Università degli Studi di Siena

Dottorato di Ricerca in Fisica Sperimentale
XVII Ciclo

Studies on the performances of the Monitored Drift Tubes of the Atlas detector

Dott. Alessandro Di Girolamo

Supervisor:
Prof. **Paolo Bagnaia**

Tutor:
Dott. **Nicola Turini**

Anno Accademico 2004

Contents

Introduction

ATLAS is one of the major experiments currently in construction at the Large Hadron Collider (*LHC*) at CERN. The experiment and the collider are scheduled to start the data taking in 2007. In these years the experimenters are designing and building the detectors, together with the related software and data handling programs.

This Thesis has been realized in collaboration with the group of the INFN of Roma *La Sapienza*, which is involved in the production of part of the chambers of the muon spectrometer of ATLAS (the *MDT chambers*, based on the drift chamber technology). The production is well advanced (the last chamber will be assembled before the end of 2004) and the focus is shifting toward the detector assembly and commissioning.

In the same time, a huge effort has been dedicated to the study on the detector performances and reliability. Due to the prohibitive environmental conditions and the close geometry of the detectors, any maintenance operation will be extremely difficult during the data taking operations, such as any replacement during the shutdown periods. It is therefore essential that those characteristics which are necessary for the physics capabilities of the detector be maintained under control.

Recently, some preliminary studies have shown that two such items are a major source of concerns and needed further analysis: the systematic error generated by the relative position of the tubes in the chamber and the possibility of a premature ageing, due to presence of pollutants in the gas mixture.

With respect to the first item, it is observed that, in the ATLAS muon spectrometer design, the relative and absolute position of the chambers is accurately measured with the help of optical devices. However, the method requires that the position of the wires inside the chamber be known, since only its variation can be calculated, by measuring e.g. the values of the temperature. Since only a small fraction of the chambers is measured at construction time, the accuracy of the detector would rely on the reproducibility of the assembly, without further checks. This Thesis presents an alternative method, developed in Roma, which is capable of measuring all the chambers, with the help of the cosmic rays data, collected just after the chamber assembly. The validation of the method relies on a simulation of the cosmic tracks, compared with the data taken in a test beam setup.

For the second item, a test had shown a deterioration of the performance of a chamber, operated under high radiation conditions with a prototype of the ATLAS gas system. In this Thesis the results of a second more systematic test are discussed. The objective of the test was to define the requirements for the components of the gas system of ATLAS and to check the behavior of the chambers after an irradiation similar to a few years of operation at LHC. For this purpose, a MDT chamber has been equipped with a dedicated electronics setup and exposed to the *GIF* facility at CERN. Both a new data taking program and analysis chain have been realized, in an effort which is comparable to a small *ad hoc* experiment.

The Thesis reports on all these subjects. Chapter 1 is dedicated to a short review of the theory of the ”Standard Model” of the elementary particles and to the ATLAS detector. Chapter 2 contains a description of the operating principles of the MDT drift tubes. The work performed by the Candidate is shown in the following chapters. In chapter 3 the measurement method of the chamber geometry parameters is described and evaluated. Chapter 4 is a description of the ageing tests, while chapter 5 contains the analysis of the tests and the results. Finally, the conclusions are summarized.

The work of this Thesis has been already partially summarized in a number of reports. We mention 4 notes [5, 1, 3, 9](all signed by the Candidate) and 4 Conference talks [1, 3, 4, 2](3 of which given by the Candidate).

Chapter 1

The Standard Model, The Large Hadron Collider and The Atlas detector

1.1 The Standard Model

The Standard Model is the current theory of fundamental particles and how they interact. It is the quantum theory that includes the theory of strong interactions, the quantum cromodynamics QCD, and the unified theory of weak and electromagnetic interactions, the electroweak theory. At present, the Standard Model does not include the effects of gravitational interactions.

According to the present knowledge all matter is made of two kinds of elementary particles: leptons and quarks. They have half-integer spin and they are called fermions; they are listed in table 1.1. The particles mediating forces are called bosons and have integer spin (table 1.2).

The fundamental fermions can be grouped into three generations of two quarks and two leptons each. Each fermion has a corresponding anti-particle with opposite electric charge and opposite charge of the strong interactions, called color charge.

There are four different types of interactions between quarks and leptons:

• the **gravitational interaction** couples to the mass of all particles and is always attractive. For high energy physics, the gravitational force is of minor importance since the masses of currently known elementary particles are very far below the scale where gravity would became appreciable;

• the **electromagnetic interaction** between electrically charged particles, de-

Leptons	mass	Quarks	mass
$\begin{pmatrix}\nu_e \\ e\end{pmatrix}$	< 3 eV/c^2 0.511 MeV/c^2	$\begin{pmatrix}u \\ d\end{pmatrix}$	1.5 – 4.5 MeV/c^2 5 – 8.5 MeV/c^2
$\begin{pmatrix}\nu_\mu \\ \mu\end{pmatrix}$	< 0.19 MeV/c^2 105.66 GeV/c^2	$\begin{pmatrix}c \\ s\end{pmatrix}$	1 – 1.4 GeV/c^2 80 – 155 MeV/c^2
$\begin{pmatrix}\nu_\tau \\ \tau\end{pmatrix}$	< 18.2 MeV/c^2 1.777 GeV/c^2	$\begin{pmatrix}t \\ b\end{pmatrix}$	174.3 GeV/c^2 4.0 – 4.5 GeV/c^2

Table 1.1: Experimentally measured masses of fermions, as reported in the Review of Particle Physics (2002) [28].

scribed by quantum electrodynamics QED in very good agreement with experiments. The mediator of this interaction is a massless spin 1 gauge boson, the photon;

- the **weak interaction**, mediated by the three massive boson W^+, W^- and Z^0, acts on all the constituents of matter. The $W^\pm$ exchange results in a change of charge of the particles taking part in the interaction and is called charged-current reaction, while the Z^0 exchange does not and is called neutral-current reaction. At low energy this interaction is very weak compared to the electromagnetic and strong interactions. It is relevant only for precesses which are forbidden by the conservation rules of the other interactions;

- the **strong interaction** takes place between quarks which make up hadrons. The mediators are 8 massless gluons. In the theory of the strong force, the QCD, there are six different types of strong charge, called color, three associated to quarks and the other three to the anti-quarks.

The electromagnetic and weak force are described in the framework of the electroweak model, or GSW model from its founders Glashow, Salam and Weinberg. It is a gauge field theory with the symmetry group $SU(2)$ x $U(1)$. To reproduce experimental results on weak decays and to allow CP violation within Standard Model, the quarks which participate in weak interactions have to be mixed by a mixing matrix (Cabibbo, Kobayashi, Maskawa CKM) defined by:

$$\begin{pmatrix} d' \\ s' \\ b' \end{pmatrix} = V_{CKM} \begin{pmatrix} d \\ s \\ b \end{pmatrix} = \begin{pmatrix} V_{ud}\, V_{us}\, V_{ub} \\ V_{cd}\, V_{cs}\, V_{cb} \\ V_{td}\, V_{ts}\, V_{tb} \end{pmatrix} \begin{pmatrix} d \\ s \\ b \end{pmatrix} \tag{1.1}$$

In general a $n \times n$ matrix is defined by n^2 complex numbers, but imposing the

boson	interaction	mass	q
Vector Boson			
W^+	Weak	80.423 ± 0.039 GeV/c^2	+1
W^-	Weak	80.423 ± 0.039 GeV/c^2	-1
Z^0	Weak	91.1876 ± 0.0021 GeV/c^2	0
γ	QED	0	0
g	QCD	0	0
Scalar Boson			
H	Yukawa	> 114.4 GeV/c^2 95% CL	0

Table 1.2: Experimentally measured masses of SM bosons, as reported in the Review of Particle Physics (2002) [28]. The last columns report the quantum numbers of these particles.

unitarity and eliminating trivial phases, the V_{CKM} is described in terms of 3 angles and 1 imaginary phase for a total of four free parameters.

In the Standard Model Lagrangian, particles are massless since mass terms are not invariant. Thus, to preserve the gauge-invariance of the Standard Model Lagrangian, is essential to introduce the particle mass through a mechanism called Spontaneous Symmetry Breaking. This mechanism is based on the existence of the Higgs boson and makes use of one isodoublet field: three Goldstone bosons among the four degrees of freedom are absorbed to build up the longitudinal components of the massive $W^\pm$ and Z bosons; the last degree of freedom corresponds to a physical scalar particle, the Higgs boson.

The search for the Higgs boson mass is shown in figure 1.1. Till the Higgs boson would be experimentally observed, the Standard Model will not be completely verified. This particle has to be searched in a mass range from 114 GeV/c^2, the limit of the direct searches at LEP2 [6], to 1 TeV/c^2, the theoretical limit imposed by the stability of the theory.

Different theories have been proposed as an extension of the Standard Model. One of the most promising is the Minimal Supersymmetric extension of the Standard Model (MSSM): it contains the minimum number of particles and it is based on the assumption that a particle, boson or fermion, has a “superpartner” with opposite statistics. The MSSM requires two isodoublets of Higgs fields to cancel anomalies and to associate the mass to the fermions.

1.2 LHC The Large Hadron Collider

The Large Hadron Collider is currently under construction at CERN in Geneva. It is a proton proton collider with a center of mass energy of 14 TeV and a luminosity of $10^{34}\mathrm{cm}^{-2}\mathrm{s}^{-2}$.

Figure 1.2 shows a schematic view of the accelerator complex. The LEPaccelerator has been removed from its 27 km circumference tunnel to allow the installation of the new LHC. The Proton Synchrotron (PS) and the Super Proton Synchrotron (SPS) will be used to (pre)accelerate the protons before injecting them into the LHC: for the forthcoming LHC operation they will accelerate the protons up to an energy of 450 GeV. Once in LHC, the protons are accelerated up to the full LHC beam energy of 7 TeV.

The LHC opted for a scheme with proton proton collision because high intensity proton beams are easier to realize than high intensity anti-proton beams. As a consequence, the LHC requires separate vacuum pipes for each proton beam, both contained in the same cryogenic and mechanical structure, and demands a novel design of the superconducting bending magnets, the “twin” aperture dipoles, to keep the two proton beams rotating on orbit in opposite directions (figure 1.3). The 1232 magnets needed along the beam line are 14.6 m long and will have a magnetic field of 8.33 T.

The LHC proton beams will have 2808 bunches of approximately 10^{11} particles each, resulting in a beam current of typically 0.56 A and a collision frequency of 40 MHz. The beams will collide with an angle of 300 μrad to avoid multiple collisions between the bunches near the interaction vertex. The bunches will be 7.7 cm long and will have a radius of 16 μm at the crossing point, so the spread of the position of the interaction vertex is expected to be 5.6 cm of r.m.s. along the beam line. The luminosity can be expressed in terms of these beam parameters

$$L = \frac{N_1 N_2 f k}{4\pi\sigma^2} \tag{1.2}$$

where N_i are the number of protons in each colliding bunch, k is the number of bunches, f is the beam revolution frequency of $1.1 \cdot 10^4$ Hz and σ is the transverse bunch width in the interaction point. Thus the Large Hadron Collider is expected to achieve the luminosity of $L = 10^{34}\mathrm{cm}^{-2}\mathrm{s}^{-2}$. This surpasses the highest luminosity reached ever before in a hadron collider by almost two orders of magnitude. The corresponding yearly integrated luminosity for the LHC is expected to reach 100 fb^{-1}.

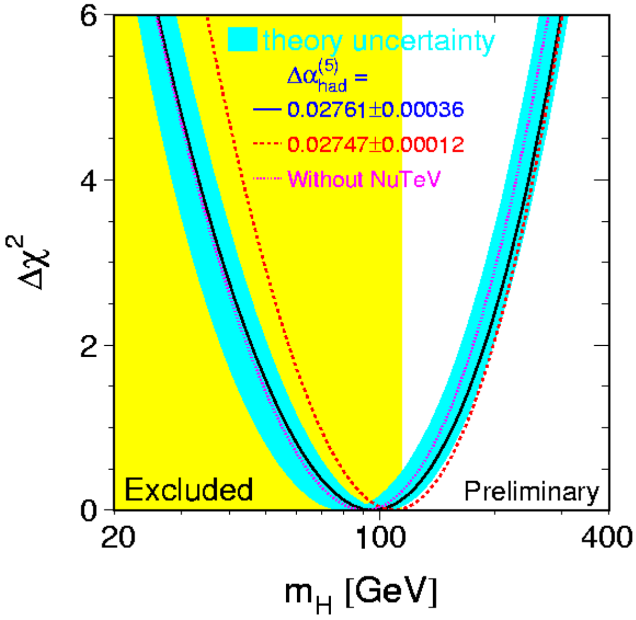

Figure 1.1: The χ^2 of the fit to electroweak data as a function of the Higgs mass [12].

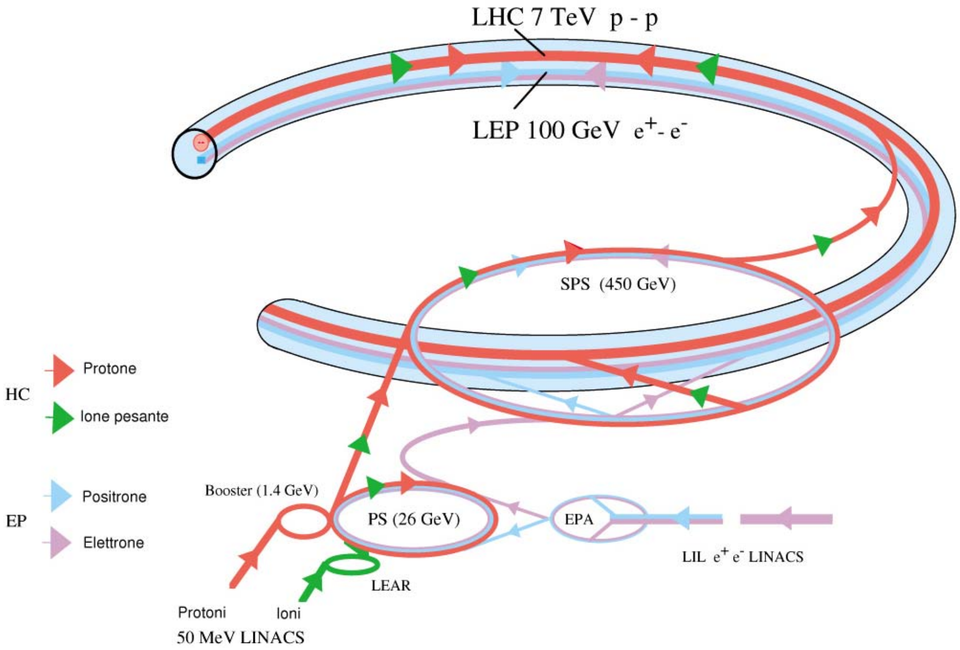

Figure 1.2: Illustration of the LHC accelerator complex.

1.2.1 Experiment at the LHC

Few experiments will be installed in the four interaction points of the LHC. We consider:

- ALICE (**A** **L**arge **I**on **C**ollider **E**xperiment) is an experiment specialized to heavy ion physics in Pb-Pb collisions with center of mass energy at the PeV scale in particular dedicated to the search for a new phase of matter, the quark-gluon plasma[10].
- ATLAS (**A** **T**oroidal **L**HC **A**pparatu**S**) is a general purpose experiment for the physics of proton-proton collisions. The ATLAS detector will be described in the next sections.
- CMS (**C**ompact **M**uon **S**olenoid) is the second general purpose experiment at the LHC. Its basic design differs from ATLAS mainly in the uniform solenoidal magnetic field which covers the whole detector including the muon chambers[11].
- LHCb is an experiment specialized in the B-physics. Since B mesons are most likely to emerge from collisions close to the beam line, LHCb is designed as an open-geometry forward detector in order to catch low angle particles [33].

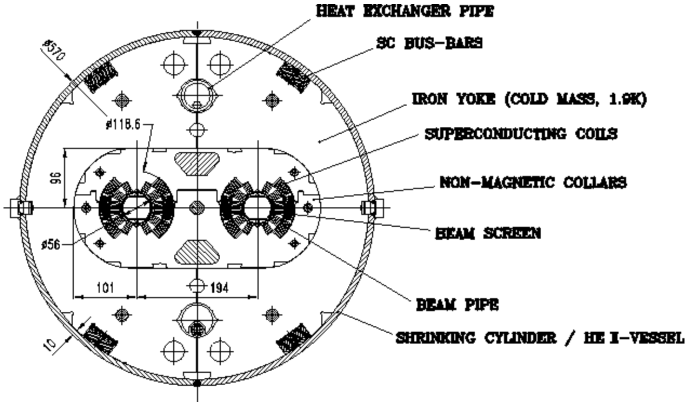

Figure 1.3: Cross section of the LHC “twin” dipoles

1.3 Physics program at the LHC

As discussed above, the search for the Higgs particle is the key element of the LHC physics program, since its discovery would validate one of the corner stones of the Standard Model: the mechanism of the electro-weak symmetry breaking.

In addition, other theories offer predictions of the phenomena well within the range of LHC. In the minimal supersymmetric extension of the SM, MSSM, the super-partners of the known particles are expected to have masses at the TeV scale and thus to be observable at the LHC.

Several extensions of the SM postulate the existence of additional heavy gauge bosons Z' and W'. They would be accessible to the LHC for masses up to 5 or 6 TeV. The hunt for any signal of new physics is another relevant part of the physics program.

As visible in figure 1.4, the production cross-section for b and t quarks will be very high. Already at the initial lower luminosity of 10^{33}cm^{-2}s^{-2}, about 5*10^{12} $b\bar{b}$ and 10^{7} $t\bar{t}$ will be produced every year: precise measurements of the b-quark related elements of the CKM matrix and the verification of the predicted CP violation in the decays of B^0_d and B^0_s will be possible, together with precise measurements of the top quark mass and detailed studies of its decay channels.

1.3.1 The search for the Higgs boson

The total Higgs production cross section at LHC is predicted to range between 0.1 pb and 100 pb depending on the Higgs mass, as shown in figure 1.5. The dominant production mechanisms are via gluon-gluon fusion, WW fusion and ZZ fusion. Other less important processes are $t\bar{t}$ fusion and Higgs bremsstrahlung from W or Z (figure 1.6). Figure 1.7 shows the Higgs branching ratios as a function of the Higgs mass:

- 80 GeV $< m_H <$ 130 GeV:

  Since in this low mass range the b-quark is the heaviest accessible particle for pair production, the channel $H \rightarrow b\bar{b}$ is dominant but the signal to background ratio is smaller than 10^{-5} because direct $b\bar{b}$ production has a big cross section, as shown in figure 1.4. However this decay mode can be used in the associated production of the Higgs with a W, a Z or a $t\bar{t}$ pair, so the background can be reduced by lepton tagging and the $b\bar{b}$ pair can be detected by looking for the secondary vertices.

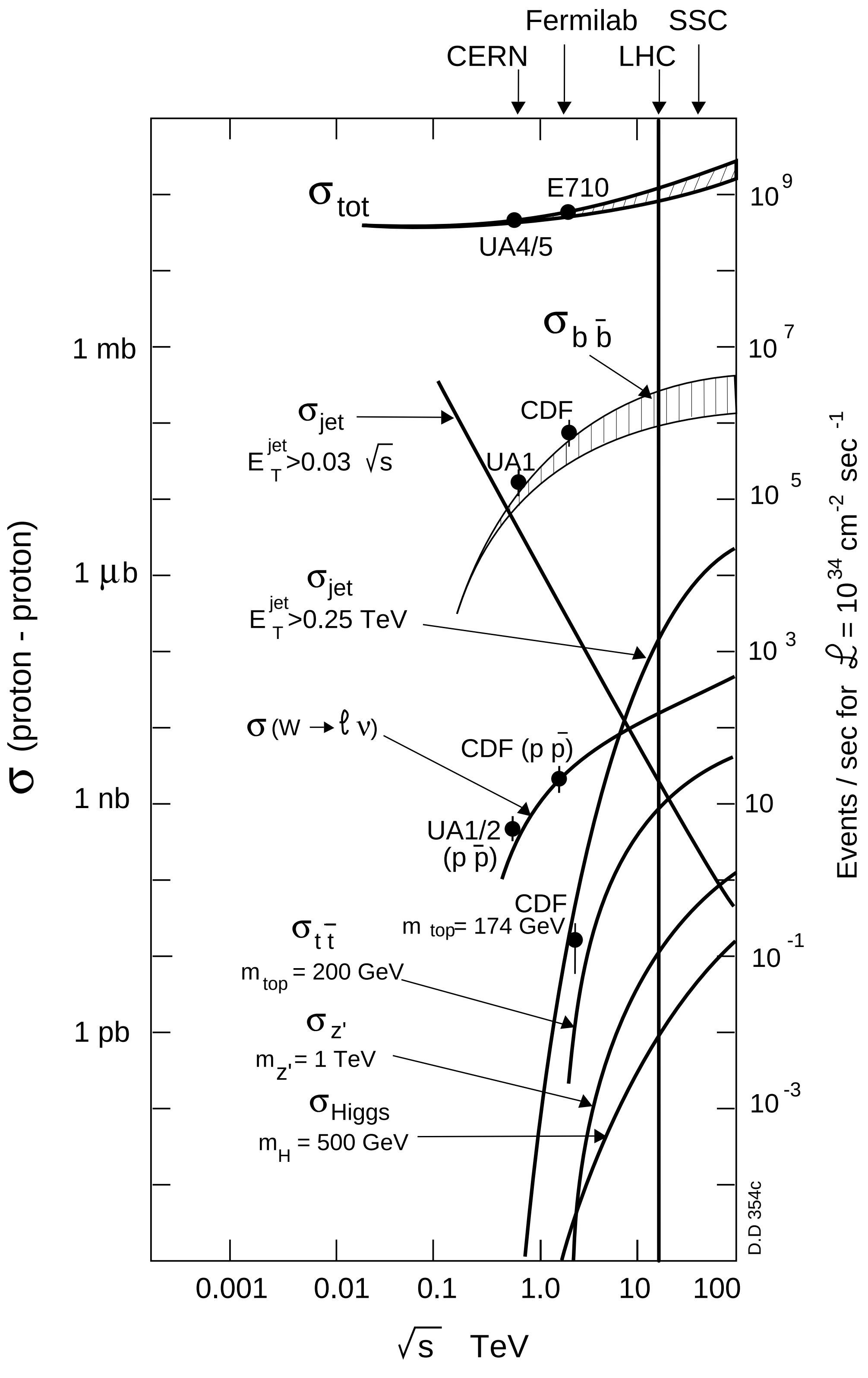

Figure 1.4: Cross section for the Higgs boson production compared with concurrent processes cross sections for a luminosity L=10^{34}cm^{-2}s^{-2}.

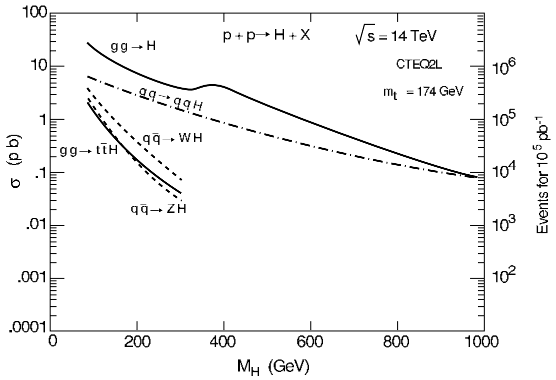

Figure 1.5: Higgs boson production cross section at the LHC for various processes as a function of the Higgs mass

Another interesting channel in this mass range is $H \to \gamma\gamma$. Even if it suffers from its low branching ratio, the signal to background ratio is expected about 10^{-2}. As in the previously discussed channel, the associated production of a W can help reducing the background.

- 130 GeV $< m_H < 2m_Z \sim 180$ GeV:

  The decay $H \to ZZ^* \to 4l$ offers a clean signature due to the high transverse momenta of the four leptons. Due to the small width of the Higgs in this mass domain (figure 1.8), at least 1% of mass resolution is required.

  For Higgs masses near 2 $m_W \sim 160$ GeV the branching ratio of the previously described channel is strongly reduced because the decay mode $H \to WW^{(*)} \to l\nu l\nu$ opens up. This channel has the disadvantage that the Higgs peak cannot be reconstructed due to the escaping neutrinos. Thus a precise measurement of the missing energy is required.

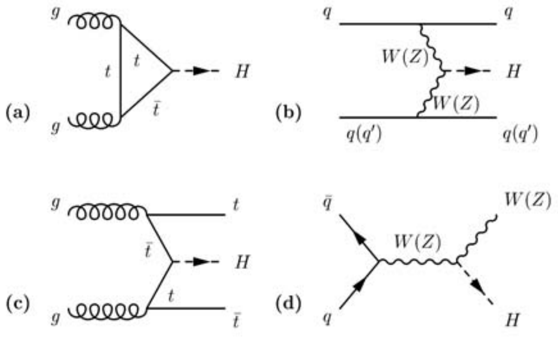

Figure 1.6: Feynman diagrams of the dominant Higgs production mechanism at the LHC

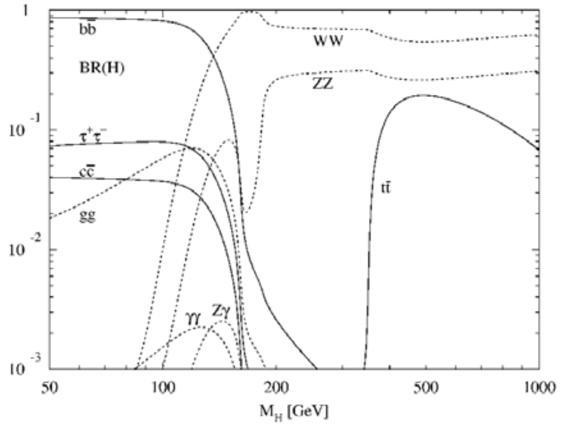

Figure 1.7: Branching ratio of all the possible Higgs boson decays vs the Higgs boson mass

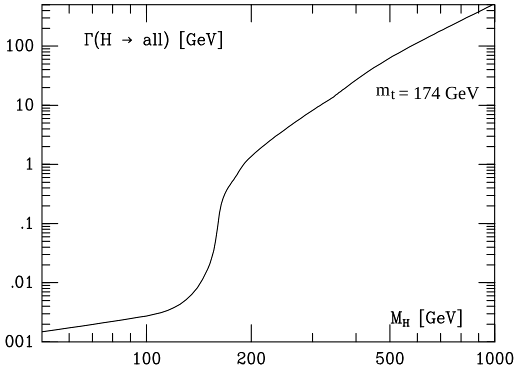

Figure 1.8: Total Higgs width Γ_H as a function of M_H

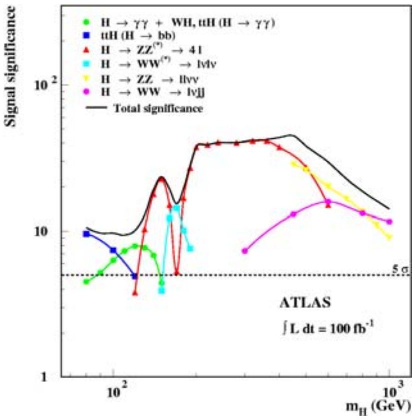

Figure 1.9: Statistical significance for the discovery of the Higgs boson in different channels

- $2m_Z < m_H <$ 800 GeV:

  Above the threshold for two real Z the discovery should be easy in the channel $H{\rightarrow}ZZ{\rightarrow}4l$ that offers a large branching ratio and low background. The sources of background for this process are mainly two, $t\bar{t}{\rightarrow}Wb{+}W\bar{b}{\rightarrow}l\nu{+}l\nu\bar{c}{+}l\nu{+}l\nu c$ and $Zb\bar{b}{\rightarrow}lll\nu cl\nu\bar{c}$, but the signal can be detected requiring an high invariant mass for the two lepton pairs.

- $m_H >$ 800 GeV:

  For very large masses the principal decay channels are: $H{\rightarrow}ZZ{\rightarrow}ll\nu\nu$, characterized by the missing transverse energy due to neutrinos and by two leptons with high transverse momenta, $H{\rightarrow}ZZ{\rightarrow}ll + 2jets$ and $H{\rightarrow}WW{\rightarrow}l\nu + 2jets$

> where the energy and angular distribution of the jets have to be measured with a hadronic calorimeter.

In figure 1.9 we plot the statistical significance, $N_{Sgnl}/\sqrt{N_{Bckgrnd}}$, as a function of the Higgs mass for the different decay modes previously described. The Atlas detector efficiency and resolution are included in the computation.

1.4 The Atlas detector

The Atlas detector has been designed in order to exploit the full discovery potential of the LHC outlined in the previous sections. Figure 1.10 shows a three dimensional cut-away view of the entire Atlas detector. This description is based on the published design of the experiment, the so-called "TDR"[13].

The inner detector surrounds the beam line and measures the trajectories, and thereby the momenta, of charged particles. A super-conducting solenoid, which generates an homogeneous 2 T magnetic field in the inner detector volume, surrounds the inner detector. Directly outside this solenoid the electromagnetic and hadronic calorimeters are located. The outermost shell of Atlas is formed by the muon spectrometer. The magnetic field in this last region is realized by three huge super-conducting toroids, that generate an average magnetic field of about 0.5 T. The Atlas detector has a coverage of $0 < \phi < 2\pi$ in azimuth and of $|\eta|<5$ in pseudo-rapidity[1].

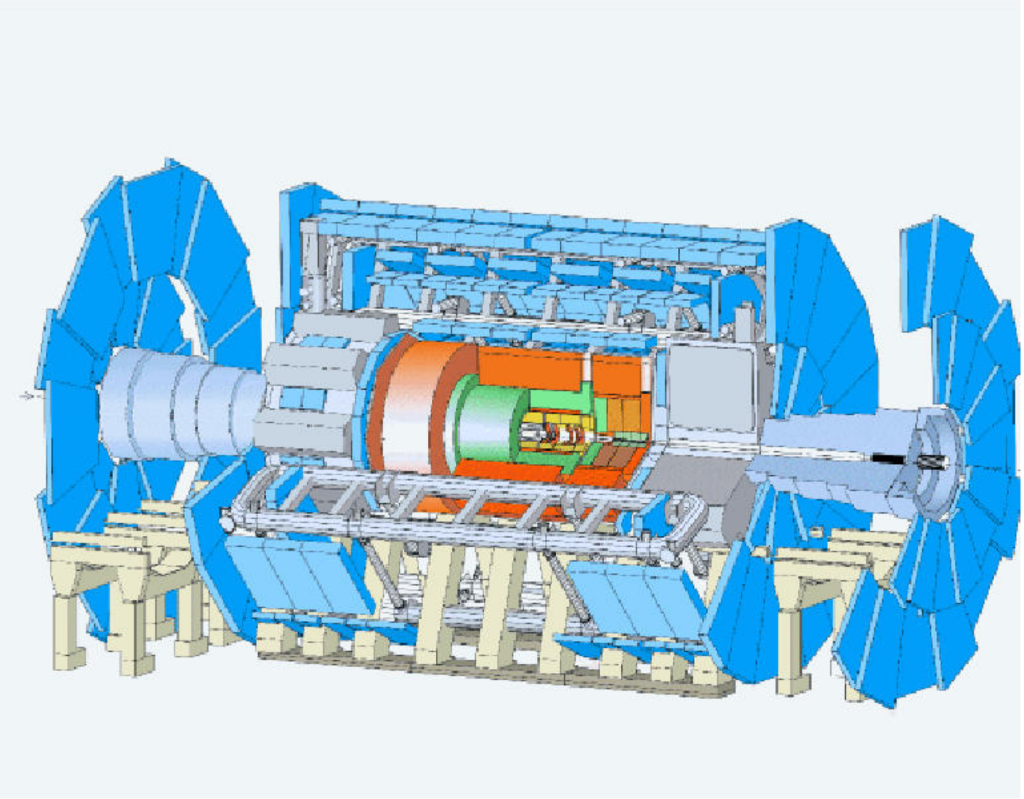

Figure 1.10: Three dimensional cut-away view of the entire Atlas detector

---

[1] the pseudo-rapidity is defined as $\eta = -ln\theta/2$

1.4.1 The Magnet system

One of the characteristics of the Atlas detector is its magnetic system: it is composed of a Central Solenoid (CS) surrounding the Inner detector, one Barrel toroid (BT) and two End Cap toroids (ECT) surrounding the muon spectrometer. The three toroids are constituted by eight coils, as shown in figure 1.11 and their bending power is reported in figure 1.12.

The central solenoid has been optimized to minimize the amount of material in front of the electromagnetic calorimeter. For this reason they share the same vacuum vessel.

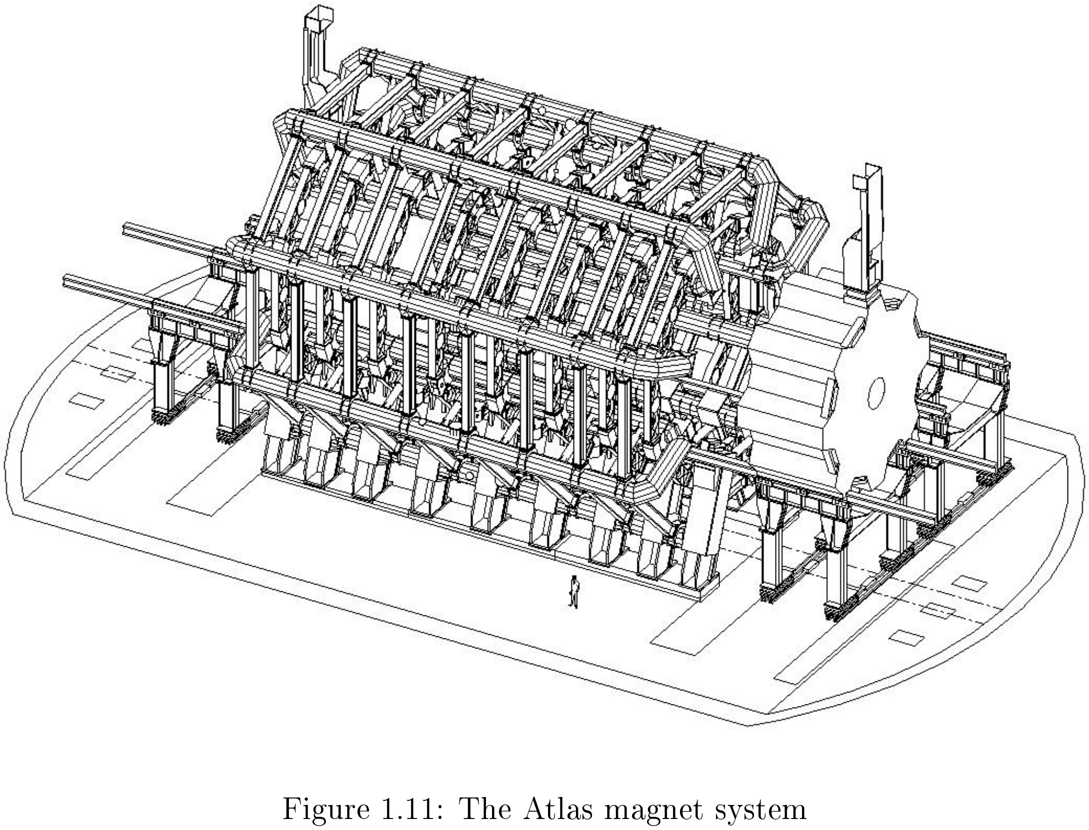

Figure 1.11: The Atlas magnet system

The barrel toroids coils are housed in eight independent cryostats, while each of the ECT is housed in a single cryostat.

1.4.2 The Inner Detector

The Inner detector (figure 1.13) covers the radial range from 4 cm to 1 m around the beam. Its task is a high precision tracking as close as possible to the primary vertex of the p-p interaction, with the aim of finding secondary vertices and identifying particles. The Central solenoid allows charge identification and momentum measurement.

Due to the enormous events rate, to keep the single channel occupancy at a modest level a very high granularity is required.

The **Pixel Vertex Detector** is the nearest to the beam line. It consists of three barrel layers and four forward disks of silicon detectors segmented in pixels of 50 μm$\times$300μm, for a total of about 140 million of silicon pixels. The finer segmentation is oriented along the bending direction of the solenoid, along ϕ: on this coordinate a resolution of 12 μm will be achieved, while on the second coordinate, along the beam line, a resolution of about 70 μm is expected.

The **Semi Conductor Tracker** covers the radial range between 30 and 55 cm. It will consist of layers of silicon microstrip detectors, 4 layers in the barrel region and 9 in each of the two endcap. The total number of readout channel will be 6.2 million, the spatial resolution will be 16 μm in the azimuthal direction and 580 μm in z .

The third and outer part of the Inner detector is the **Transition Radiation Tracker**. Its components will be gas-filled straw tubes arranged in layers separated by polypropylene/polyethylene radiators: when particles cross these radiators, transition radiation photons are created and then converted in electrons in the Xenon based operating gas of the straw tubes. Each track will be measured with a precision of 170 μm by each tube it will cross.

The combination of these three detectors guarantees for any track more than 40 points. The Inner detector typically achieves a momentum resolution of $\frac{\Delta p_T}{p_T}$<30% at p_T=500 GeV and $|\eta|$<2, and an impact parameter resolution of about 15 μm.

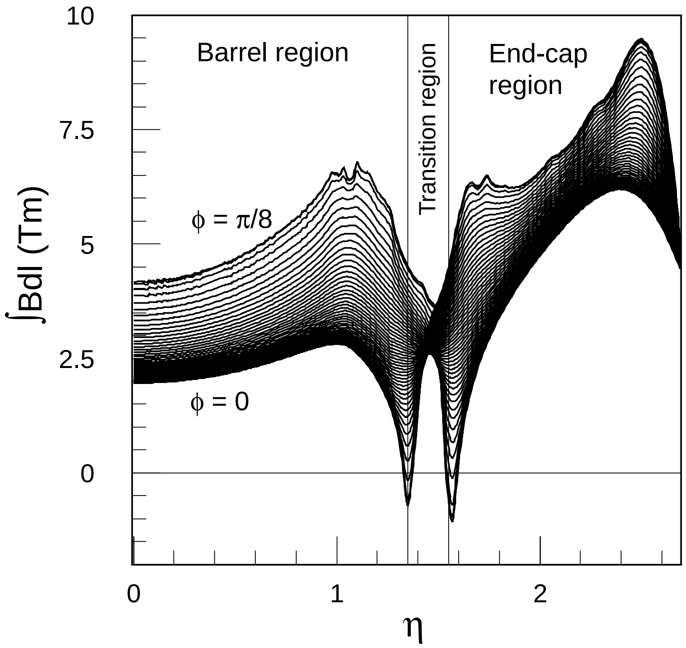

Figure 1.12: Bending power of the barrel and endcap toroids as a function of η. The different lines corresponds to different azimuthal angles

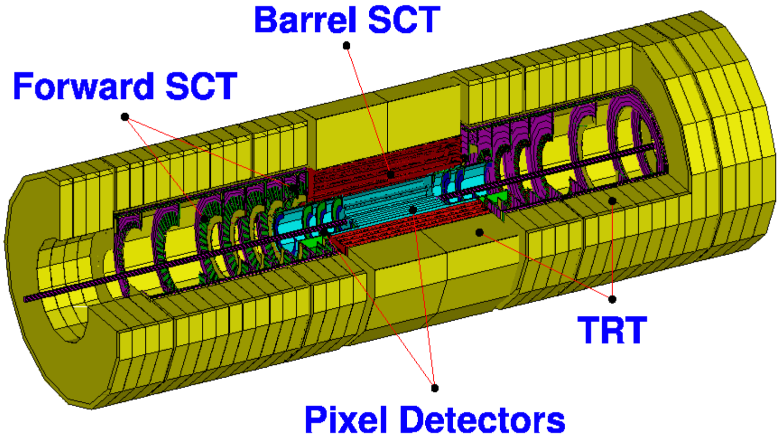

Figure 1.13: Vertical cut of through one quarter of the inner detector

1.4.3 The Calorimeters

The Atlas calorimetric system has been designed to meet the different demands of the LHC physics program. This system, shown in figure 1.14, is composed by an electromagnetic liquid argon calorimeter covering the pseudorapidity region $|\eta|<3.2$, an iron scintillating tiles hadronic calorimeter covering the pseudorapidity region $|\eta|<1.7$, an end-cap liquid argon hadronic calorimeter covering the region $1.5<|\eta|<3.2$ and a forward liquid argon calorimeter covering the region $3.2<|\eta|<4.9$,

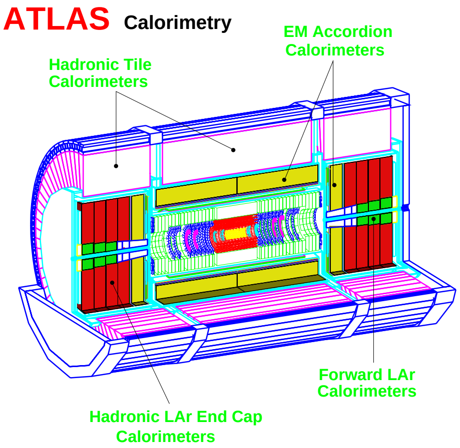

Figure 1.14: The Atlas calorimetric system.

The **Electromagnetic calorimeter** can be divided in a barrel region, up to $|\eta|<1.475$, and an end-cap region, composed by two concentric wheels. The EM calorimeter is a detector made of accordion-shaped lead absorber plates alternating with copper readout electrodes on kapton carriers. Its total thickness corresponds to more than 24 radiation lengths X_0. The gaps between absorbers and electrodes are filled with liquid argon. With a granularity of $\Delta\eta$ x $\Delta\phi \sim 0.025$ x 0.025 an angular resolution of 40 μrad/$\sqrt{E(GeV)}$ will be obtained. The expected energy resolution is $\frac{\sigma_E}{E}$=10%/$\sqrt{E(GeV)}\oplus$1%.

The **Hadronic calorimeter** has been designed with a thickness of about 10 interaction lengths. This thickness is adequate to obtain a good containment of hadronic showers and to reduce punch-through in the muon spectrometer. The large η coverage will permit good E_T^{miss} measurements. The hadronic tile calorimeter is a sampling calorimeter using iron and scintillating tiles with a readout granularity $\Delta\eta \times \Delta\phi$ between 0.1 x 0.1 and 0.1 x 0.2. At larger pseudorapidity the hadronic calorimeter is based on the use of liquid argon. The expected combined energy resolution is $\frac{\sigma_E}{E}$=50%/$\sqrt{E(GeV)}\oplus$3% in the barrel and $\frac{\sigma_E}{E}$=100%/$\sqrt{E(GeV)}\oplus$10% in the end caps.

1.4.4 The Muon Spectrometer

The Muon Spectrometer dominates Atlas by its impressive dimensions of 22 m in diameter and 44 m in length. The overall layout is shown in figure 1.15 and 1.16.

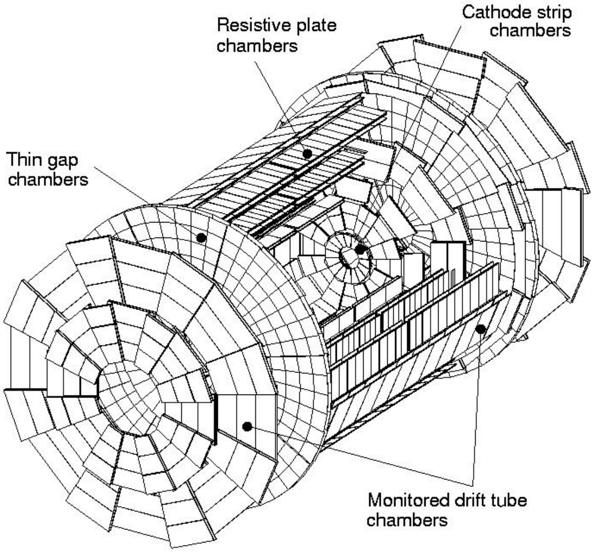

Figure 1.15: 3-dimensional view of the Atlas Muon Spectrometer

The idea underlying the design is to measure the transverse momentum of muons by deflecting them in the magnetic field previously described and to measure each muon tracks in at least three chambers: the detectors are positioned at three locations along a muon track. In the barrel the three stations (see figure 1.16) are mounted concentrically around the beam line at 5 m (*inner*), 7 m (*middle*) and 10 m (*outer*) radial distance. In the end-cap the disks are mounted perpendicular to the beam line at 9 m (*inner*), 14 m (*middle*) and 20 m (*outer*) from the interaction point. The design performances of the muon spectrometer are:

- Momentum resolution at the level of 1% up to 1 TeV operating indipendently from other subdetectors.
- Second coordinate (non bending view) measurement with a spatial resolution of 5-10 mm.
- Pseudorapidity coverage up to $|\eta|<2.4$ for trigger and up to $|\eta|<3.0$ for precision measurements

- High trigger selectivity with transverse momentum programmable thresholds.
- Bunch Crossing identification with a time resolution much better than the 25 ns LHC bunch crossing period.
- Capability to operate for many years in a high radiation background and high flux environment.

Four different technologies have been chosen for trigger and precision chambers in different regions of the spectrometer. As trigger chambers Resistive Plate Chambers (RPC) and Thin Gap Chambers (TGC) are used. The RPC are a gaseous detector constituted by two bakelite plates separated by insulating spacers. The 2 mm gap between the bakelite plates is filled with $C_2H_2F_4$. The avalanche charge produced by the particles is readout via capacitive coupling: the spatial resolution is about 3 cm while the time resolution is of $\sim$2 ns. They are used in the region $|\eta|<1.1$. The TGC are multiwire proportional chambers with a distance between anode wires of 1.8 mm and a distance between anode and cathode planes of 1.4 mm. They are operated with CO_2 / n-C_5H_{12} gas mixture at a voltage of 3.1 kV. The short anode wires distance gives a short drift time and thus a good time resolution of about 5 ns, sufficient to make bunch crossing identification. The TGC are used in the end-cap region.

As precision chambers, Monitored Drift Tubes (MDT) and Cathode Strip Chambers (CSC) are used.

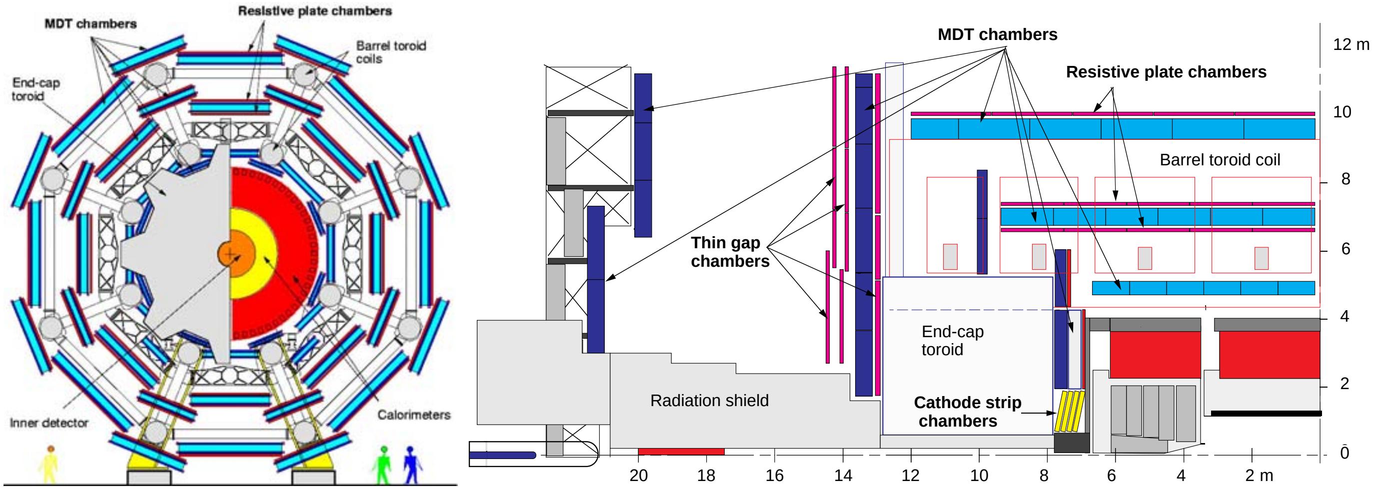

Figure 1.16: Transverse and longitudinal view of the Atlas Muon Spectrometer

The MDT, ionization detectors operated in proportional mode, will be described in detail in the next chapters. The CSC are multiwire proportional chambers with an anode wire spacing of ∼2.5 mm. The precision coordinate is obtained measuring the charge collected on the cathode strips and the expected resolution is ∼60 μm. As CSC have better performances than MDT when exposed to a high flux of particles, they are used in the forward region ($|\eta|>2$).

In figure 1.17 the expected Atlas transverse momentum resolution for the inner tracker, the muon spectrometer, and the combined system is plotted. No systematic errors, like the chamber alignment and calibration, are considered.

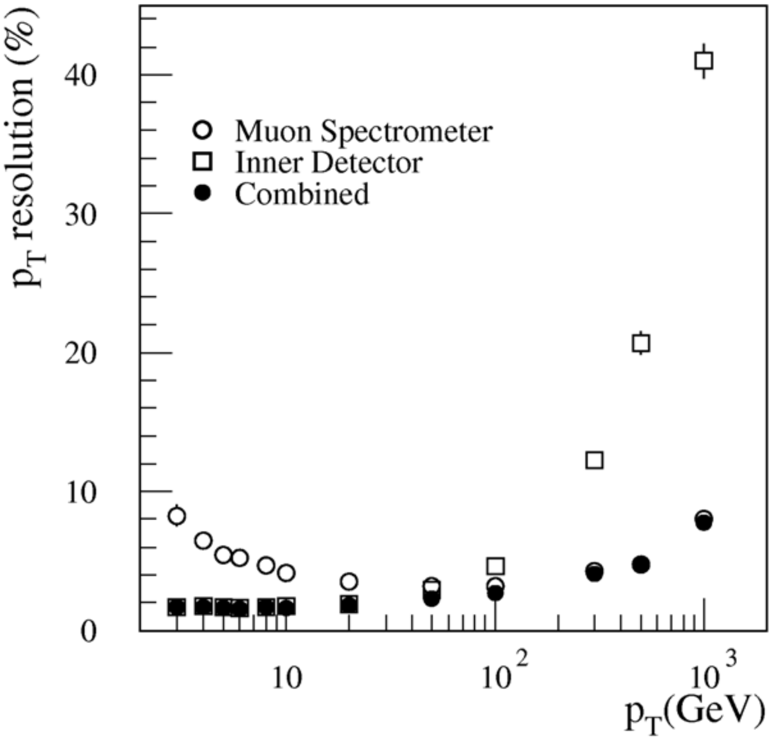

Figure 1.17: p_T resolution of track reconstruction in the Muon system, in the Inner and of combined tracks. [13]

1.4.5 Particle flux and background conditions

The radiation conditions define the specifications for rate capability, granularity, ageing robustness and radiation hardness of the muon chambers. The particle flux can be distinguished in two categories:

- Primary collision products (figure 1.18): These are particles still associated in time with pp interactions, mainly muons and hadrons with momenta above 3 GeV. As we can see from figure 1.18, the primary background is dominated by muons from the decay of low-p_T pions and kaons in the inner detector and the calorimeter. The second most important contribution comes from prompt muons produced in the decay of hadrons with b and c quark: for p_T>8 GeV they even dominate the inclusive cross-section. Less important are muons from gauge bosons and t quark decay. Finally there is the contribution from "punch-through" hadrons, like hadrons which do not interact in the calorimeter and penetrate into the muon spectrometer: as the big absorptive power of the calorimeter system, this hadronic debris is suppressed down to a negligible amount.

  However the particle rate from the primary background is expected at the scale of 10 Hz/cm^2 in the innermost precision chambers: this rate is negligible compared to the uncorrelated radiation which will be discussed next.

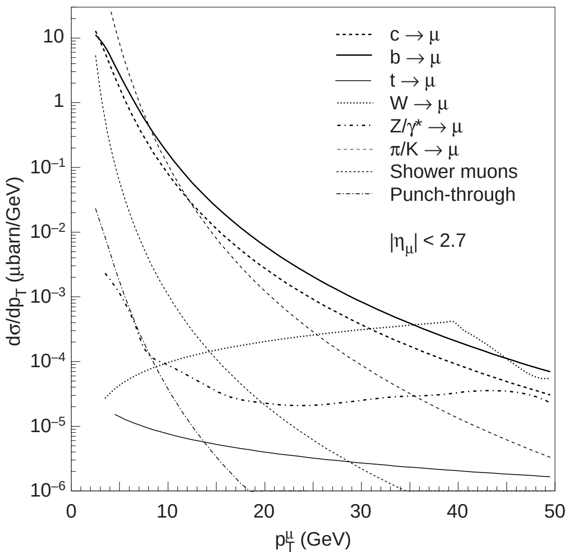

Figure 1.18: Simulated inclusive cross section for primary collision products as a function of p_T, integrated over $|\eta|$<2.7. [13]

- Radiation background (figure 1.19): In the interactions of primary collision products with various detector and machine elements huge quantities of low-energy photons and neutrons are produced. By frequent rescattering these particles lose any correlation with the initial pp collision and form a permanent background, the "cavern background", with energies mainly between few keVs and 10 MeV. On MDT counting rates up to 100 Hz/cm^2 are expected, corresponding to 300 Hz per centimeter tube length. The region $|\eta|>2$, as already mentioned, will be equipped with Cathode Strip Chambers which can operate at higher rates than MDT: they will have to cope with up 1 kHz/cm^2.

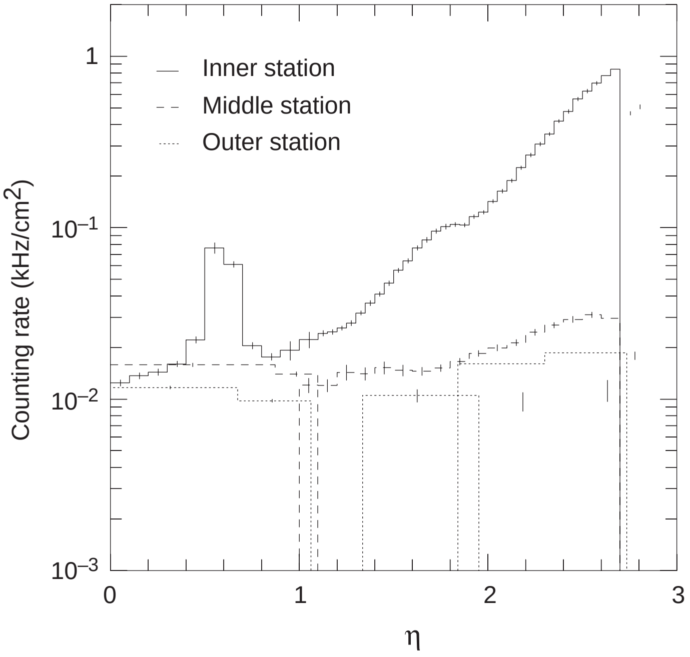

Figure 1.19: Total counting rates in the three stations of precision chambers as a function of pseudorapidity at nominal luminosity 10^{34}cm^{-2}s^{-2}.

Presently the background counting rate is still subject to uncertainties. To minimize the risk of underestimating it, the Atlas collaboration decided to design the muon system for a five times higher background than the average expectation.

To study the effects of the high rate radiation background on Monitored Drift Tubes, a dedicated experiment with a strong gamma source was carried out. It will be one of the subjects of this Thesis.

1.4.6 The Trigger System

The Atlas trigger system is organized in three levels which successively reduce the event rate from the bunch-crossing rate of 40 MHz, that corresponds to an interaction rate of 1 GHz at high luminosity, to about 100 Hz, which can be written to mass storage devices. (see figure 1.20)

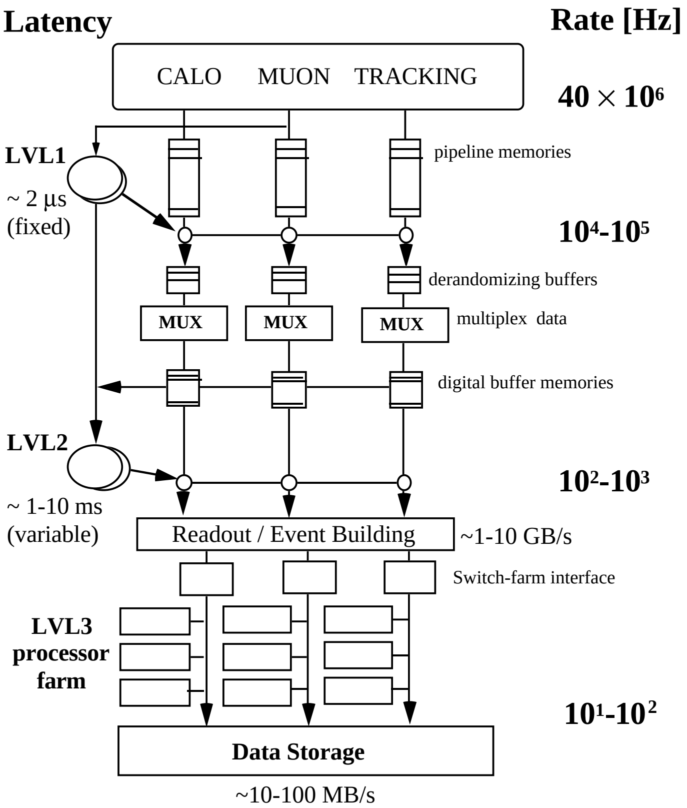

Figure 1.20: The Atlas three level trigger scheme

The first level trigger (Lvl1) uses the information with reduced granularity of the calorimeters and the muon trigger chambers. The Lvl1 has a latency of 2 μs and a maximum pass rate of 75 kHz. The calorimetric Lvl1 trigger searches for high p_T isolated electron and photons, for isolated leptons decaying in hadrons, for jets and for large missing and transverse energy, while the first level muon trigger searches for high or low p_T muons. All the selection algorithms can be combined in coincidence or in veto in a flexible way. During the Lvl1 decision time the data must be stored in pipelined memories because the Lvl1 latency extends over many of the 25 ns spaced LHC bunch crossings. The events accepted are stored in the so-called Read Out Buffers (ROBs) to be analysed by the second level trigger (Lvl2).

The Lvl2 has an event dependent latency from 1 ms to 10 ms, and reduces the data rate to a maximum of 1 kHz. In order to reduce the data transfer bandwidth from the ROBs to the second level trigger processors, the Lvl2 algorithm works on subsets of the detector data called Regions of Interest (RoIs). The muon trigger selection criteria are improved at Lvl2 by sharpening and imposing isolation to the muon tracks candidates if some particular decay channel are searched for. The sharpening is obtained using also the data from the muon spectrometer precision chambers and from the Inner detector. The track isolation is achieved using the data from the calorimeter cells close in $\eta - \phi$ to the muon candidates. Electron and photon isolation is checked using the full granularity information of the calorimeter and, only for the photons, also of the Inner detector. For the event accepted by the Lvl2, the data are sent to the Event Builder and written into the Full Event Buffers.

The third level trigger (Lvl3) is now applied to the whole event. The Lvl3 uses complex offline algorithms mixing online informations with parameters from calibrations, alignment procedures and from the magnetic field map. For the maximum trigger rate of 100 Hz, the data rate written to mass storage corresponds to 100 MByte/s. As one nominal LHC running year is $\sim 10^7$s, the recorded data amounts to 1 PByte per year.

Chapter 2

The Atlas Monitored Drift Tubes

In the major part of the Muon Spectrometer the technology of Monitored Drift Tubes (MDT) is adopted as precision chambers. A MDT chamber consist of two "multilayers" separated by a spacer structure of "cross-plates" and "longitudinal beams". Each multilayer is composed by three or four layers of 30 to 72 tubes, which are between 1.6 m and 5 m long. The number of tubes and layers depends on the location of the chamber in the muon spectrometer. To cover the whole spectrometer area of 5500 m^2, 1194 MDT chambers with 370000 tubes are needed. In figure 2.1 a MDT chamber is shown.

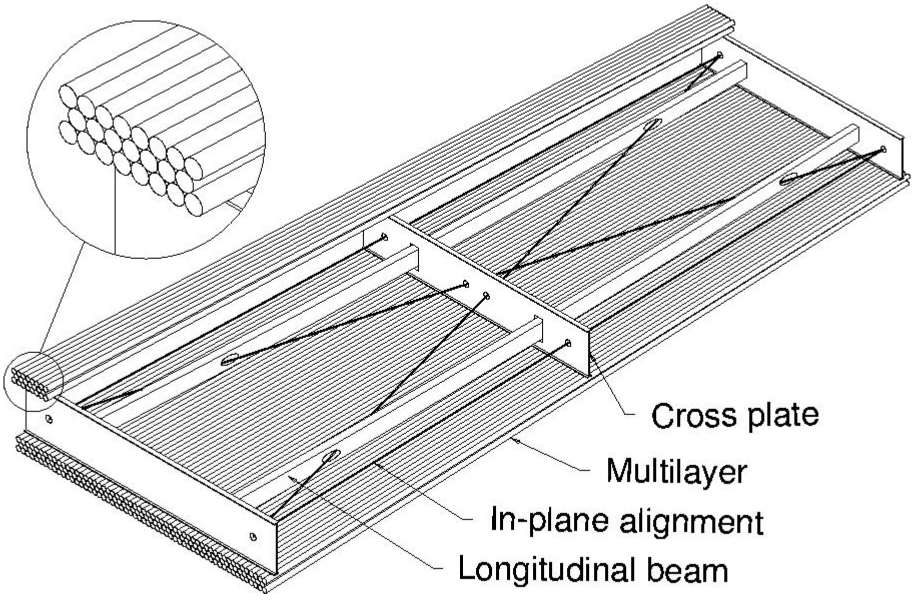

Figure 2.1: A Monitored Drift Tube chamber

2.1 The Muon Measurement principle with the MDT

The single drift tube is made out of an aluminum tube with a wire that is connected to high voltage. The tube is filled with a non-flammable gas at high pressure to reduce diffusion and ionisation position fluctuations.

When a charged particle crosses the tube, the gas is ionised along its track. The electrons drift to the wire and the ions to the wall of the tube: these movements generate a current signal on the wire. By knowing a common trigger and the space-drifttime relation, the distance of the track from the wire can be calculated. The measured distances on different tubes are combined to reconstruct a track segment in the chamber. To achieve the designed $\frac{\Delta p_T}{p_T}$ of maximum 10% at $p_T = 1$ TeV, the sagitta of muon tracks must be measured with an accuracy of ~ 50 μm, as the sagitta of a muon of 1 TeV is approximately 500 μm in the average magnetic field of 0.5 T of the muon spectrometer.

2.2 Monitored Drift Tube Specifications

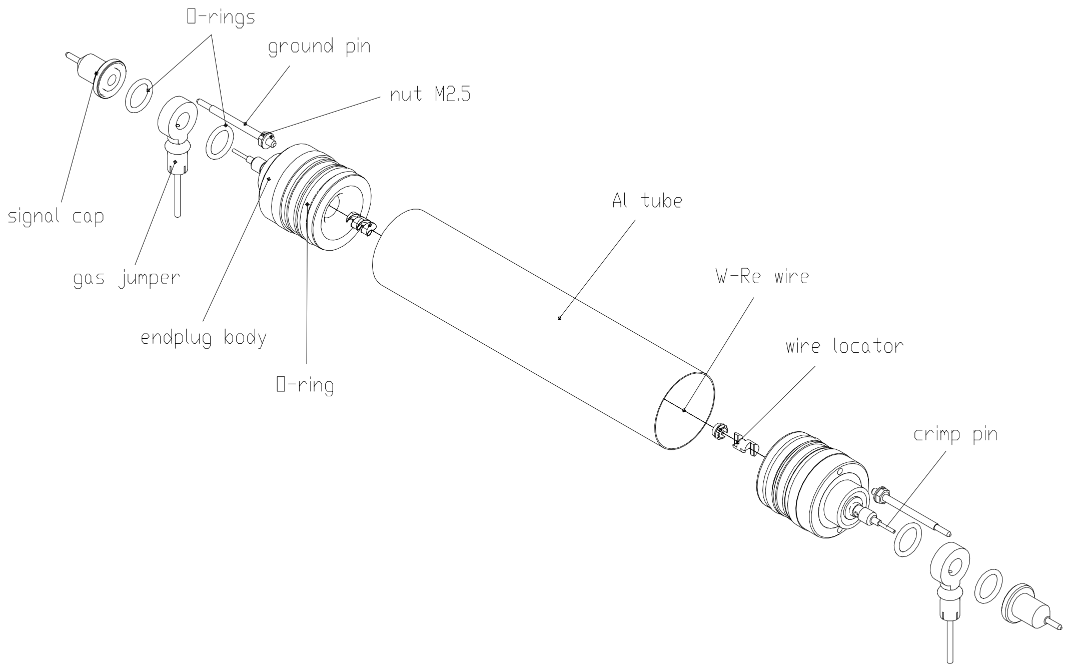

Figure 2.2: Exploded view of a Drift Tube

The exploded view of a Monitored Drift Tube is shown in figure 2.2. The tube consists of a 29.97 mm diameter aluminum tube with a 400 μm thick wall. It is filled with Ar-CO_2 (93:7) at 3 bar absolute and holds at its center a 50 μm gold plated tungsten-rhenium wire at 3080 V. The tube is closed at both ends with two endplugs, made of Noryl reinforced with glass fiber. These endplugs, shown in figure 2.3, serve several purposes at the same time: they hold the wire in the center of the tube with a precision of 10 μm by using a twister wire locator inserted in the central hole of the endplug; they provide electrical insulation between the anode wire and the cathode tube wall; finally they hold the gas connectors("jumpers") to allow the inlet and the outlet of the gas.

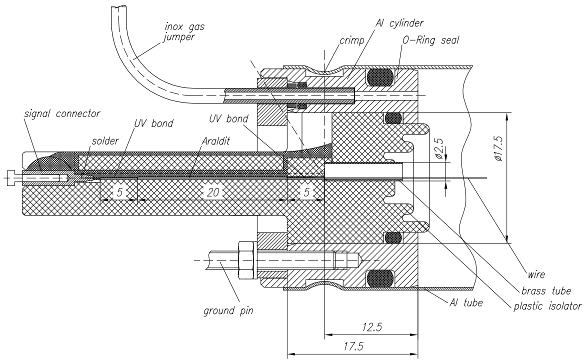

Figure 2.3: Longitudinal section of a MDT endplug

2.2.1 Detection of charged particles in the gas

Relativistic charged particles transversing a drift tube lose energy in matter primary by ionisation and atomic excitation, producing ion-electron pairs along their paths (figure 2.4). The mean rate of energy loss of a muon when traversing a material

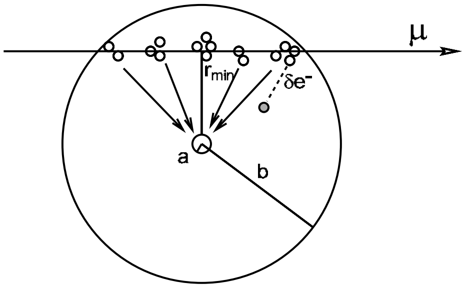

Figure 2.4: Ionisation of the gas along a track of a particle crossing the tube.

of a certain thickness δx is dependent on the particle energy and described by the Bethe-Bloch formula [28]:

$$-\frac{dE}{dx} = Kz^2\frac{Z}{A}\frac{1}{\beta^2}\left[\frac{1}{2}ln\frac{2m_ec^2\beta^2\gamma^2T_{max}}{I^2} - \beta^2 - \frac{\delta}{2}\right] \tag{2.1}$$

where K=0.31 MeV g^{-1} cm^2, Z and A are the atomic and the mass number of the absorbing material, z is the charge of the particle, γ is the standard factor $E/(mc^2)$, β^2= 1-1/γ^2, T_{max} is the maximum kinetic energy which can be transferred in a single collision and I is the mean excitation energy of the material.

The fluctuations around this average energy loss per track length in the gas follow a Landau distribution [32]. Along the path it is possible to distinguish two different types of ionisation: the primary and the secondary ionisation. The primary ionisation is a process where electrons are produced by direct collision of the incoming particle with gas atoms: a small fraction of primary electrons, the so-called δ-rays, has enough energy to travel for “macroscopic” distances creating themselves ionisation along their path. In the secondary ionisation processes the electrons are extracted from atoms either by electrons produced by primary ionisation or through intermediate excited states. Usually these secondary electrons are produced very close to the primary electrons because of their low energy, forming clusters along the particle path. As every primary interaction is independent from each other, the number of clusters per unit track is Poisson distributed. For the mixture used in the MDT, Ar-CO_2 (93:7) at 3 bar, about 100 clusters per cm are created for 100 GeV muons, each cluster containing in average three pairs. The effective average energy necessary to create an ion-electron pair mainly depends on the gas, much more than on the particle type or on its incident energy: for Argon it's about 26 eV.

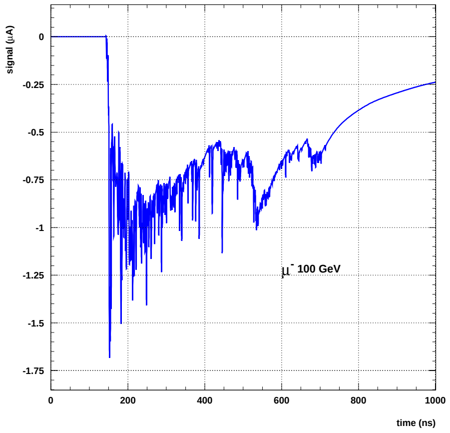

Figure 2.5: Garfield simulated signal of a 100 GeV μ as it is at the tube signal pin.

A a consequence of the cluster size fluctuations and of the non-continuous and variable distance between clusters, the signal of a muon presents typically more than one peak, as it is shown in figure 2.5: this effect is particular visible when the distance between clusters is comparable to the drift path they have to follow, as for tracks passing close to the wire. The program Garfield, used to produce this calculation, is described in more detail in 3.2.

2.2.2 Detection of photons in the gas

Photons inside MDTs have a complete different behaviour from muons. According to their energies, they interact with the gas or with the tube wall mainly in photo-electric or Compton scattering in the range below 1 MeV, as shown in figure 2.6. In the case of photons with energy below ~100 keV, the effect that dominates is the photo-electric. In this case all the photon energy is transferred to a single electron; this electron has a range of the order of few millimeters in argon at 3 bar. The signal generated on the wire from such interactions shows a clear single peak, corresponding to the energy of the incoming photon, and the measured pulse charge spectra have gaussian shapes. Figure 2.7 is the simulated signal of a 60 keV γ. For photons with higher energies, the Compton scattering [15] is the most probable process. For this process the energy transmitted to a quasi-free electron in an interaction follows the Klein-Nishina formula approximation [30]:

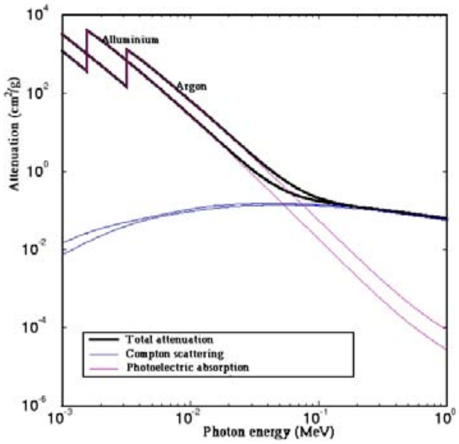

Figure 2.6: Attenuation (cm^2/g) in Aluminium and Argon

$$E_e \sim E_\gamma \int_{-\pi}^{\pi} \frac{k(1-cos\theta)}{1+k(1-cos\theta)} \tag{2.2}$$

with k=$E_\gamma/m_e c^2$. Following this formula, the maximum energy transferred, the Compton edge, is:

$$E_{e,max} = E_\gamma \frac{2k}{1+2k} \tag{2.3}$$

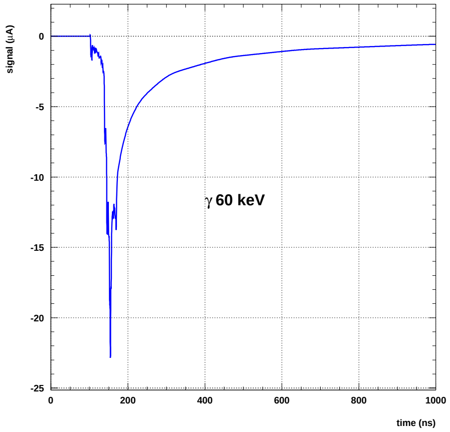

Figure 2.7: Garfield simulated signal of a 60 keV γ as it is at the tube signal pin

The signals generated from this process seems like muons, in fact in a large percentage of the events happens that the electron has enough energy to go across the entire tube and to ionise itself along its path. Figure 2.8 shows the signal generated from an ^{137}Cs γ source that emits 660 keV γ. For these interactions is difficult to predict the pulse charge spectra since not only the Compton process but also the energy loss of the recoil electron and the possibility that the scattered photon would interact again in the tube must be taken into account.

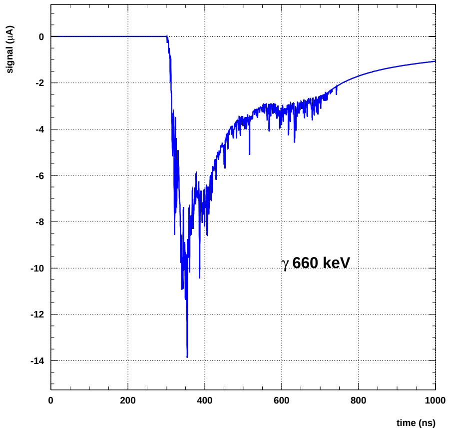

Figure 2.8: Garfield simulated signal of a 660 keV γ as it is at the tube signal pin

2.2.3 Ion-electron pairs drift and avalanche process

The electron-ion pairs created in the gas drift respectively to the anode wire and to the wall, guided by the radial electric field

$$E(r) = \frac{1}{r}\frac{V}{ln\frac{b}{a}} \tag{2.4}$$

where V is the high voltage applied to the wire, b is the inner radius of the tube and a is the wire radius. Their path is deflected from the radial direction by the Lorentz angle $\alpha{=}arctg(v_{drift}B/E)$ as the magnetic field $\vec{B}$ inside the muon spectrometer is oriented almost parallel to the wire. The drift velocity v_{drift} is the result of the concurrence of two alternating processes: the acceleration due to the above mentioned electric field and the loss of kinetic energy in collisions with gas atoms. The mobility $\mu = v_{drift}/E$ for electrons is found to be a function of E, thus velocities as high as 10^6 cm s^{-1} can be reached, while for positive ions depends on the ratio E/P, the reduced electric field, up to relatively high electric field: for Argon is about 1.53 cm^{2}V^{-1}s^{-1} and can be assumed constant inside an MDT except for the avalanche zone near the wire.

In figure 2.9 the drift velocity (μm/ns) of electrons in a MDT in standard conditions

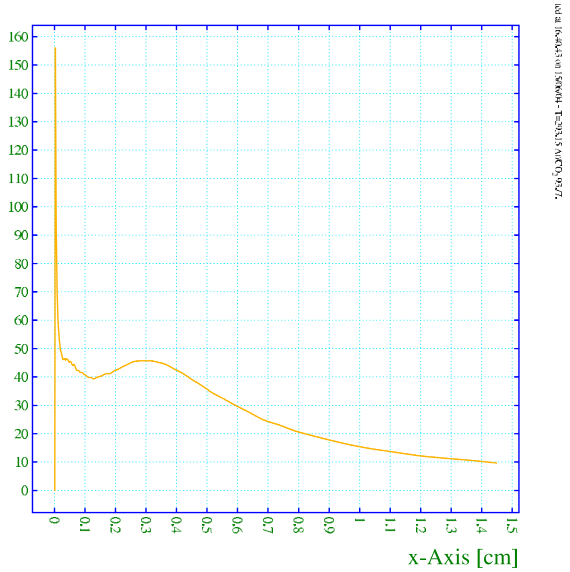

Figure 2.9: Drift velocity of electrons in a MDT as a function of the distance from the wire. The drift velocity is expressed in μm/ns

is plotted. Since the v_{drift} is not constant but depends on r, one of the crucial points of the MDT detectors is to have their calibration, the r-t (radius-time) relation, to be able to reconstruct the correct position of the tracks: the r-t relation must be known with an accuracy not higher than 20-30 μm to achieve the physics goals explained before. When the electrons reach the high-field region close to the wire they gain enough kinetic energy to cause secondary ionisations that again are able to ionise other atoms, starting an avalanche process. The increase of number of free electrons over a path dl is $dN = \alpha\ N\ dl$, with α known as First Townsed coefficient that depends strongly on the gas mixture and on the electric field. The gas gain in principle could be calculated with

$$G = e^{\int_a^{r_{min}} \alpha(r)dr} \tag{2.5}$$

where a is the radius of the wire and r_{min} is the minimum radius where the avalanche process starts. Since in 2.5 small uncertainties on the knowledge of $\alpha(r)$ lead to large errors on the calculations of the gain, is better to calculate the gain at the anode wire is used the Diethorn formula [39], an empiric parametrization of the gain:

$$G = \left[\frac{V}{a \cdot ln\frac{b}{a} \cdot E_{min}(\rho_0) \cdot \frac{\rho}{\rho_0}} \right]^{\frac{ln 2 \cdot V}{ln\frac{b}{a} \cdot \Delta V}} \tag{2.6}$$

In 2.6 the assumption that α is proportional to E is made. For the MDT operating mixture Ar-CO$_2$ 93:7, the parameter E_{min}, the minimum electric field at which the gas amplification process starts, is measured to be 24 kV/cm and ΔV 34 V. The Atlas MDT gas gain is typically $2{\cdot}10^4$.

2.2.4 Signal formation

As explained in the previous section, when an electron drifts in the high-field region. an avalanche process sets up producing ion-electron pairs. The positive ions cloud moves from the avalanche zone towards the cathode, inducing a current in the anode wire, as the electrons do by drifting to the wire. The current induced i from a moving charge q can be calculated by the Ramo theorem [36]:

$$i(t) = \frac{q}{V} \cdot v(t) \cdot E(r(t)) \tag{2.7}$$

where V is the potential, v its velocity and E the electric field. However, since the drift distance covered by the electrons is only as big as the amplification zone near the wire, about 100 μm, the signal induced by the electrons is a sharp spike of about 100 ps containing very little charge. Thus the contribution of electrons at the total signal is negligible compared to the contribution of the ions. Substituting in 2.7 the v of the ions, the pulse of a single ion is:

$$i(t) = \frac{q}{2ln\frac{b}{a}} \cdot \frac{1}{t + \frac{a^2}{2\mu V}ln\frac{b}{a}} \text{ for } 0 < t < t_{max} \tag{2.8}$$

where t_{max} is the arrival time of the ion at the cathode, of the order of some ms.

The current signal is then read out from one side of the tube, amplified, shaped and then sent to a discriminator. The complete electronic chain of the signal will be described in detail in the next section.

2.2.5 The on-chamber readout electronics

A simplified model of the tube with the High Voltage distribution and the on chamber readout electronic is shown in figure 2.10. The total induced signal on the wire is the sum of several signals like 2.8 arriving at different times: a derivator circuit with a small time constant cuts the long tail of the signal so the resulting signal at the tube signal pin is thousand time less than the total ion drift time. A simulated current and voltage signal is shown in figure 2.11 as it is at the tube signal pin. The amplification, the shaping, the discrimination of the tube signal and the digitization of the time informations are performed by two chips, the ASD and the AMT [19]. These chips are mounted on a front-end board (mezzanine) which is connected directly to the tubes. The different mezzanines are read out via the CSM, the Chamber Service Module, which is a board mounted on the chamber and connected to the ROD (Read Out Driver) via optical link. The CSM performs both the data collection and the initialization of the parameters of the ASD and of the AMT. The block diagram of the ASD is shown in figure 2.12.

Each tube signal pin is connected to a pre-amplifier while a second pre-amplifier is inserted to provide DC balance and common-mode rejection of noise. Then the signal is sent to a series of three differential amplifiers that provide gain and shaping of the signal. The amplified and shaped signal is split and sent to the Wilkinson ADC and to a discriminator. The Wilkinson ADC integrates the signal in a programmable time gate (8-45 ns) and stores the charge in a capacitor that is discharged with a constant run-down current: the discharge time is proportional to the signal charge. The Wilkinson ADC information is used to apply offline time slew correction to improve time resolution.

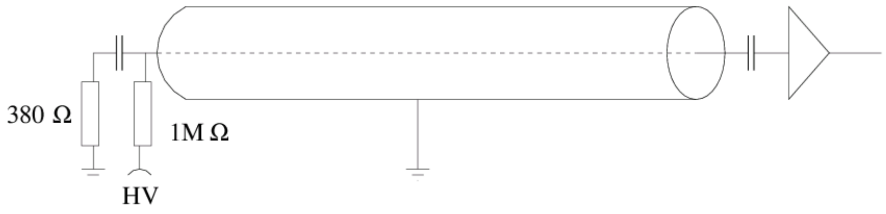

Figure 2.10: MDT frontend schematic as presented in the TDR

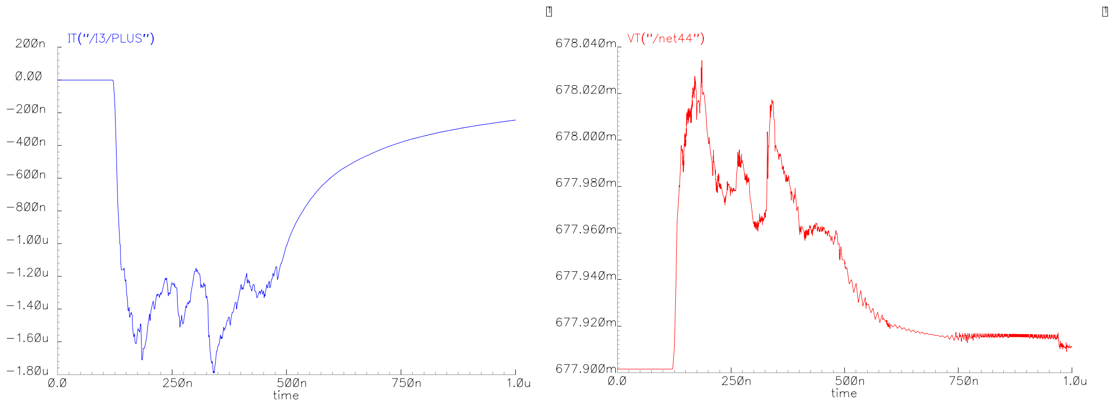

Figure 2.11: P-spice simulation of the signal at the input of the ASD [19]. On the left the current induced on a MDT wire as seen at the tube signal pin, on the right the voltage at the ASD input pad assuming a simple electrical model of the tube including the termination resistor and the coupling and parasitic capacitances.

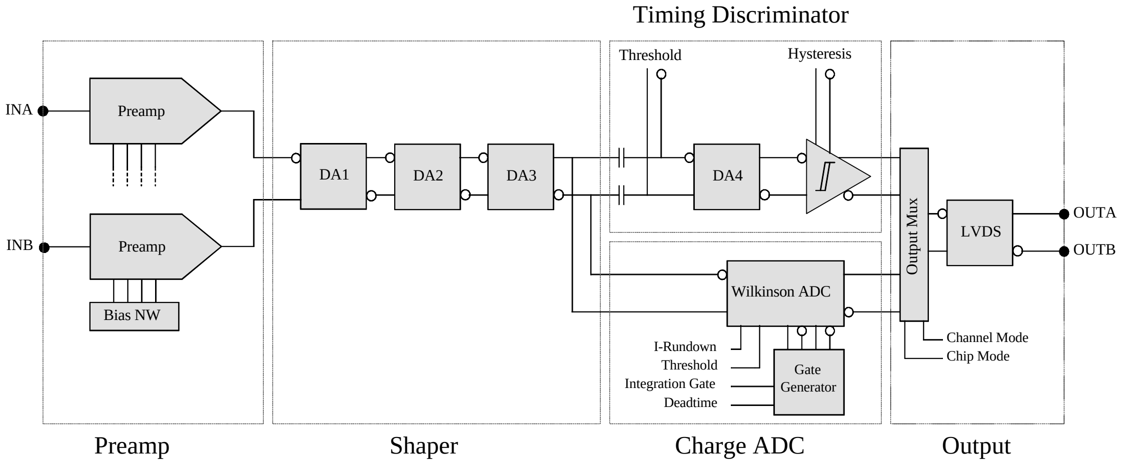

Figure 2.12: The MDT ASD block diagram [19].

The discriminator measure the time of the leading edge of the signal when it becomes higher than a programmable threshold. The value of the threshold is chosen taking into account the value of the electronic noise, that usually is expressed in terms of equivalent noise charge[1] ENC. The signals generated by the ASD are sent to the AMT chip, which is a 32 channel programmable TDC. The AMT works with a 5-bit interpolator and it is clocked at the LHC frequency of 40 MHz, so the least count is 25/32 of ns. The function of this AMT TDC is to measure the starting time of the signal respect to an external trigger that receives through the CSM. As already mentioned, these times coming from the tubes which were crossed by particles, knowing the local drift velocity to convert the time in position, are used to reconstruct the exact position of the tracks in the muon spectrometer.

In the last prototype version of the front-end electronics, the previous version before the final production version, the CSM was a VME board and the ASD had a different transfer function: a detailed description of the differences between the final version of the ASD and the last ASD prototype version, the ASD-lite, is given in 4.6, where we explain also the choice of using the ASD-lite instead of the final ASD to better study variations of the gain due to ageing effects, the main subject of this thesis.

---

[1] The ENC is the number of equivalent electrons which generate a signal equal to the r.m.s. of the noise.

2.2.6 The MDT alignment system and mechanical precision

Since the position of a muon track is measured relatively to the wires position in a chamber and also relatively to the chambers position in the different projective towers, it becomes crucial to know these informations to be able to reconstruct the tracks. Given the large scale of the muon spectrometer and the big number of chambers, it would be extremely difficult to keep the geometry of the chambers and their positions stable on the scale of the tracking accuracy required of 50 μm.

Therefore a different approach was chosen for alignment: the chambers will be positioned with low precision, on the millimeter scale, while their movements and deformations will be continuously monitored by an optical alignment system with a precision better than 20 μm. The measured deviations from the ideal geometry will be used as corrections for the muon tracking procedure. In the Atlas muon spectrometer several kinds of alignment systems can be distinguished depending on the different type of characteristics they monitor. The in-plane system monitors single MDT chamber deformations. The praxial system monitors the relative movements of different chambers in one half barrel octant. The projective system monitors

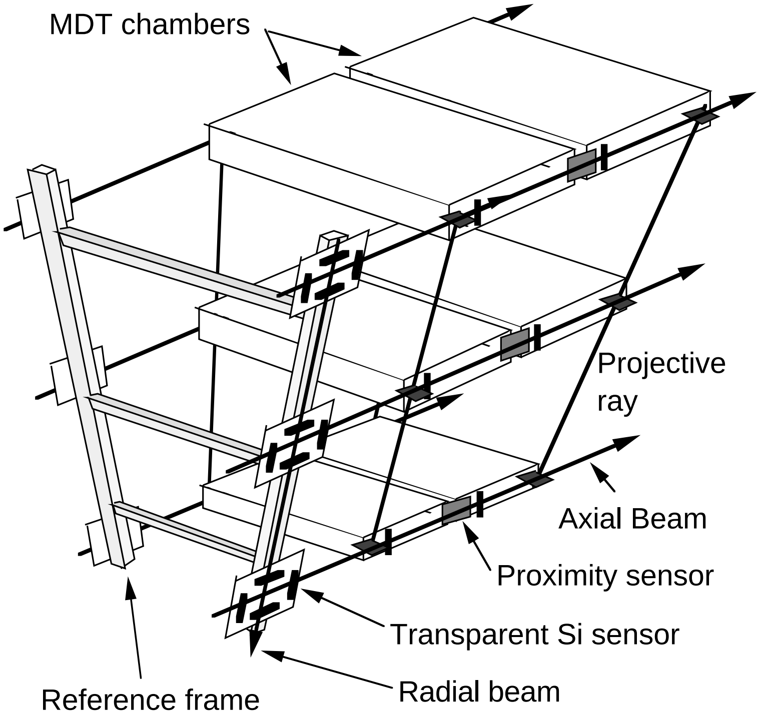

Figure 2.13: Three dimensional view of the projective alignment system of one half octant interconnecting the three barrel stations. The axial alignment lines interconnecting adjacent chambers are visible for BML chambers.

the relative displacements of the three MDT barrel stations. All these systems use different combinations of Rasnik monitors [13].

One other contribution to the precision of the reconstructed muon tracks is the precision with which the grid of wires within each MDT chamber is known. The target precision of the wire positions in an MDT should be 20 μm. A dedicated apparatus, the X-ray tomograph [20], has been developed at CERN to verify the mechanical precision of the MDT chambers.

Only a small fraction of all the MDT can be X-ray inspected at the tomograph, but all the chambers are expected to be certified in a **cosmic rays test stand**. We can therefore try to optimize the chamber geometrical parameters from the analysis of the cosmic rays data.

In the next chapter the Monte Carlo evaluation of the performances of a cosmic rays test facility is described in detail.

2.2.7 The on-chamber gas system

The on-chamber gas distribution system supplies the gas from a single input directly to each tube and collect their output in a single output: this kind of distribution is called *fully parallel*. The input and the output lines of the gas ends into two volumes called gas bar. Each tube is connected to these gas bar with the help of stainless steel tubelets which end in plastic “jumpers”, as showed in figure 2.14. Each jumper fits over an MDT endplug. The plastic used for the jumpers is Pocan[2] and the o-rings used are of EPDM[3]. The use of sealant compounds and of glue was avoided to minimize the risk of chamber ageing due to contaminations.

2.2.8 The Gas Recirculation system

With a gas volume of 754 m^3 at 3 bar absolute, the Atlas MDT becomes one of the hugest gaseous detector ever built. This large gas volume has to be replaced continuously to avoid degradation in chambers performances due to accumulation of unwanted gas constituents. These contaminations come from back diffusion through unavoidable leaks, from materials in contact with the gas, from diffusion through end-plugs or o-rings, or also from chemical reactions following the ionisation process. In table 2.1 are reported the gas system specifications.

Although the chosen MDT operating mixture, Ar-CO_2 93:7, consists of inert

---

[2] Pocan: polybutylenterephthalate produced by Bayer Polymers

[3] EPDM: polymerized etylene propylene diene monomers

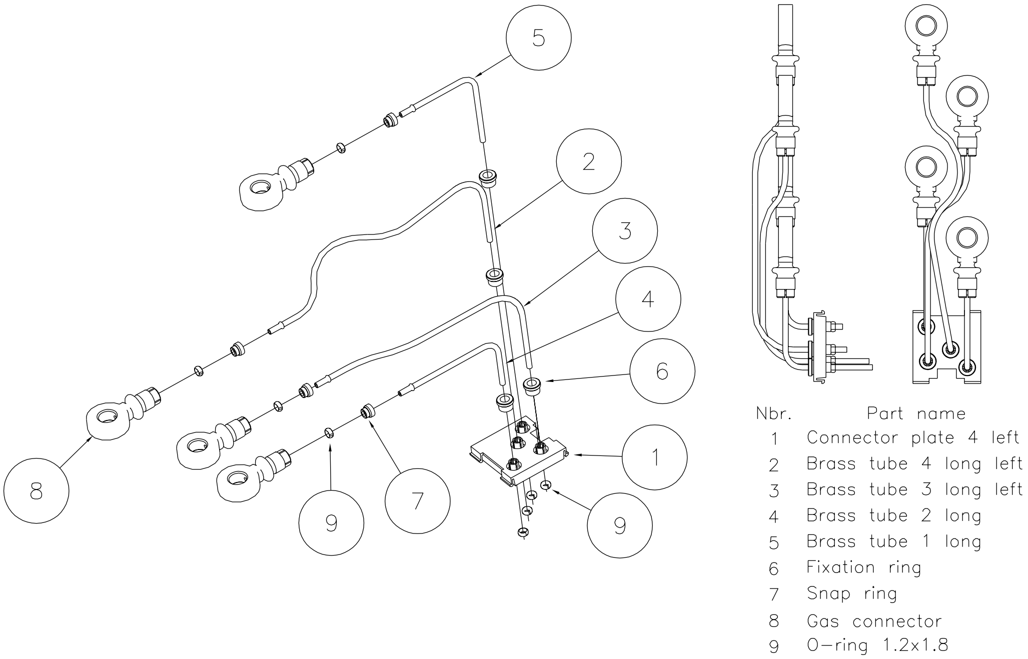

Figure 2.14: Tubelets needed for the tube connection to the gas bar.

Total Volume	754 m^3
Operating pressure	3 bar abs.
Number of chambers	682 (barrel) 512 (endcap)
Number of gas channel	112 (barrel) 162 (endcap)
Gas circulation	1 volume/day
$\Rightarrow$ Circulating flow	$\sim$ 100 Nm^3/h
Refreshing rate	10% of total volume/day
$\Rightarrow$ Fresh flow	$\sim$10 Nm^3/h
Leak rate	$\leq$ 0.1 Nm^3/h
Impurities	$\leq$ 100 *ppm* O_2
Water content	$\sim$ 500 *ppm* (max 1000 *ppm*)
Materials and components	oil-lubrificant free, no silicon

Table 2.1: The Atlas MDT gas system specification

standard gases not much expensive, financial constraints forbid to use the gas only once. Thus the gas circulation through the MDT will be 1 volume per day, while the refreshing rate will be the 10% of the total gas volume. The fresh gas exchange was chosen as low as possible, but large enough to suppress such contamination effects.

Evaluation, in an environment similar to the Atlas one, of the ageing effects caused by such contaminations, in particular those due to the improper usage of oils or lubrificants containing silicon, was the main goal of this Thesis.

The Argon Turbo Circulator

As a consequence of the specifications for the gas system, the choice for a suitable gas compressor is limited by several factors:

- High flow rate, nominal of 100 Nm^3/h, maximum 200 Nm^3/h, but also usable to lower flow rates whenever a sub-distribution system have to be stopped.
- Gas mixture density of 4.95 $\mathrm{Kg/m}^3$.
- The compressor must be able to compensate a minimum pressure drop of 0.3 bar due to the pass of the gas through all the components of the gas system, like the pipes, the flow adjustment valves, the flowmeters, the optional purification system and the chambers themselves.
- High reliability: the compressor must be able to operate for more than 8 months per year with nearly no interruption.
- Strict purity requirements have to be fulfilled to keep the performances of the MDT chambers over years of LHC operations. No grease, neither oil, nor organic solvents nor any kind of silicone compounds should ever be in contact with the gas.

A big effort has been undertaken to find a compressor within these constraints. The selected turbine, called Argon Turbo Circulator ATC, was custom-made for Atlas by the company ATEKO. The design of this circulator was done according to the specifications mentioned above: materials in contact with the gas are only metals and no lubrification is needed. During operation the rotor shaft with the wheel blade is held by three dynamics gas bearings, two radial and one axial. Once a rotation speed of 4000 rpm is reached, the density of the argon cushion created by the special geometry of these bearings is high enough to make the shaft hover above the bearings with a clearance of about 60 μm: the turbine rotation speed for Atlas is expected about 44000 rpm, while the maximum rotation speed is 65000 rpm. Thus there is no friction while the compressor is running, limiting the need of maintenance, but during the run up and run down phase abrasions of the bearings is unavoidable. The heat produced of about 150 W is dissipated with cooling water channels all around the compressor.

2.2.9 MDT ageing requirements

As already mentioned in 1.4.5, the main background contributions comes from photons and neutrons interactions. Figure 2.15 and figure 2.16 show the last simulation results for the photon and neutron flux in the muon spectrometer. One of the principal cause of possible degradation of the MDT is the large amount of charge which will be deposited on the anode wire. This charge is the integral of primary charge times gas gain over time:

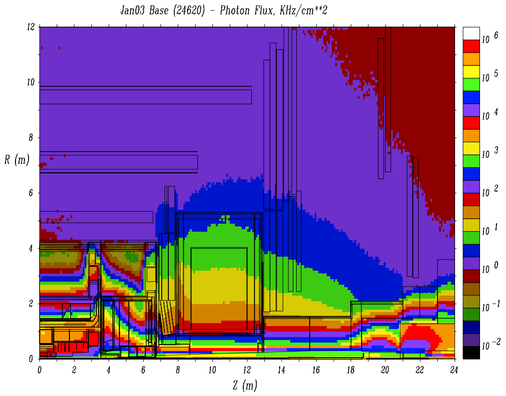

Figure 2.15: Instantaneous photons rates at nominal luminosity L=10^{34} $\mathrm{cm}^{-2}\mathrm{s}^{-1}$ for the full Atlas detector

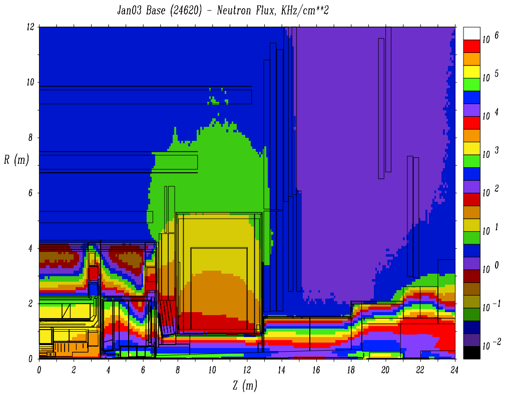

Figure 2.16: Instantaneous neutrons rates at nominal luminosity L=10^{34} $\mathrm{cm}^{-2}\mathrm{s}^{-1}$ for the full Atlas detector

$$Q = \int (R \cdot N_e \cdot d \cdot G \cdot e) dt \tag{2.9}$$

where R is the particle rate, N_e is the number of primary electrons produced per incident particle, d is the diameter of the tube, G is the gas gain and e the electron charge in Coulomb. The worst case background rate expected is 5×100 Hz/cm^2 which corresponds to 5×300 Hz/cm, where the factor 5 was introduced to allow for uncertainties in the background simulations [13]. This background rate is dominated by background hits from neutral particles, as already explained, which deposit an average energy of 32 keV per event (figure 2.17).

The number of primary ionisation, remembering the average energy of 26.6 eV per ionisation for the used gas mixture, is ∼1200. This means that, during the 10 years of LHC operations(10^8s), the maximum accumulated charge on the wire is

$$Q_{max} = 5 \cdot R \cdot N_e \cdot d \cdot G \cdot e \cdot t = 0.576 C/cm \simeq 0.6 C/cm \qquad (2.10)$$

with a gas gain of $2{\cdot}10^4$. Such an high amount of charge can produce ageing effects like chemical deposits on the anode wire surface or on the cathode tube wall.

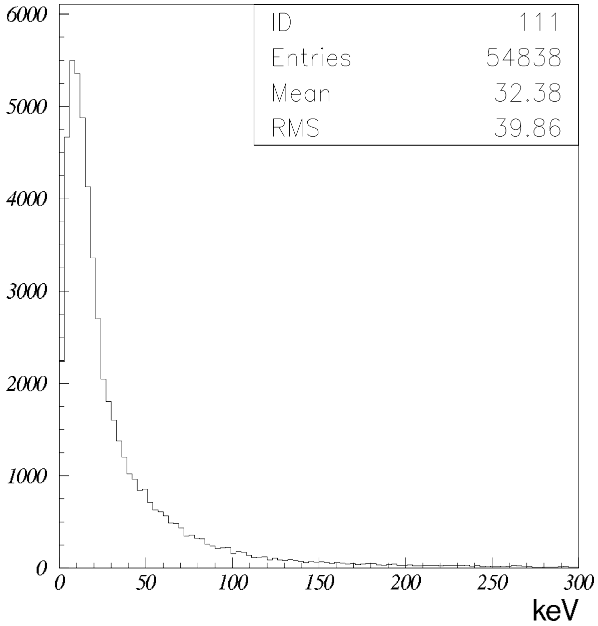

Figure 2.17: The distribution of the expected energy deposited in the MDT due to photon background

MDT ageing tests

To study the ageing effects on the MDT, several tests were performed. The results of the tests until May 2003 is briefly described in 4.3, while the last ageing test performed is described in detail in chapter 4 and 5.

2.3 MDT momentum resolution

A detailed study on the muon momentum resolution has been computed taking into account the geometry of the detectors and the distribution of the material in the spectrometer. The different contributions to the muon barrel momentum resolution are shown in figure 2.18 as a function of the transverse momentum. In the figure, only the reconstruction in the muon spectrometer is considered, contrary to figure 1.17. It is possible to distinguish three different regions:

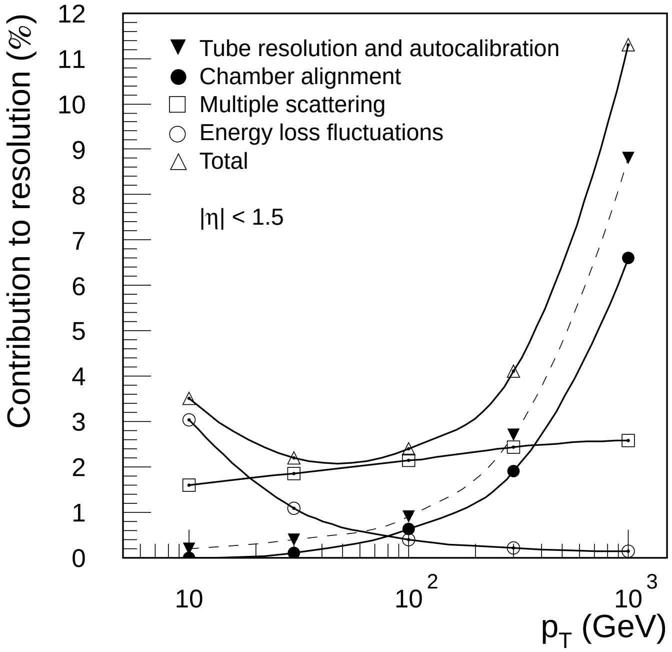

Figure 2.18: $\frac{\Delta p_T}{p_T}$ as a function of the transverse momentum up to 1 TeV for muons reconstructed in the barrel region using the muon spectrometer only.

- $P_T < 30 GeV/c$: at low momentum energy loss fluctuations in the calorimeters are dominant. These fluctuations influence the extrapolation from the muon spectrometer to the interaction point, so the inner detector, which is closer to the interaction point respect to the calorimeter, provides the more precise momentum measurement.
- $30 < P_T < 300 GeV/c$: the resolution is dominated by multiple scattering, which depends strongly on the amount and on the distribution of material along the track
- $P_T > 300 GeV/c$: the single tube resolution (80 μm) and the chamber alignment dominate the resolution

Chapter 3

A Monte Carlo evaluation of the performances of a MDT Cosmic Test Stand

The aim of the work described in this chapter is the Monte Carlo evaluation of the performances of a simple cosmic rays test facility, looking in particular to the resolution that can be obtained in the measurements of the chamber geometrical parameters. This work has already been published in an Atlas Note [5].

The high level of mechanical accuracy in the wire location respect to the whole chamber represents one of the main requirements on the characteristics of the MDT chambers.

The X-ray tomograph measurements performed till now at CERN have certified an accuracy below 20 μm on the r.m.s. of the wire position respect to the nominal position. The parameters measured in the tomograph are stored in a database and will be used in the track reconstruction phase to avoid systematic errors. Since only a small fraction of all the MDT chambers will be tomographed, for all the other MDT chambers the full wire grid measurement will not be available. However, it has been observed that it is possible to have a substantial improvement (up to 5-7 μm) in the wire r.m.s. measuring only some of the chamber geometrical parameters, like the relative distance, the rotation and the angle between the two multilayers. This is due to the better accuracy that can be obtained, at the construction level, in the wire location inside a multilayer respect to the relative positioning of one multilayer respect to the other.

More sophisticated approaches [21] trying to obtain single wire positions from mechanical measurements, offer only a marginal improvement respect to the few parameters fit and are much more difficult to perform.

As already mentioned, only a small fraction of all the MDT chambers will be tomographed, but all the chambers must be certified in a cosmic rays stand. We can therefore try to optimize the chamber geometrical parameters from the analysis of the cosmic rays data or perform the same analysis during the Atlas commissioning period with cosmic rays or during low luminosity runs. In this way we will be able to store the actual chamber parameters in the offline database and therefore to improve the resolution of the muon spectrometer.

3.1 MDT geometrical parameters

We will use in the following the standard local MDT reference system with the x along the wire, y orthogonal to the layers and z orthogonal to the wire along the tube layer, as it it shown in figure 3.1. We will also represent each track in the multilayer reference frame as a line $y = a \cdot z + b$. As we have seen from the X-ray tomograph results [26], and assuming a good internal geometry of individual multilayers, the main parameters needed for optimizing the overall chamber geometry are graphically represented in figure 3.1. They are the differences between the nominal and the actual positions of the higher (second) multilayer in the reference system of the lower (first) multilayer:

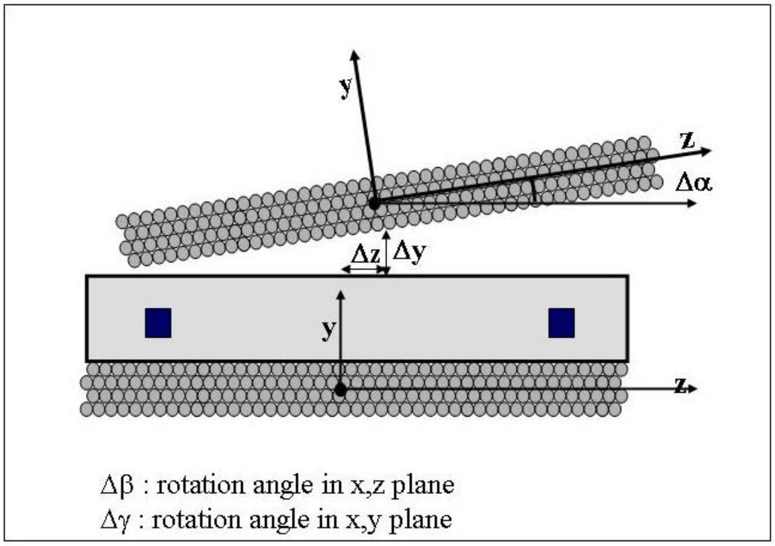

Figure 3.1: The main parameters of the MDT chamber geometry

$\Delta\alpha$ is the relative angle between the two multilayers internal reference systems, i.e. the rotation of the second multilayer with respect to the first in the yz plane of the first multilayer: $\Delta\alpha = \mid \mathrm{a}_{Multilayer1}\text{-}\mathrm{a}_{Multilayer2} \mid$;

$\Delta \mathrm{z}_0$: the z position of the origin of the second multilayer in the ref. system of the first multilayer;

$\Delta \mathrm{y}_0$: the difference between the nominal and effective separation between the two multilayers in the y direction of the first multilayer;

The knowledge of these 3 parameters at the two chamber ends (ReadOut and HighVoltage side) will allow to measure the two additional angles $\Delta\beta$ and $\Delta\gamma$, corresponding to the rotation of the first multilayer respect to the second in the x-z plane and in the x-y plane respectively. These parameters must be measured with an accuracy of few microns for $\Delta \mathrm{y}_0$ and $\Delta \mathrm{z}_0$ and of few microradiants for $\Delta\alpha$, $\Delta\beta$ and $\Delta\gamma$ in order to bring the knowledge of the overall chamber geometry at the 10 μm level of r.m.s..

3.2 Test sites and simulation tools

To validate the simulation we compared simulated data with real data taken in two different test sites: H8 and Roma3.

H8 is the name of a beam line at CERN, used to test the Atlas detector elements, among which the muon chambers. The geometrical displacement of the chambers, showed in figure 3.2, is such to reproduce a complete sector of the muon spectrometer barrel. The muon beam has a variable energy between 10 GeV to 180 GeV, and its direction (14 degrees respect to the chamber plane) can be changed of few degrees by a magnet positioned along the beam path. This setup differs from the Atlas final one also for the trigger: it was not done using the RPC positioned on the MDT, but it is done mainly by two different counters of plastic scintillator of 10×10 cm^2.

Roma3 is a site where MDT chambers type BIL (Barrel Inner Long) are equipped with the gas distribution system, the high voltage distribution and with the on-chamber readout electronics. Then these chambers undergo the Quality Assurance and Quality Control to monitor their functionality. For this test a cosmic rays hodoscope has been built [18]. It is possible to insert up to three BIL in the frame used also for their transportation. The trigger is provided by three planes of RPC, two on the bottom and one on the top of the hodoscope structure. A schematic view of this setup is shown in figure 3.3, where also the reference system, similar to the one already defined, is shown.

The Monte Carlo simulation was implemented in the GEANT 4 (version 5.2)[16] framework, in order to trace the simulated particles through the trigger detectors and the MDT chambers. The whole geometry, all the materials (including, for example, also the glue) and the signal delays have been described in detail. For the simulation of the response of a single MDT and for the hit digitization we have used the results of a Garfield Monte Carlo study [25]. Garfield [38] allows to define the geometry of the tube and the MDT operating conditions [14], and it's able to parametrize effects like fluctuations of cluster-size, cluster-position, diffusion and variations of gain.

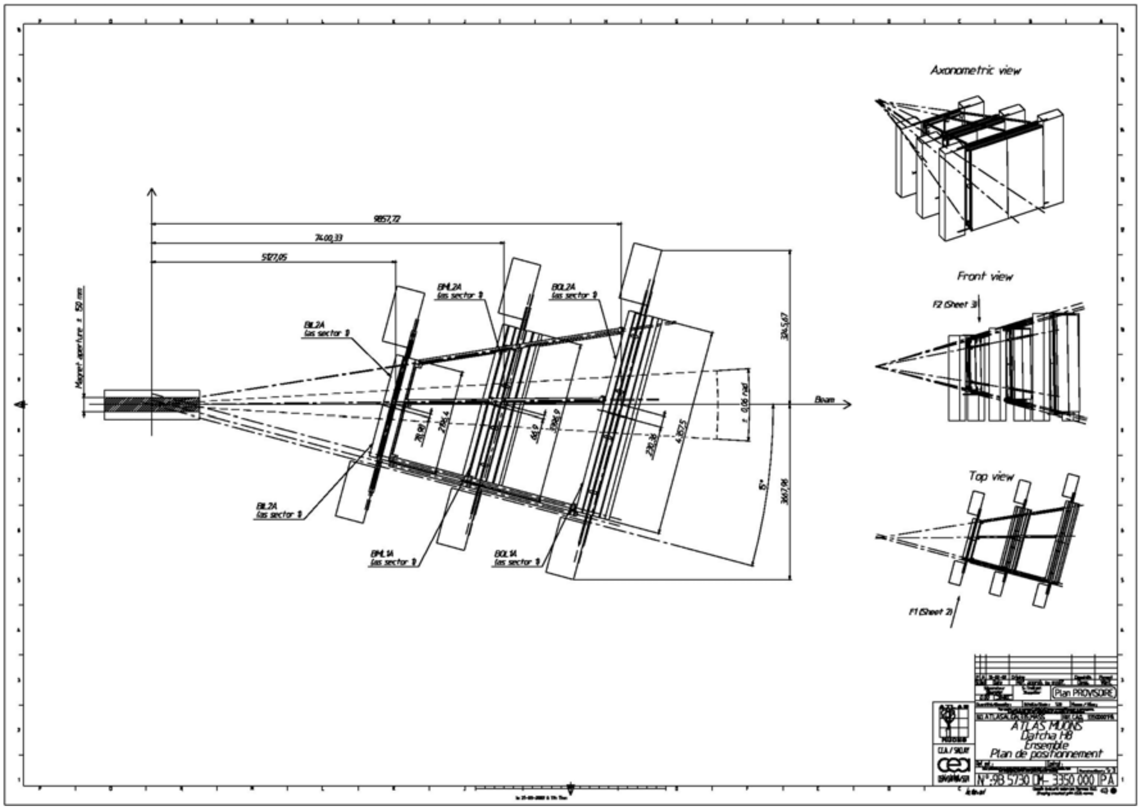

Figure 3.2: H8 setup in 2002-2003

3.3 The simulated setup and the MDT chamber description

The simulated cosmic test set up, almost identical to the Rome3 cosmic test facility, is shown in figure 3.3: 3 planes of RPC counters are placed in a tower 2.5 m high, one plane on top and two planes at the bottom at 12 cm distance with 5.5 cm of lead in the middle, providing a fast cosmic trigger with a resolution in time of about 1 ns. This trigger hodoscope covers an area of 2.8 x 1.2 m^2 and houses up to three MDT chambers of the BIL (Barrel Inner Long) type. Along the tubes the trigger counters are segmented in 6 sub-towers. Only the two extreme sub-towers will be used for the study of wire positions near the end plugs. In this way we avoided the risk to have cosmic rays at a wide angle respect to the x axis, thus we can ignore possible $\Delta\gamma$ rotations.

The wire positions have been smeared around their nominal locations with a r.m.s. of 10 μm both in z and in y to simulate the accuracy on the mechanical construction of the tubes.

Figure 3.4 shows the correlation between the simulated drift time and the perpendicular distance of the track from the wire. The correlation function, the r-t, is obtained from the Garfield simulation. The events below the correlation band are due to δ-rays produced in the gas and reaching the wire before the ionization of the primary charged particle. After removal of these events, the distribution function of the drift time, for a given radial distance, is well described by a gaussian, even at small distances from the wire. We recompute the r-t function by the reconstructed tracks in a similar way as with real data. This function is then used in track reconstruction.

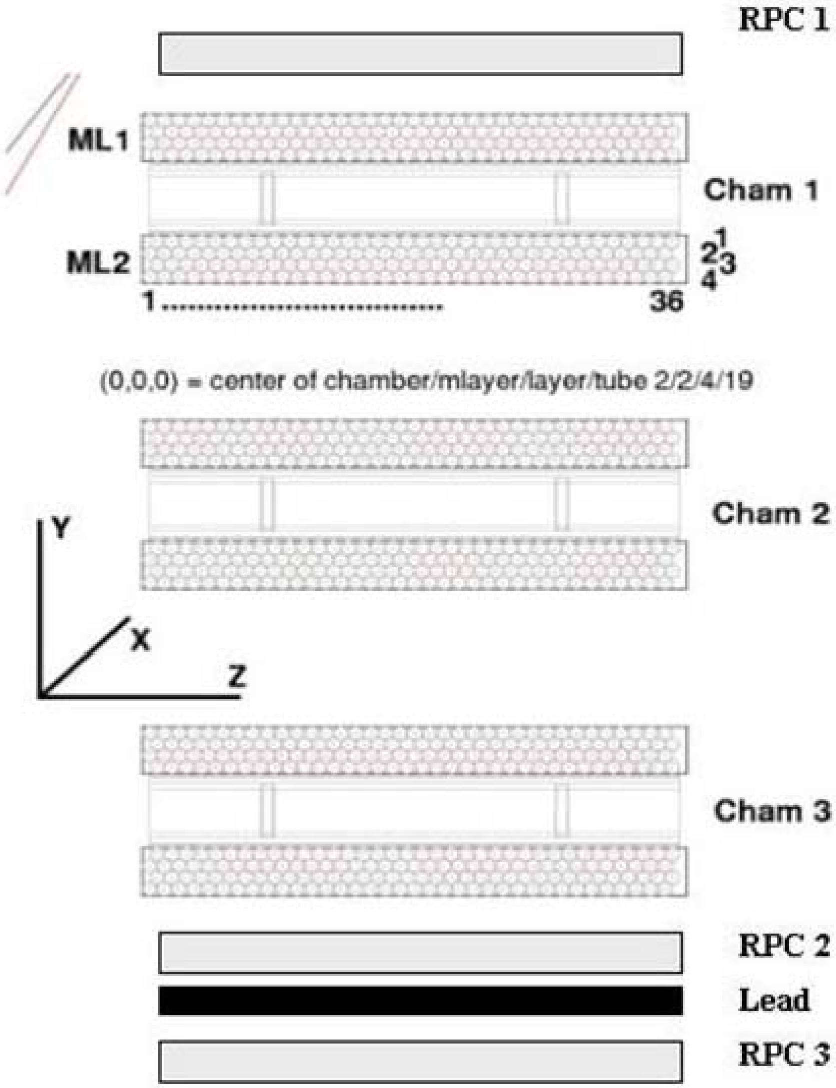

Figure 3.3: Layout of the simulated cosmic ray stand, similar to the Roma3 one

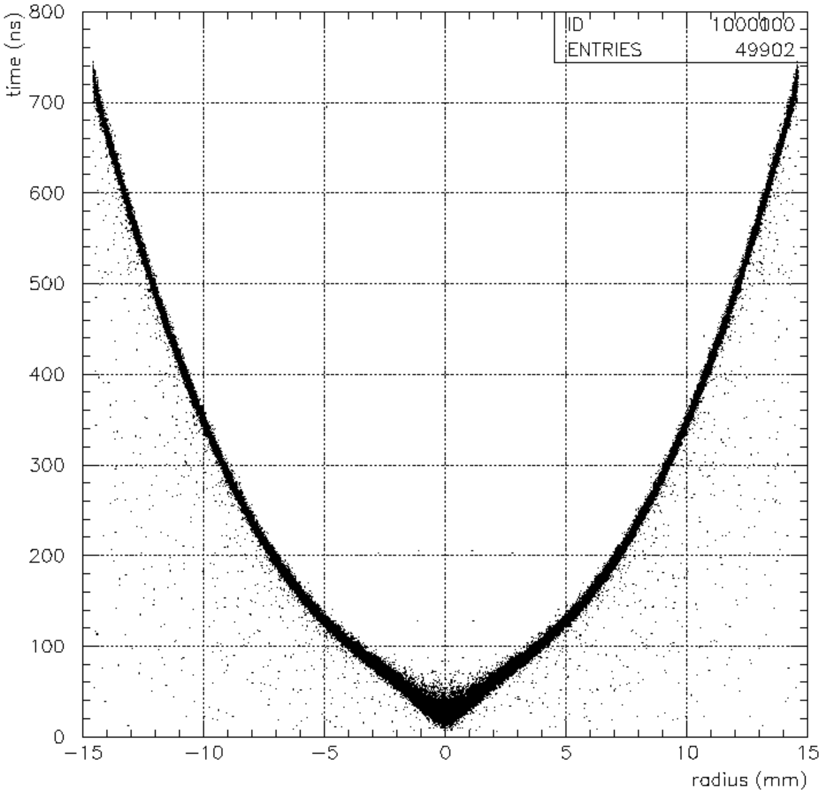

Figure 3.4: Drift time as a function of the distance of the track from the wire obtained from the Garfield simulation

3.4 Test with high-energy muons

In order to validate the GEANT4 Monte Carlo generation and the reconstruction software without the additional complications coming from the low momentum tracks of the cosmic muon spectrum, high energy muons were used; we have generated a sample of 103 k high energy muons (180 GeV/c), with a geometrical configuration very similar to the one in H8 test beam (10 × 10 cm^2 trigger counter, angular spread 0.1 mrad both in y-z and y-x planes, chamber at 14 degrees respect to the y axis)[23].

We have analyzed one of the two multilayers and requested, at the pattern recognition level, one and only one "string" of hits without additional hits, where a "string" is defined as 4 contiguous tubes fired, one in each layer. This request reduces the initial sample to 96 k events. The loss, about 7% of the events, is due both to geometrical inefficiencies (< 1% at this impact angle, as expected from the tube walls) and to the presence of extra hits associated to the production of high energy rays within the multilayer itself. As a comparison we have applied the same selection to the H8 data at the same energy. Masking noisy channels and avoiding regions with known dead channels, the "string" request rejects about 14% of events; inefficiencies are in agreement with MC expectation while the fraction of events with extra hits shows a sizable discrepancy (13% compared to 6%) which is due to some GEANT4 underestimation of the production with the default cuts. Discrepancies of the same size appear also in the comparison between measured drift times. In fact, the effect of high energy rays is twofold: the extra particles affect both the number of hits, when entering a tube not crossed by the primary particle, and the

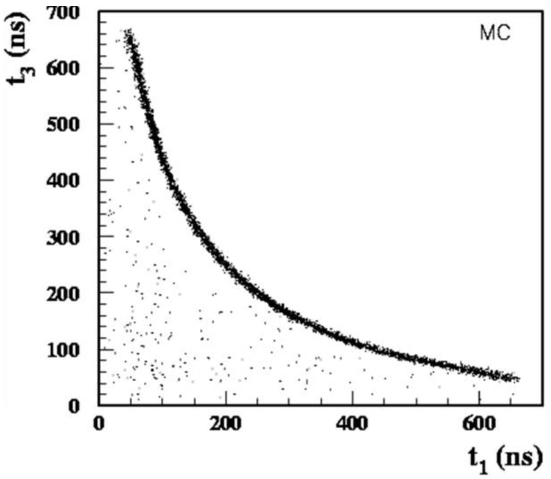

Figure 3.5: t_1 vs t_3 from 180 GeV/c MonteCarlo data

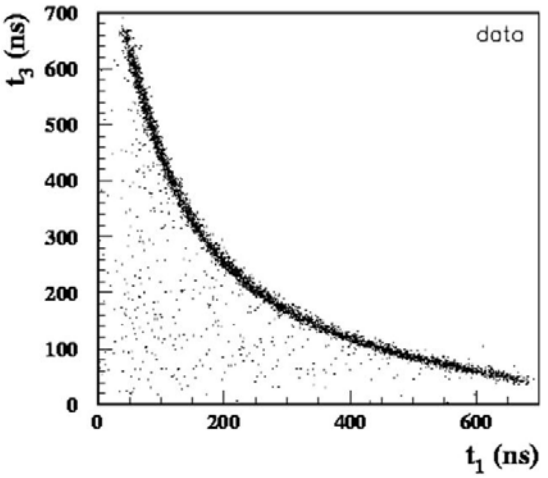

Figure 3.6: t_1 vs t_3 from 180 GeV/c H8 data

measured drift time, when entering a tube already crossed by the primary particle and spoiling its drift time measurement. The number of hits spoiled by the presence of a ray can be estimated from the plot of t_1 versus t_3, where $t_{1,3}$ are the drift times observed in layer 1 and in layer 3, figures 3.5 and 3.6.

In these plots, thanks to the very small angular spread of the beam, the good hits lye on a clear correlation band while the points below the band are events in which at least one of the two drift times is due to a δ-ray. From figure 3.5 the fraction of spoiled hits per tube in the simulation is 2.5% (means 10% for a track). The same plot for the test beam data, as shown in figure 3.6, gives an higher probability 4.5%(i.e.17% for a track), pointing again to an underestimation of the ray production in the simulation. It is worth to mention that these cuts are applied in order to produce a very clean sample, to be used for calibration. The actual cuts which will be used with real data tracks for the physics analysis, will be much less severe (e.g. three aligned hits in a multilayer) and the inefficiencies will be much smaller.

For the track reconstruction of simulated events we have used the time to radius relation and the corresponding resolution coming from [25]; the t_0, the time corresponding to a track very near to the wire, has been obtained from the fit of the leading edge of the drift spectrum, shifting the origin in order to reproduce the t_0 obtained from the Garfield simulation (t_0 = 23 ns). The track fit $z = a \cdot y + b$ to

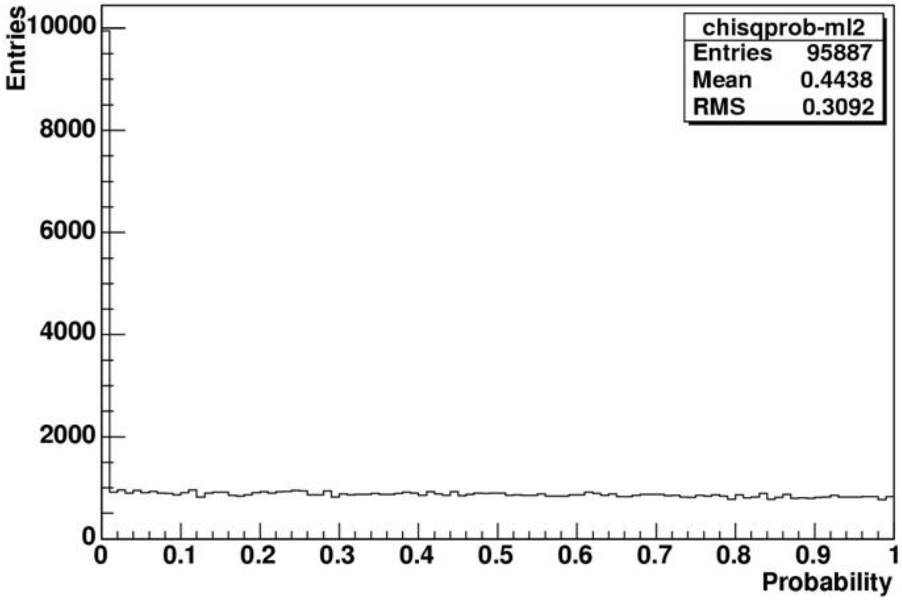

Figure 3.7: $P(\chi^2)$ distribution for the fitted tracks from MonteCarlo simulation at 180 GeV/c

the radial circles uses the same algorithm described in [40], with y,z origin in the center between the two multilayers. The resulting χ^2 probability distribution, for the simulated tracks, is shown in figure 3.7; apart for a large peak at very low probabilities the distribution is flat, showing that the simulation and the reconstruction algorithms are internally consistent. The peak at low probabilities corresponds to the δ-ray production in the gas or in the tube walls; a cut at $\chi^2 < 9$ ($P(\chi^2)<0.01$ for 2 degrees of freedom) removes ~9 k out of 96 k tracks, corresponding to a probability of a δ-ray spoiling the track hit of 9% in agreement with the fraction estimated from the plot of t_1 versus t_3. Figure 3.8 shows the straight line fit parameters a and b compared to the generated values (a_{fit}-a_{gen}, b_{fit}-b_{gen}). After the $P(\chi^2)$ cut the single multilayer resolutions are $\sigma_a = 1.64$ mrad and $\sigma_b = 234$ μm for a and b respectively. The pulls, defined as $(\text{Value}_{Generated} - \text{Value}_{Reconstructed})/\sigma_{fit}$, are shown in figure 3.9; their fit with a gaussian shape gives values compatible with $m = 0$ and $\sigma = 1$ in both cases, showing the good quality of the reconstruction and the correct estimation of the errors on a and b.

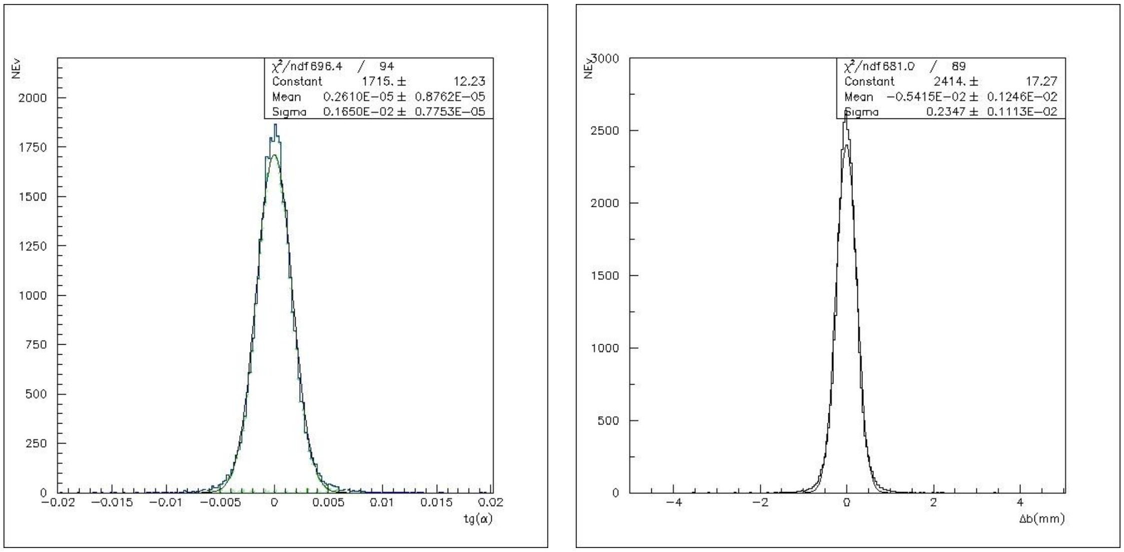

Figure 3.8: The track fit parameters a and b compared to the generated values

H8 data were reconstructed using the t-r relation and resolution produced by CALIB[24]. The χ^2 probability distribution is shown in figure 3.10. It is similar to the one obtained on simulated data but the size of the peak at small probabilities gives a probability of a ray spoiling a track hit of 17%, in agreement with the fraction estimated on H8 data from the plot of t_1 versus t_3. Finally the autocalibration procedure used by CALIB to compute the t-r relation and the spatial resolution was checked on a simulated sample of 180 GeV/c muons with a wider angular distribution (σ_a=0.1 rad). The angular spread of the tracks of the used sample is in fact essential

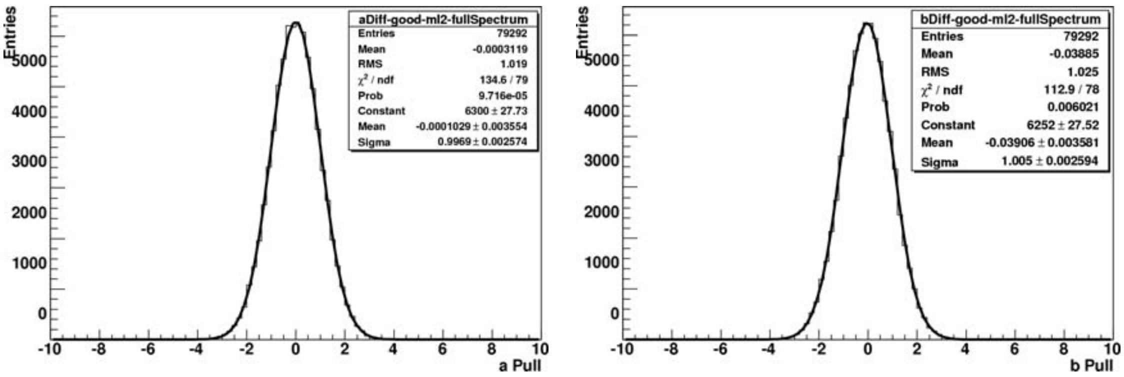

Figure 3.9: Pulls on track parameters a and b for tracks with the $\chi^2 < 9$

for the convergence of the autocalibration algorithm. The resulting time-to-radius has been compared with the one used in the generation; in figures 3.11 and 3.12 the difference of the two is shown as a function of the drift time and of the distance from the wire. The discrepancies are typically at the level of 1 ns or 20 μm, showing the good performance of the autocalibration procedure.

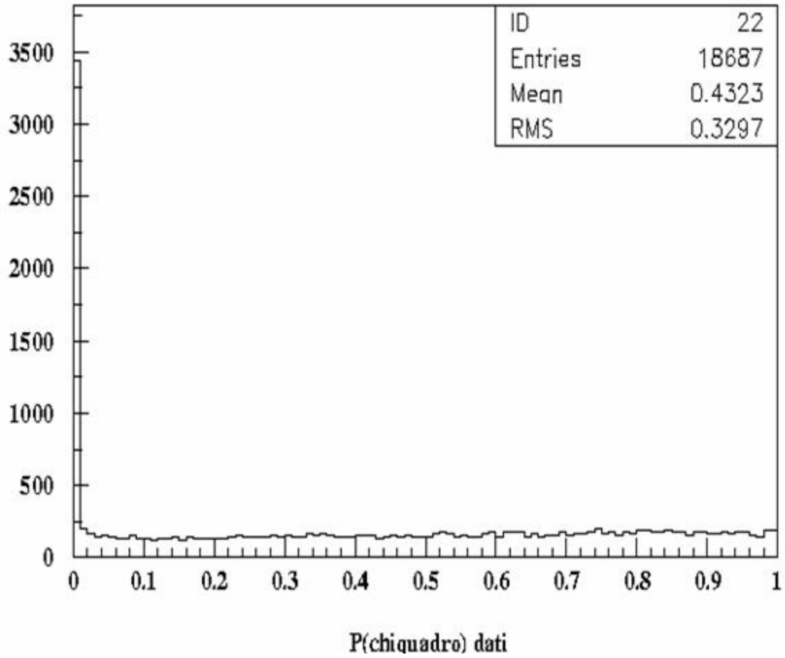

Figure 3.10: P(χ^2) distribution for the fitted tracks from H8 data at 180 GeV/c

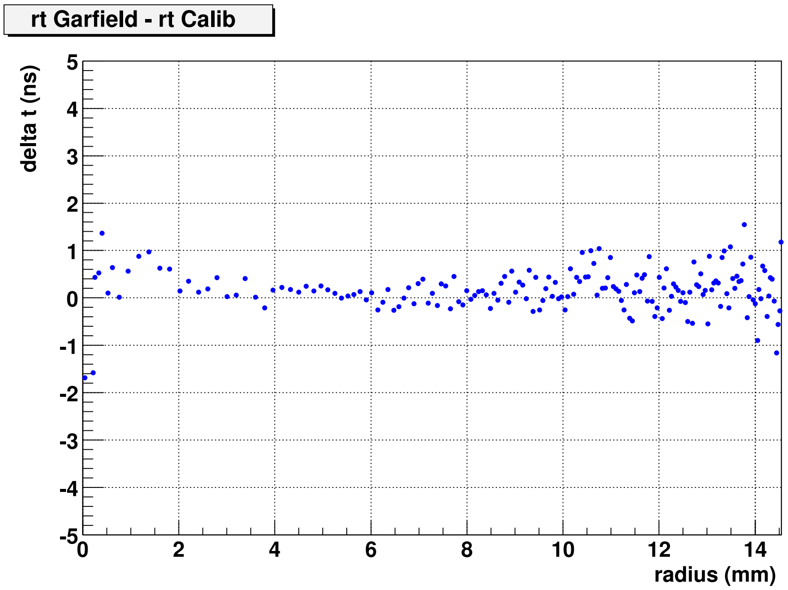

Figure 3.11: Difference between the time to radius from Garfield and the one obtained from CALIB calculated at fixed radius interpolating the time

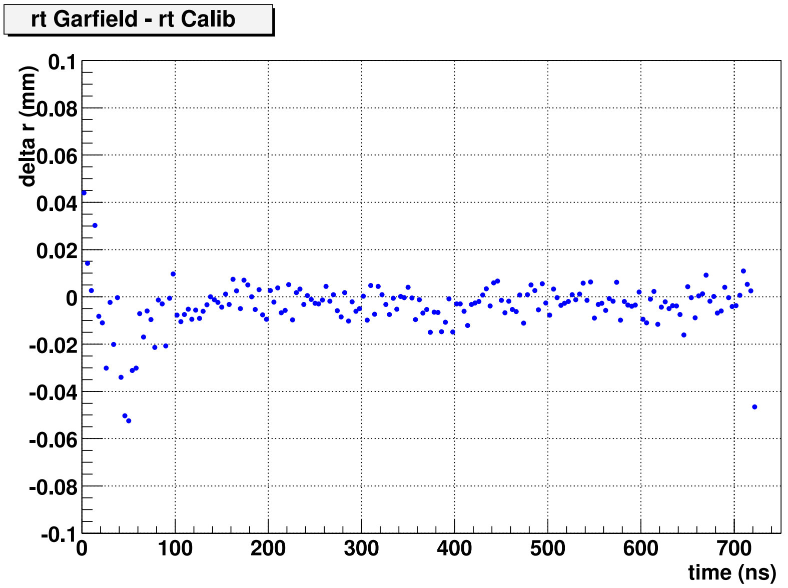

Figure 3.12: Difference between the time to radius from Garfield and the one obtained from CALIB calculated at fixed time interpolating the radius

3.5 The Monte Carlo simulation of the cosmic test stand

The cosmic spectrum from experimental measurements at sea level for vertical muons [17] has been used to simulate the behavior of the cosmic test stand. The angular dependence of the momentum spectrum has been neglected; as a result the average momentum of the simulated muons is slightly underestimated. In figure 3.13 the angular coefficient of the triggered tracks is shown. Three MDTs have been inserted in the tower but only the data from the middle chamber and from the first trigger sub tower have been used in the analysis. A total of ∼120 k triggers have been generated in the same conditions as in the previous paragraph; no electronic noise has been introduced.

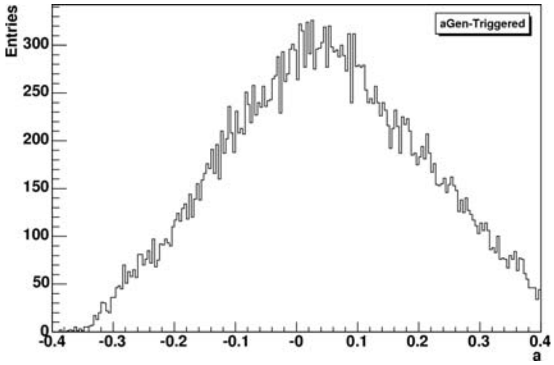

Figure 3.13: Angular coefficient of the triggered tracks.

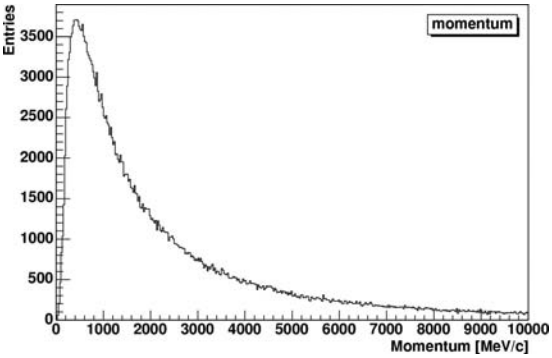

Figure 3.14: The momentum spectrum of the triggered tracks in the cosmic ray test stand

The trigger acceptance, defined as the number of events with at least 1 hit divided by the total number of triggers, is 94%, in good agreement with the real data (93%). The momentum spectrum of the triggered tracks can be seen in figure 3.14; the cut introduced by the 5.5 cm lead absorber is clearly visible. The fraction of events with at least 4 hits divided by the number of events with at least 1 hit, is 91%, to be compared with 93% for the cosmic data, corresponding to the expected geometrical inefficiency of the detector for tracks with a wider angular distribution.

For the t-r relation and resolution we have used the CALIB results on the same sample; with a final cut on the $P(\chi^2) > 0.08$ and at least 20 iterations, we obtain a t-r relation in agreement, at the 20 μm level, with the generated one. The $P(\chi^2)$ for tracks reconstructed in multilayer 1 is shown in figure 3.15; as expected the multiple scattering contribution to the hit resolution of the low energy muons results in an underestimation of the uncertainty in the track position, as it is clear from the slope of the distribution towards low probabilities.

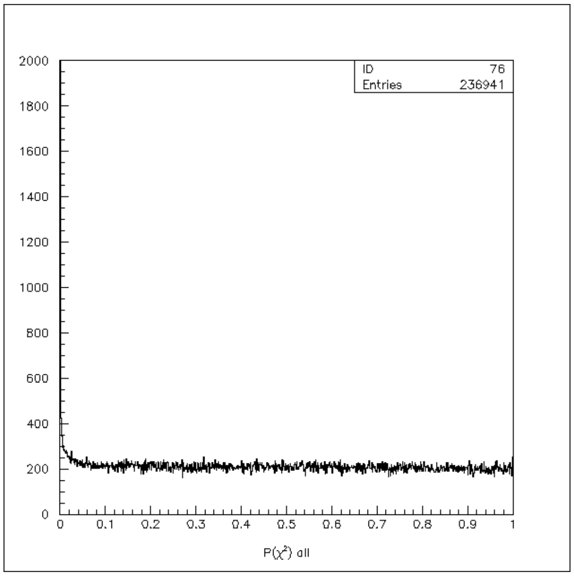

Figure 3.15: P(χ^2) distribution for the fitted tracks from the MonteCarlo simulation of the cosmic ray test stand.

The very low momentum muons, together with the δ-ray production in the tube, are responsible for the large peak below 10% probability. If we accept the tracks with P(χ^2)> 8%, the track reconstruction efficiency (defined with the "at least 4 hits" cut) is 65% and the pulls in a and b, showed in figure 3.16, have a σ of 1.4 and of 1.3 due to the neglected multiple scattering contribution. The effective resolution on a and b (generated reconstructed) is shown in figure 3.17; from a gaussian fit we get 2.3 mrad resolution on a and 296 μm on b. Reconstructing now the tracks independently in both multilayers we can compare the a and b obtained in the two multilayers; the difference between the two is shown in figure 3.18; the sigmas are, as expected, 1.4 times the results of the single multilayer.

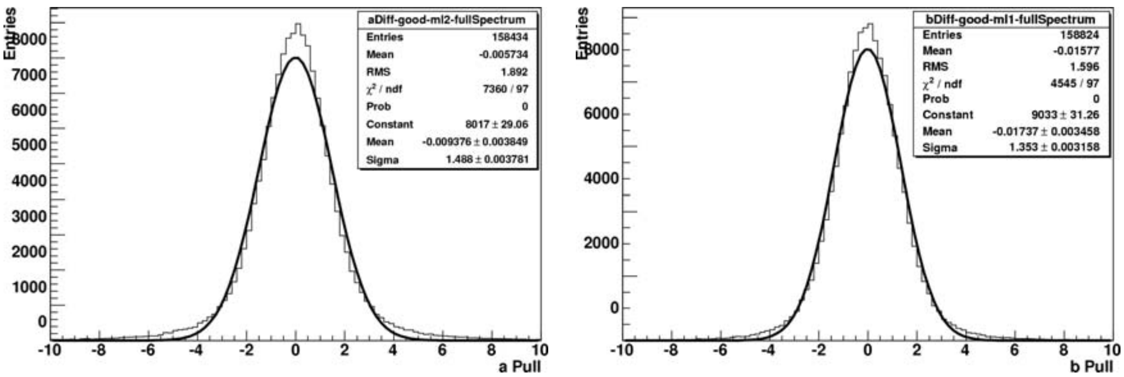

Figure 3.16: Pulls on cosmic-track parameters a and b for tracks with the $\chi^2 < 8$

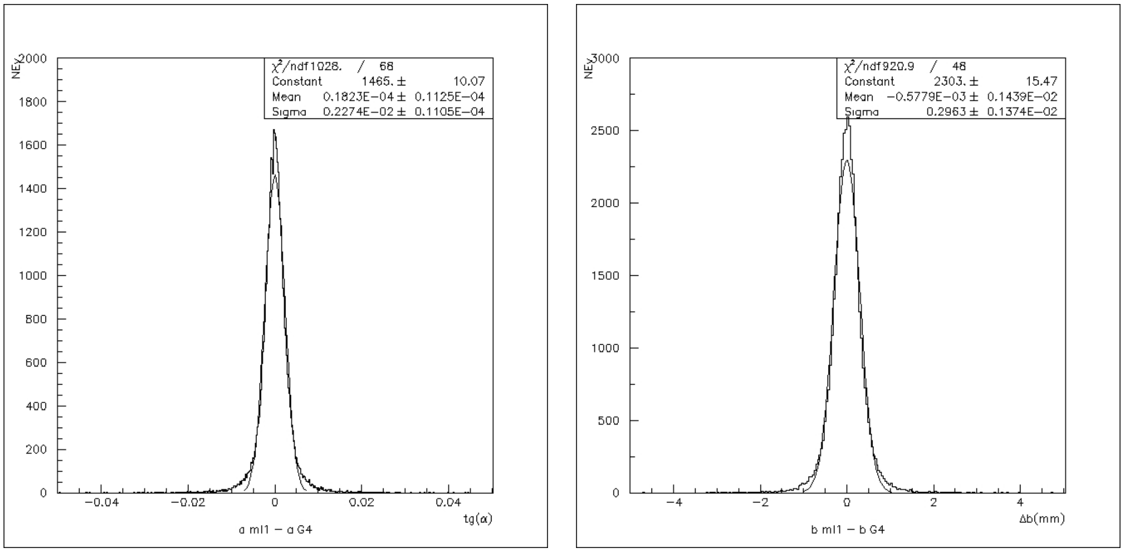

Figure 3.17: The effective resolution on a and b

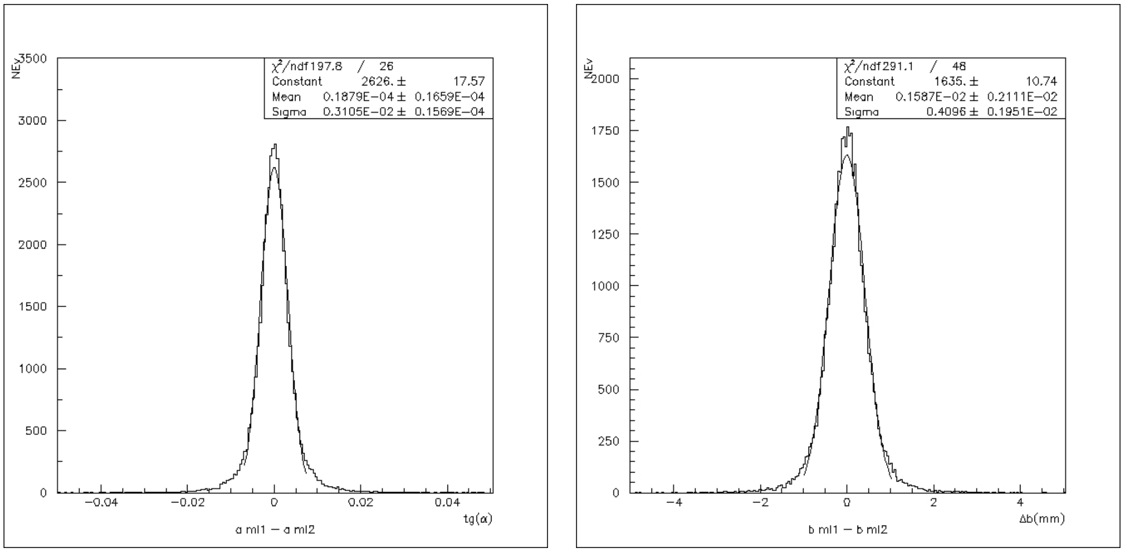

Figure 3.18: The difference between a and b as reconstructed in multilayer 1 and 2

3.6 Reconstruction of the chamber geometry

As we have seen from the previous section, the intrinsic accuracy on a and b (having placed the origin of the y axis in the medium plane of the chamber) are $\sim$2 mrad and $\sim$ 300 μm respectively. With a statistics of 100 k good tracks in the two extreme sub towers of the cosmic trigger we can therefore measure Δa with $\sim$ 10 μrad accuracy, $\Delta \mathrm{z}_0$ with 1.0 μm and $\Delta \mathrm{y}_0$ with a factor 10-20 worse, depending on the stereo angle. From simple geometrical considerations Δb , the difference of the track intercept in the middle plane between the two multilayers as reconstructed in multilayer 1 and multilayer 2, can be written as:

$$\Delta b \simeq \Delta y_0 \cdot a + (L \cdot \Delta\alpha + \Delta z_0) = m \cdot a + q \tag{3.1}$$

where L is the distance between the center of the multilayer and the central plane, 137 mm for a BIL chamber, a is the track angular coefficient, $\Delta\alpha \simeq a_{Multilayer1} - a_{Multilayer2}$, $\Delta \mathrm{y}_0$ is the error in the distance between the two multilayers, and $\Delta \mathrm{z}_0$ is the horizontal shift between the multilayers. Having measured $\Delta\alpha$ from the comparison of the track angular coefficient in the two multilayers, a linear fit to Δb versus a should allow a measurement of $\Delta \mathrm{y}_0$ and $\Delta \mathrm{z}_0$ with the required accuracy. From the data of Rome3 cosmic rays stand, the required statistics of $\sim$200 k triggers

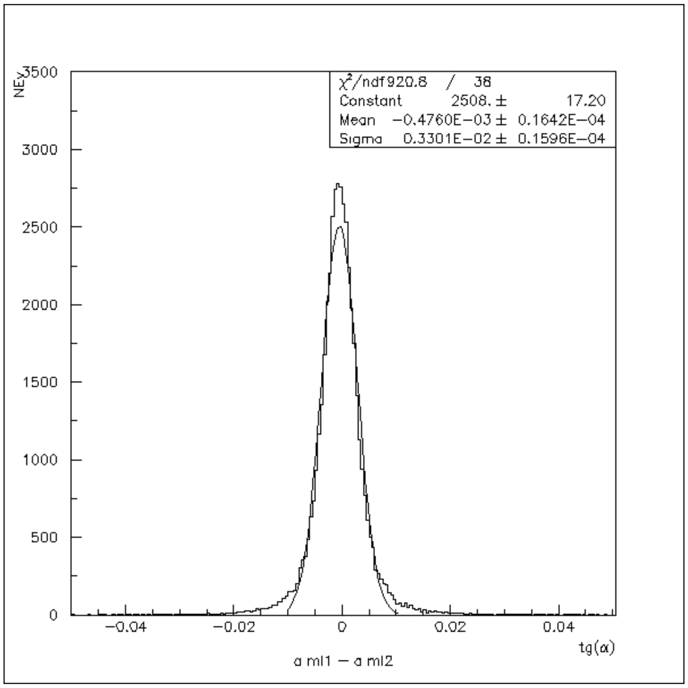

Figure 3.19: Δa between the angular coefficient of the track as reconstructed in multilayer 1 and 2 for a distorted chamber with $\Delta\alpha = 500$ μrad

(taking into account the overall efficiency for having a good track in both multilayers) within a sub tower can be easily collected in a 36 hours run with cosmics at sea level. In order to verify the accuracy that can be reached we have generated a sample of ~200 k triggers in the same conditions of section 3.5 but introducing a distorted geometry in the chamber description: $\Delta\alpha = 500\ \mu$rad, $\Delta y_0 = 700\ \mu$m, $\Delta z_0 = 100\ \mu$m. Following the same procedure as in section 3.5 and using the autocalibration to get the t-r relation, we have reconstructed in the first sub tower ~ 100 k tracks in both multilayers independently. The $\Delta\alpha$ distribution is shown in figure 3.19; the gaussian fit gives $\Delta\alpha = 476\ \mu$rad with an error on the mean of 10 μrad. The Δb versus a plot is presented in figure 3.20; the linear behavior is clearly visible. The fit to Δb versus a data gives: $\Delta y_0 = 704 \pm 19\ \mu$m and $\Delta z_0 = 102 \pm 3\ \mu$m , in good agreement with the distortions introduced in the simulation. As a cross check, the same plot on the high-energy muons and with undistorted chamber geometry is shown in figure 3.21. As expected $\Delta y_0 = 26 \pm 19\ \mu$m and $\Delta z_0 = 2 \pm 2\ \mu$m, well compatible with 0.

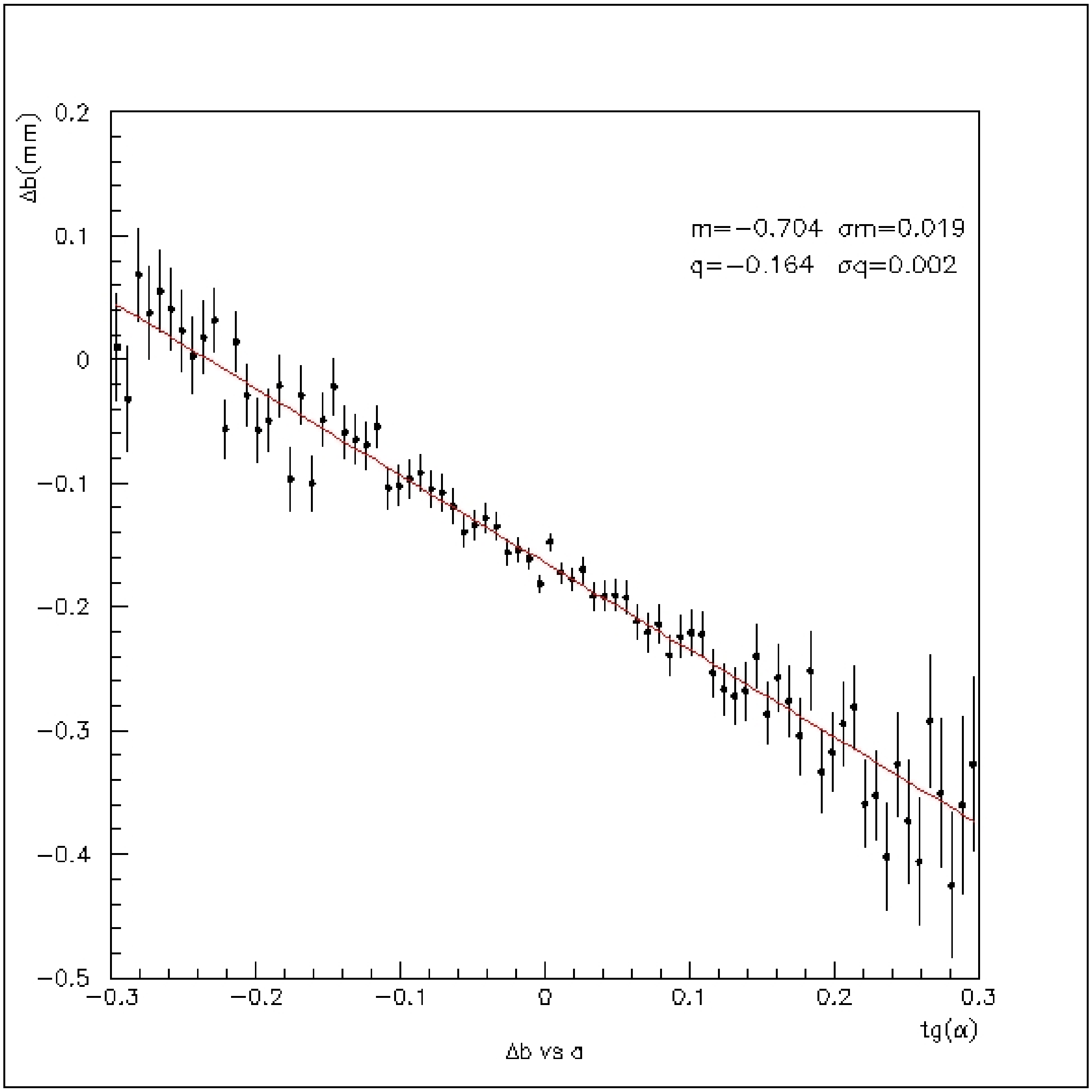

Figure 3.20: Δb between the impact point on the chamber middle plane of the same track reconstructed in the two multilayers versus the track angular coefficient for a chamber with distorted geometry

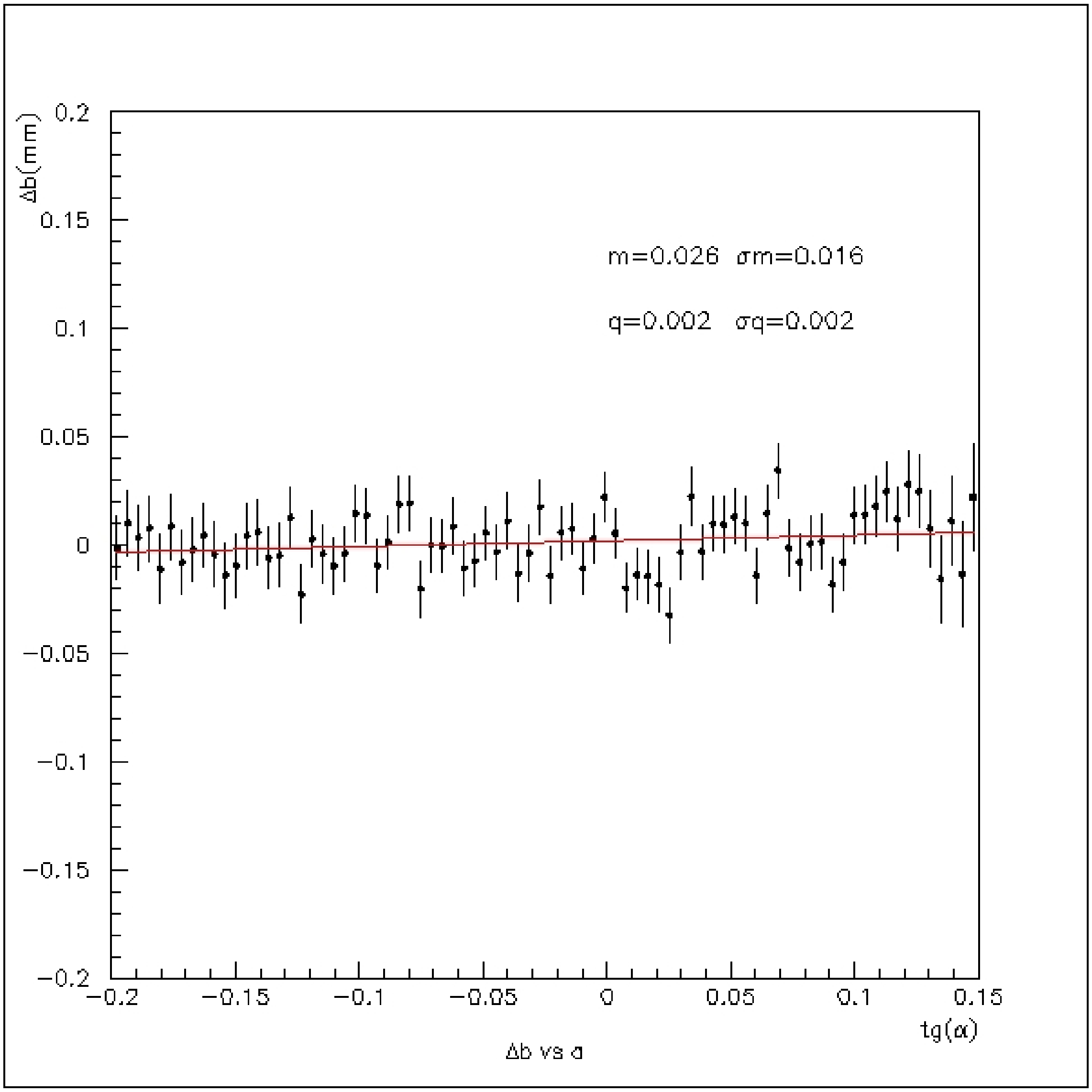

Figure 3.21: Δb between the impact point on the chamber middle plane of the same track reconstructed in the two multilayers versus the track angular coefficient for a chamber with undistorted geometry

3.7 Conclusions

In this chapter we have presented the expected performance of an MDT chamber in a cosmic rays stand; in particular we have shown that, with a relatively modest amount of data taking we can measure, with an accuracy comparable to the one of the X-ray tomograph device, the main geometrical deviations of a chamber, respect to the nominal site parameters. This result can be validated analyzing the cosmic data collected with chambers that has been measured at the X-ray tomograph facility and this type of analysis should be extended to all the MDT chambers in order to improve the overall Atlas muon spectrometer performance.

Chapter 4

The MDT Ageing Test

In this chapter we described the motivations and the setup of the MDT ageing tests. During a first phase, preliminary studies were performed in order to choose the experimental setup and to understand the sensitivity in terms of gain loss. This first part of the test was carried out in a storage area at CERN called BB5. The second and main part of the test took place at the CERN Gamma Irradiation Facility (GIF) were a chamber was irradiated from January 2004 to May 2004; during this period weekly data takings were performed: the gain has been monitored, as a function of the integrated charge, at different positions along the tubes.

4.1 Ageing of the MDT

Ageing effects on MDT are crucial since it is practically impossible to replace a muon chamber in the Atlas spectrometer in case of failure. Several different manifestations of “ageing effects” exists: typically there may be loss of gain, reduction of gain uniformity, decrease of energy resolution or efficiency, excessive dark currents, formation of sparks, current discharges or even a complete detector breakdown. These deleterious effects can all be caused by coating or other degradation of the cathode and the anode wire surface [29].

These effects are related to the absorbed radiation and are not reversible with a simple gas exchange. It is possible to group the undesirable effects into two categories: electrical breakdown and loss of gain. Deposits on the cathode like a thin insulating layer can cause self-sustained discharges or dark currents (“Malter effect”) but they don’t have a direct relationship with gain drops, while deposits on the anode have large influence on the gas gain. The increase in diameter of the anode wire will result in lower surface field, hence lower gain, even for a conductive coating. As an example, a 5 μm thick coating on a 50 μm diameter anode wire can cause large reduction in the avalanche gain, up to $\sim$ 80%. This coating is presumably deposited non uniformly, since gain variations are usually observed along the wire length. The most common assumption to explain the formation of these sparks or whiskers is that their formation is a polymerization process of the gas molecules between themselves or with contaminants [41]. Some of the possible sources of contamination are:

- Outgassing products: glues and plastic materials can dissipate plasticizer or other chemicals. The impact on the lifetime of the detector, however, is very small respect to other kind of contaminations;
- Impurities from gas leaks: loss of gas cause the contamination of the gas in the detector with air, which contains oxygen. The oxygen is an electronegative gas which has the ability to capture electrons, causing pulse height reduction: the quantity in the gas should stay below 100 ppm to avoid this effect.
- Modifications of materials under irradiation: some materials are stable in normal conditions but are instable and can be damaged when they are exposed to ionizing radiation;
- Cleaning procedure: different kinds of sealant, oil, grease and lubrificant are used during the production and assembly phase. They have to be completely removed from the detector to prevent uncontrolled contaminations, so the cleaning procedure is one of the crucial point to avoid improper cleaning;

When radiation background breaks covalent bond of contaminant molecules, a radical molecule is formed [37]. This molecule does not have electrical charge, but typically has a large dipole momentum, because it is frequently distorted. Because of the high electric field near the anode, these radical molecules are attracted to the anode wire surface. They are chemically very active and they can either recombine back to original molecules or form new molecular species.

One of the most important variable to control the formation of deposits on the anode wire is the gas flow rate. The rate of polymerization is low both for very low and very high flow rate. At very low flow rate there is usually not enough of the primary polymerization material (the contaminant), and at very high flow rate the charged polymers, depending on their weight, are swept away before they can reach the anode. Many products of oxygen and hydrocarbon radicals can be thus removed by a high gas flow. This is not so much the case with the silicon species because they are heavier. In this sense, the silicon contamination is a serious problem.

Many people reported ageing problems with silicon based wire deposits [42, 31, 37, 8, 29]. Silicon can polymerize both with oxygen and with carbon forming macromolecules like $(SiO_2)_n$. One of the possible source of Si atoms in the drift tubes is silicone, which is used as sealant, as lubrificant and also in some kind of o-rings. All the materials used in the MDT were carefully chosen and tested to prevent ageing effects. However, an empirical test with an Atlas-like full gas system is needed. One of the main goal of the ageing test subject of these chapter is the test of a very similar system of the gas circulation system foreseen for Atlas.

4.2 The Gamma Irradiation Facility

The Gamma Irradiation Facility (GIF) [27] is a test area in which large area high-energy particle detectors are exposed to an adjustable high background flux of photons, simulating the background conditions that these detectors will suffer in their operating environment at the Large Hadron Collider at CERN.

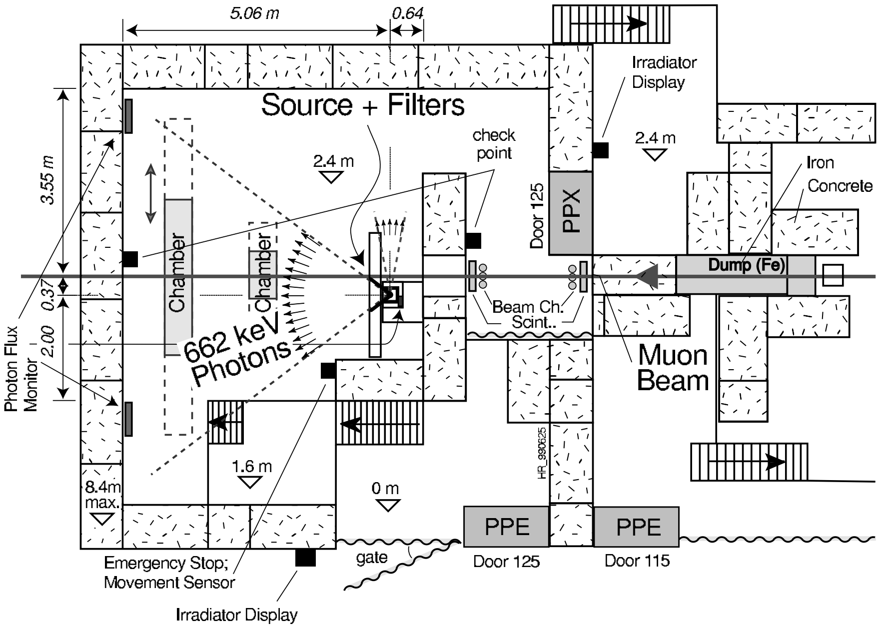

Figure 4.1: Layout of the test beam zone called X5/GIF at CERN. Photons from the radioactive source flood the detectors, producing a sustained high rate of random hits over the whole area. Calibration with tracks is done with a narrow beam of high energy muons.

The GIF is situated in the SPS West Area at the downstream end of the X5 test beam. A schematic layout of the GIF zone is shown in figure 4.1. The photons are produced by a strong radioactive source, the irradiator, housed in a rectangular container, 400 mm wide and 900 mm high. The active element is a radioactive ^{137}Cs source with a half-life of 30 years, the strength of which was measured on March 1997 to be 740 GBq (implying e.g. 630 GBq in March 2004), which emits a 662 keV photon in 85% of the decays. The principal collimator hole provides a pyramidal aperture of $74^o \cdot 74^o$ solid angle. This provides a photon flux in the pyramidal volume shown in figure 4.1. A pneumatic system raises the source to

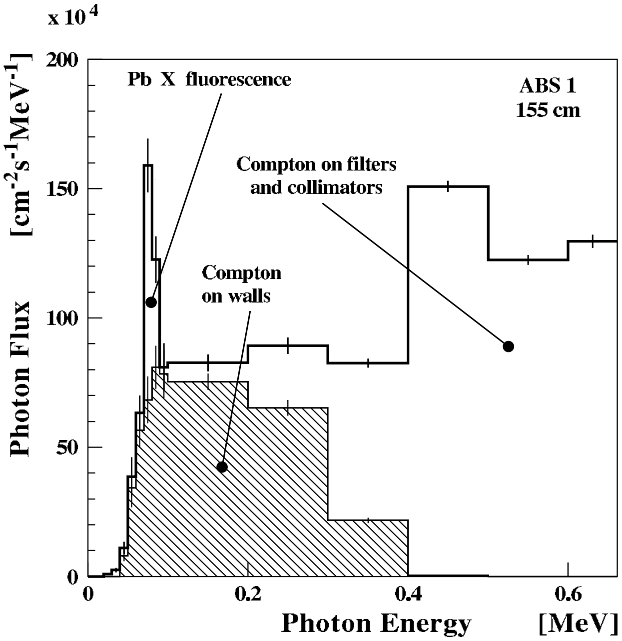

Figure 4.2: Simulated spectrum of the scattered photons at 155 cm from the source on the axis of the irradiation field and for absorption factor “ABS 1”. The three main contributions are indicated: two are from filters and collimators (white area), the other from walls and floor (dashed area). The total flux of scattered photons amounts to $6.4 \cdot 10^5$ cm^{-2}s^{-1}, while the flux of direct photons (at 662 keV, not shown) is $8.0 \cdot 10^5$ cm^{-2}s^{-1}

the irradiation position, or lowers it to the shielded position. In case of pressure drop, the source falls naturally, by its own weight, into its protection container. The pointlike radiation source delivers a flux of photons of fixed rate, which is uniform over a spherical surface. In contrast to this, for the systematic test of flat large area detectors the rate should be uniform over a plane and should be adjustable; some detectors with limited rate capability may even need a safe protection against too high rates. These three features are all implemented at GIF, with the help of specially shaped lead filters. The first filter has its shape calculated to transform the uniform rate on a spherical surface into a almost uniform rate on a planar surface. Its largest absorption factor is 2, at the center. This angular correction filter is always present. The other filters have thus only to ensure an absorption factor which is independent of the direction of the incident photon. A set of movable filters is installed in front of the source. It consists of three planes of two filters each. By remote control they can be moved laterally to place no filter or the desired filter of each plane in front of the source. The absorption factors of the filters are 100, 50, 1 for the plane closest to the source, 20, 10, 1 for the second plane, and 5, 2, 1 for the third plane, respectively. This gives possible attenuation factors over 4 orders of magnitude. The presence of massive objects like filters, walls, floor, equipment, is at the origin of scattered photons in addition to the original monochromatic "direct" photons, figure 4.2. The scattered photons make simple precise predictions very difficult, since they will depend on details of the actual geometry and on a possible spectral dependence of the detector response.

4.3 Ageing tests 2001-2003

A final Atlas chamber of type BIS (Barrel Inner Small, described in 4.4) became available for ageing tests in 2001. The chamber was exposed over its full size to an intense photon flux at GIF between November 2001 and May 2003 [7]. The MDT performances were monitored in weekly reference runs using cosmic muons, recording for each tube the drift time measurements and, every third tube, recording the pulse height of the signal generated by the muon using a charge integrating ADC.

During reference runs the γ-source was retracted into its lead housing. A 4-layer 105·100 cm^2 scintillator hodoscope was used for trigger purpose; it also permitted to point the position of the cosmic rays in the direction of the MDT wires. One of the major goal of the study was to test a gas recirculation system similar to the one foreseen at Atlas. The gas system parameters were chosen such to reproduce the Atlas conditions as closely as possible; a bypass loop was included to run the gas compressor Argon Turbo Circulator, described in par. 2.2.8, at its nominal flow rate despite the BIS volume constitutes less than one permille of the total Atlas volume. One of the two multilayer of the BIS, from now referred as "multilayer 1", was connected to the gas recirculation system, while the second one ("multilayer 2") was operated in flushing mode for comparison.
Since the attenuation of 660 keV γ after the material of one multilayer ($\sim$2 mm of aluminium, argon is negligible) is very small as it can be inferred from figure 2.6, the dose absorbed from the two multilayer can be considered equal.

A typical pulse charge spectrum measured in a reference run is showed in figure 4.3. For each tube, thus each spectra, a Landau distribution was fitted to the data. The maximum of the Landau distribution, Q_{tube}, is proportional to the gain of the tube, and can be used to investigate possible gain drops. All data has been scaled to

20^oC according to the relation $Q_{20} = Q(T)[1+0.022\cdot(20^o-T)]$, which was established in test beam measurements performed in summer 2002. This relation is in agreement with the one which can be derived from the Diethorn formula 2.6: $\Delta G/G = 9.86 \cdot \Delta T/T$, which corresponds to a gas gain variation of 3.3% per temperature degree.

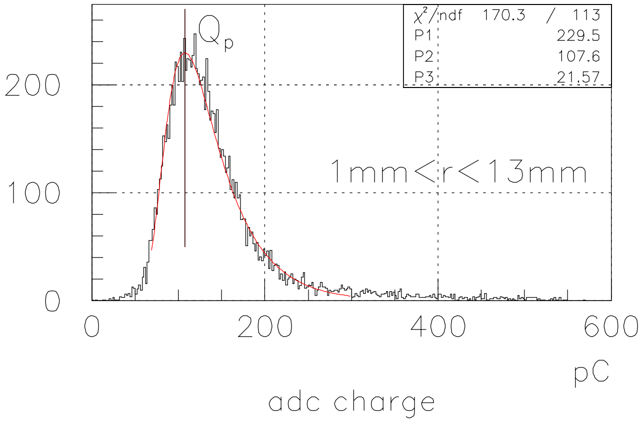

Figure 4.3: Pulse charge spectrum for cosmic muons; a Landau distribution is fitted to the data. The maximum is indicated as Q_p.

4.3.1 Results for “multilayer 2” operated in flushing mode

For tubes operating in flushing mode, no loss in pulse height was observed up to an accumulated charge of 240 mC/cm, equivalent to 4 years of LHC operations included the safety factor of 5. In figure 4.4 is plotted the pulse height $Q_{rel} = Q_{tube(i)}/Q_{ref.tube}$, where $Q_{ref.tube}$ were the tubes disconnected from the High Voltage during the irradiation, thus they did not accumulate charge. None of the 38 monitored tubes belonging to the vented multilayer showed any distortions in the ADC spectrum, that were similar to the one showed in 4.3.

4.3.2 Results for “multilayer 1” with gas recirculation

For the tubes operated in recirculation mode, ageing effects started to show up when 40 mC/cm of charge were accumulated on the wires. The first effect observed was a distortion of the pulse height spectra, which started to show a second peak at charge smaller than the one fitted with the Landau distribution (figure 4.5).

Further investigations were done during normal reference runs by reconstructing the cosmic muon track positions along the wire using the hodoscope informations. These studies showed a large loss of gain in the first 30 cm from the gas inlet,

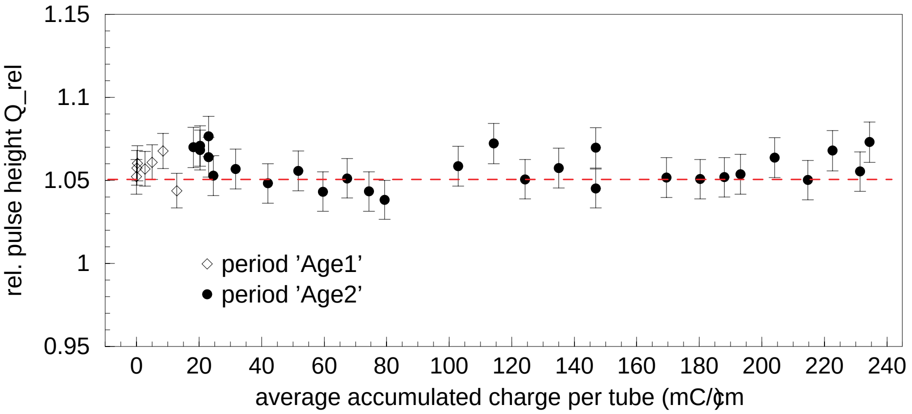

Figure 4.4: Relative pulse height Q_{rel} as a function of the integrated charge; the results are consistent with a line of zero slope, thus no evidence for ageing is present in the multilayer operated in flushing mode.

then the effect decreased until it was negligible after 50 cm, as it is shown in figure 4.6. These results were obtained after the irradiation period by moving a small radioactive source along the tubes.

All the 33 monitored tubes under high voltage during the irradiation showed drops of gain close to the gas inlet side, while the two reference tubes disconnected from high voltage during the irradiation kept constant their behaviour. After approximately 240 mC/cm the chamber irradiation was stopped, and several MDT were opened: the scanning electron microscope technique (SEM) revealed a growth of needle-like structures on the anode wire. They had a length of 5-7 μm close to the gas inlet side and decreased in size when moving further down the tube, in agreement with the pulse height behaviour. An energy dispersive X-ray (EDX) analysis indicated that these deposits were made of silicon and oxygen, while no carbon was detected. It was concluded that the observed ageing effects were due to a contaminant: a first attempt to find the pollutant directly in the gas by doing a gas chromotography was unsuccessful. Therefore, since the MDT operated in flushing mode did not show any ageing effects, a deep analysis of the gas system was performed, especially in the region of the recirculation loop.

It was found that three valves contained a silicone sealant. Further it was discovered that the specifications about the use of lubrificant, no lubrificant in all the gas system except for the silicon-free vacuum grease Apiezon in few well-defined locations, were not respected.

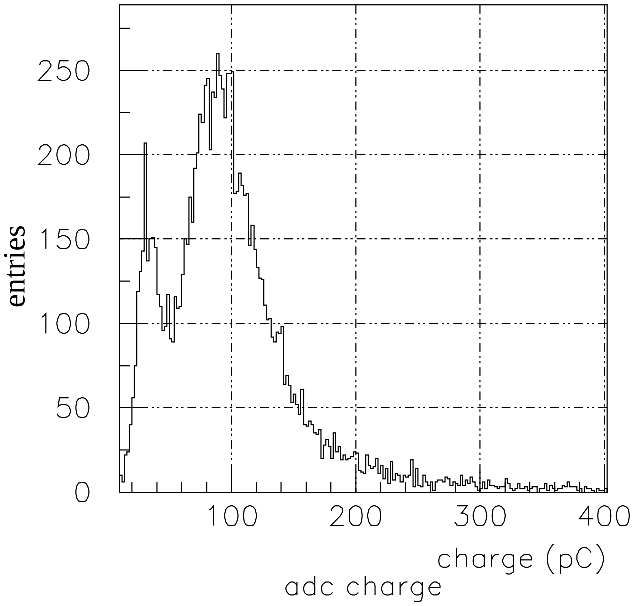

Figure 4.5: ADC spectrum for a tube operated with gas recirculation after an irradiation of 240mC/cm.

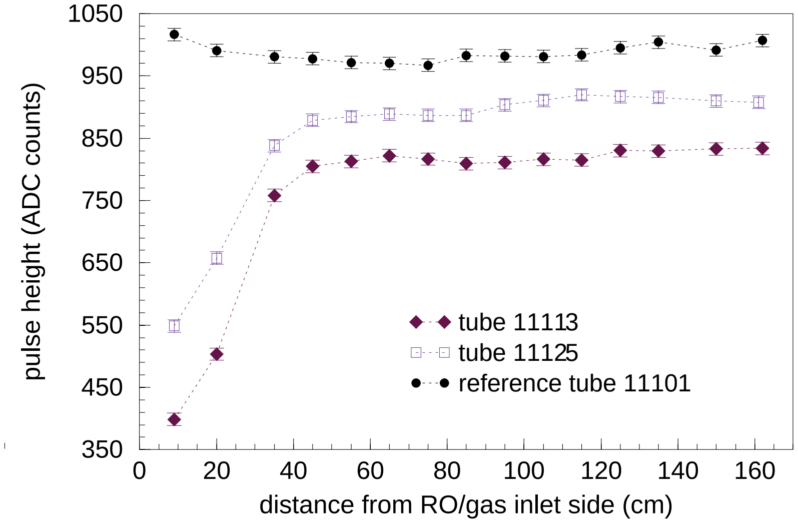

Figure 4.6: Pulse height versus position in the wire for two tubes operated in recirculation mode.

4.4 Mechanical setup: the BIS “Beatrice” and the bundles

In the 2004 ageing test an Atlas MDT chamber of type BIS (Barrel Inner Small), called “Beatrice” [22] [7], and two little test-chambers, referred to as “bundles”, were used. The BIS Beatrice is one of the first MDT produced following the final Atlas design and using the final Atlas components, except for the front-end readout electronics (described 4.6) and the Faraday cages.

Beatrice is built with 2 multilayers of 4 layers each. Each layer consists of 30 drift tubes 170 cm long, for a total of 240 tubes. The multilayers are separated by seven 6 mm thick aluminum strips. The volume of each multilayer is approximately 144 liters. The gas distribution system, fully parallel, has already been described in 2.2.7. The two bundles are constituted of 4 layers of 6 tubes each. The tubes are 280

Figure 4.7: The mechanical setup in the GIF area. The BIS is on the left, the two bundles on the right. In the middle it’s possible to distinguish the movable support of the two ^{241}Am sources.

cm long for a total volume of ~48 liters. The bundles have a serial gas distribution, which means that the 6 tubes of each layer are connected in series from the point of view of the gas: thus the gas outlet of the first tube goes into the gas inlet of the second one and so on. Instead, the four layers have a parallel gas connection.

The BIS and the bundles were mounted as shown in figure 4.7, with the tubes in vertical position, the readout side on the bottom and the high voltage side on the top. The BIS and one bundle were aligned and the other bundle was on the back of the first one. The GIF gamma source, not visible in the picture, is in front of the mechanical structure at a distance of ~150 cm.
The front-end electronics was mounted on the bottom-side of the chambers, with the high voltage distributor boards on the top.
One of the two bundles showed problem of self-sustained dark currents during the test performed in 2002 after the assembly. It was cured by exchanging for some days the anode voltage from positive to negative (the so called "reconditioning" procedure), and it was observed not to show any dark currents problem. To test the functionality of this bundle with reconditionated wires, a second one, that did not show any known problem, was mounted as comparison.
Since one multilayer of the BIS was damaged in a not repairable way at the end of the 2001-2003 ageing test briefly described in 4.3, only the other multilayer of the BIS, the one closer to the GIF source and visible in the figure 4.7, was equipped with the gas distribution and the front-end readout electronics. Only the bundle without reconditionated wires, the one closer to the GIF source, was readout in the weekly reference runs, while for the reconditionated bundle only the absorbed currents were monitored and compared to the currents absorbed from the other one.

4.4.1 Naming and conventions

The BIS tubes name follow this convention:
- the layer number increases from 1 to 4 according to the distance from the source, layer 1 being the closest;
- the tube identifier increase from 1 to 30, tube 1 being at the left side;
- similarly for the bundles, the layer (tube) number runs from 1 (1) to 4 (6) respectively.

The X-axis is directed parallel to the tube wires. Its origin corresponds to the bottom of the BIS tubes, where the gas inlet is situated, and increases with the height from the floor. The Y-axis is directed as the numbering of the tubes.

4.5 Gamma sources and step motors

Two ^{241}Am sources with an activity of 36.5 MBq each were used to monitor the behaviour of the MDT. The ^{241}Am emits α particles and γ. The α particles are not able to reach the chamber, thus are not interesting for our studies. The emitted γ interact with the tubes, depending on their energies: the ^{241}Am emits γ with 60 keV (36%), 35 keV ($\sim$15%) and 14 keV (42%). It was decided to use this γ source for different reasons:

- γ of 60, 35 and 14 keV interact mainly in photo-electric way, as already mentioned in 2.2.2. All the energy is released to a single electron that ionises atoms along its path. Its range is of few millimeters, so they generate a sharp signal which exhibits a clear peak in a pulse charge spectra.

- The energy of the emitted γ is in the requested range; for example, a ^{55}Fe radioactive source emits 6 keV γ which have a very small probability to cross more than one tube, and a ^{137}Cs source (660 keV γ) generates signals on the wire very similar to muons (figure 2.8) making difficult the measurement of the variation of the gas gain since the energy released in the tube is not constant (see 2.2.2).

- The intensity of these two sources is such that we have a counting rate of few kHz on the irradiated tubes, suitable to make a proper measurement on the pulse charge distribution in stable conditions.

The radioactive sources were mounted in a lead housing for safety reasons; when the lead housing is in unsecure position the photons irradiate a 30^o cone zone. To study the behaviour of the tubes along the wire, since the sources are positioned 10 cm far from the first layer of the tubes, a collimator was positioned in front of each source. These collimators were built such that on the x-axis only $\sim$3 cm of wire is irradiated on the fourth layer, which is $\sim$18 cm away from the source. On the y coordinate no collimation was done, thus $\sim$ 6 tubes on the fourth layer were irradiated simultaneously. The two sources are mounted on a mechanical support moved by two step motors along the X and the Y axis, to illuminate different portions of the wires and different tubes. The software control of the motors, included in the data acquisition software in a pc outside of the X5 zone, was done via serial port and was able to move the sources between different positions (in few seconds) avoiding radiological risk for the people on shift.

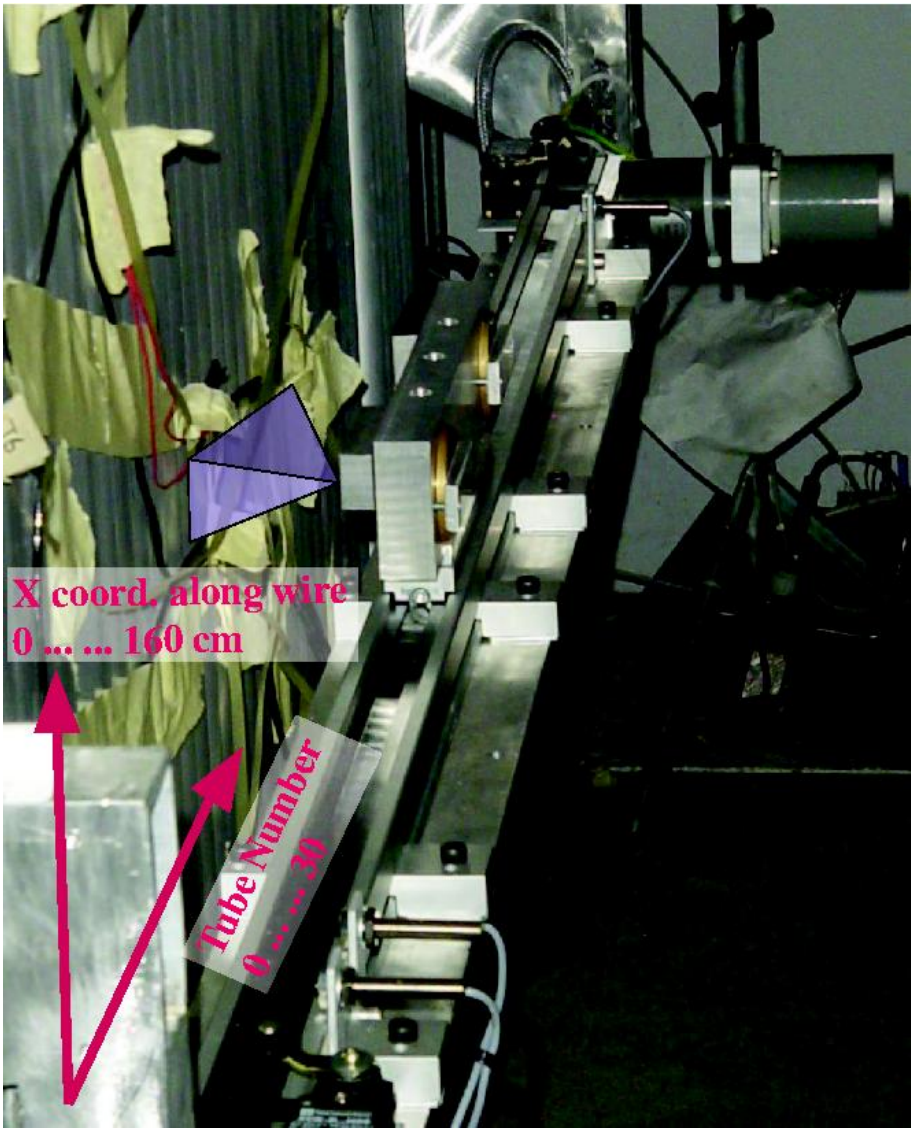

Figure 4.8: A zoomed view of the movable support and of the horizontal step motor used to move right-left the two γ sources (in the center of the picture). The violet pyramid would represent the γ source collimator, while the red arrows indicates the X-axis, the origin corresponds to the gas inlet side of the tube, 160 cm to the gas outlet, and the Y-axis, corresponding to the tube numbering that increase from left to right.

4.6 Electronic choice: unipolar versus bipolar shaping. Preliminary tests

The MDT front-end electronics was reviewed many times since the first proposal scheme of the TDR. Especially the question of unipolar versus bipolar shaping for the transfer function of the preamplifier-filter system was reconsidered. The transfer function for bipolar shaping, both in the complex variable s and in time t, is:

$$g(s) = \frac{n! s\tau}{(1+s\tau)^{n+2}} \longrightarrow f(t) = (1 - \frac{t/\tau}{n+1})(t/\tau)^n e^{-t/\tau} \quad t_p = \tau \cdot (n + 1 - \sqrt{n+1}) \tag{4.1}$$

where n is the order of the transfer function, in this case 2, τ is the time constant and t_p is the peaking time of the function, 12.5 ns. Since the delta response integrates to zero, which means that every signal convoluted with this transfer function integrates to zero, it is not necessary to add any other filters. On the contrary, for the unipolar shaping, the transfer function is:

$$g(s) = \frac{n!}{(1+s\tau)^{n+1}} \longrightarrow f(t) = (t/\tau)^n e^{-t/\tau} \quad t_p = \tau \cdot n \tag{4.2}$$

together with two pole-zero filters, needed to cancel the long signal tail:

$$g(s) = \frac{s + 1/\tau_1}{s + 1/\tau_2} \longrightarrow f(t) = (1/\tau_1 - 1/\tau_2) e^{-t/\tau} + \delta(t) \tag{4.3}$$

Also for the unipolar transfer function n=2 and t_p=12.5 ns. The transfer functions for both shaping schemes can be seen in figure 4.9. As final readout electronics the bipolar shaping was chosen mainly because the unipolar shaping requires an active baseline restoration circuit to avoid baseline fluctuations due to high rates. In order to have a proper measurement of gain loss with the final mezzanine, since it is not possible to integrate the full length of the signal due to the bipolar shaping applied on it, we tried to use the information stored in the Wilkinson ADC, that integrates the signal in a programmable gate from 8 to 45 ns. We started using the standard electronics parameters configuration, gate 15 ns, rundown current 4.5 μA, threshold -44 mV, then we simulated the variation of gain by decreasing the high voltage. For safety reasons we used one small ^{109}Cd γ source (85% 22keV, $\sim$ 60 kBq) to illuminate one tube, then we readout the Wilkinson ADC measurements from the CSM (as explained in 2.2.5). The Wilkinson ADC spectra that we obtained are showed in figure 4.10.

The “shoulder” on the right of the spectra is probably due to a saturation in the capacitor used to store the integrated charge. This saturation didn’t appear in the measurements done with muons for the reason we explained in 2.2.2: γ from ^{109}Cd,

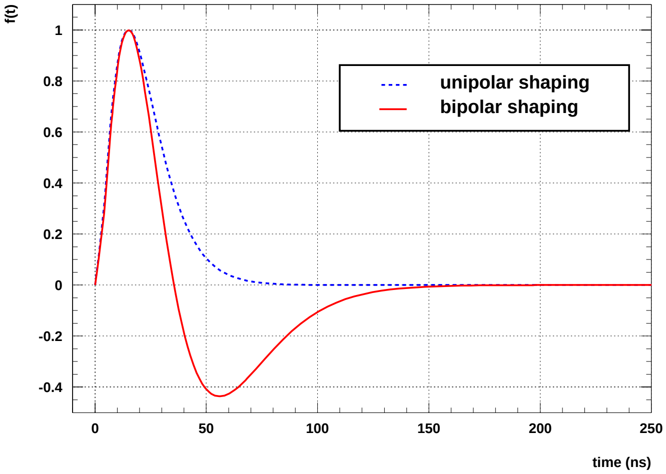

Figure 4.9: Frontend delta response for unipolar (blue dashed line) and bipolar (red line) shaping. The unipolar response is at the preamp output, without the filter stages.

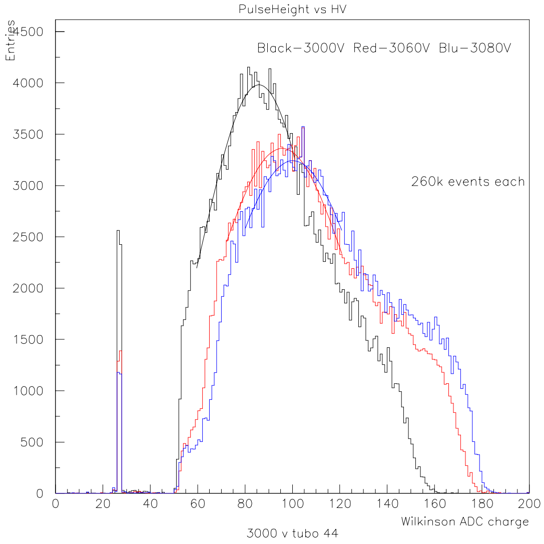

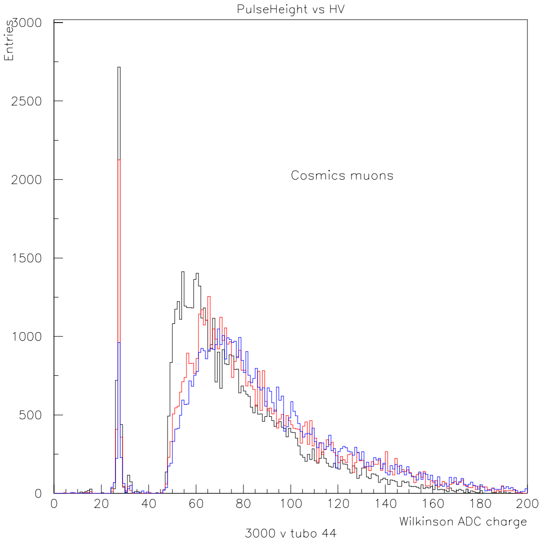

Figure 4.10: Wilkinson ADC charge spectra at different high voltages.

Figure 4.11: Wilkinson ADC spectra for cosmic muons at different high voltages.

inside MDT, released all their energy in shorter signal respect to muons, thus the charge contained in the first 15 ns for γ is more than double than for muons. As cross-check, we did the same test with cosmics muons. The Wilkinson ADC spectra that we obtained for cosmic muons are showed in figure 4.11. To understand the sensitivity on this measurement of gain loss, we compared, at different high voltages, the variation of the peak position to the expected variation of gain as reported in [34]. The results are shown in figure 4.12. Between 3080 V and 3060 V the pulse height reduction measured was ~5%, while the gas gain reduction following reference [34] is about 25%. Between 3060 V and 3000 V the pulse height reduction was ~10% and the gas gain reduction is ~30%. We did other tests changing the Wilkinson ADC parameters to improve the accuracy of the measurement with similar results. These preliminary tests showed that, in order to discriminate gain differences of about 5-10%, it is not enough integrate only the rising edge (15-20 ns) of the signal.

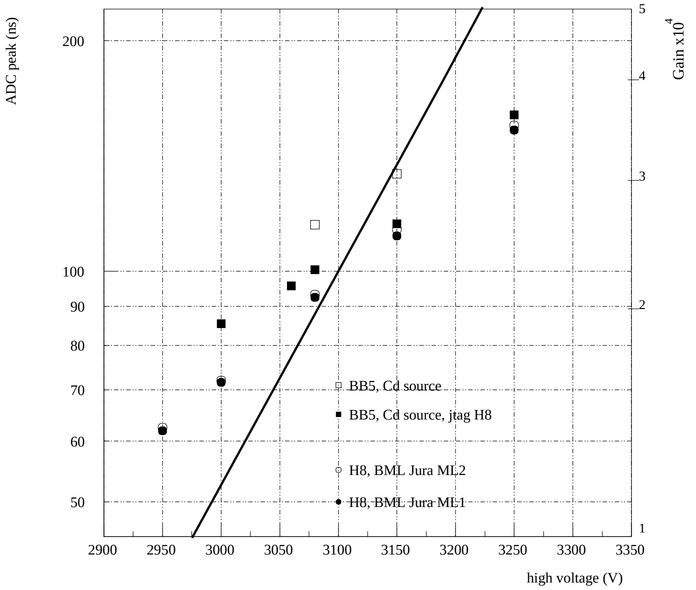

Figure 4.12: Wilkinson ADC pulse height as a function of the high voltage. The two types of squares indicate the measurements of pulse height with a ^{109}Cd γ source with two different gates. The line is the Aleksa-Riegler measurement [34] of gas gain variation as a function of the high voltage. The circles represent H8 data of the summer 2003 for two different multilayer, shown here as further comparison.

Since the “old” mezzanine, the one with the unipolar transfer function, has some electronics-debugging output pins from which is possible to pick up the analog signal after the amplification and the shaping, we decided to use this readout electronics. This allowed us to integrate the full analog signal, thus having a good accuracy on gain drop measurements.

4.7 Gas system and slow control

To simulate the final Atlas gas system (2.2.8), a prototype system which uses the final Atlas gas circulator ATC has been built. This off-chamber gas system is similar to the one used in the previous ageing test mentioned in 4.3. A scheme of the setup, as shown in the slow control program, is presented in figure 4.13. One of the difficulties in building an appropriate down-scaled test setup lies in the much smaller gas flow that is needed for a setup approximately one thousand times smaller than the final Atlas gas system: the ATC turbine, in fact, cannot deliver a flow only 10^{-3} of the nominal one of 100 Nm^3/h.

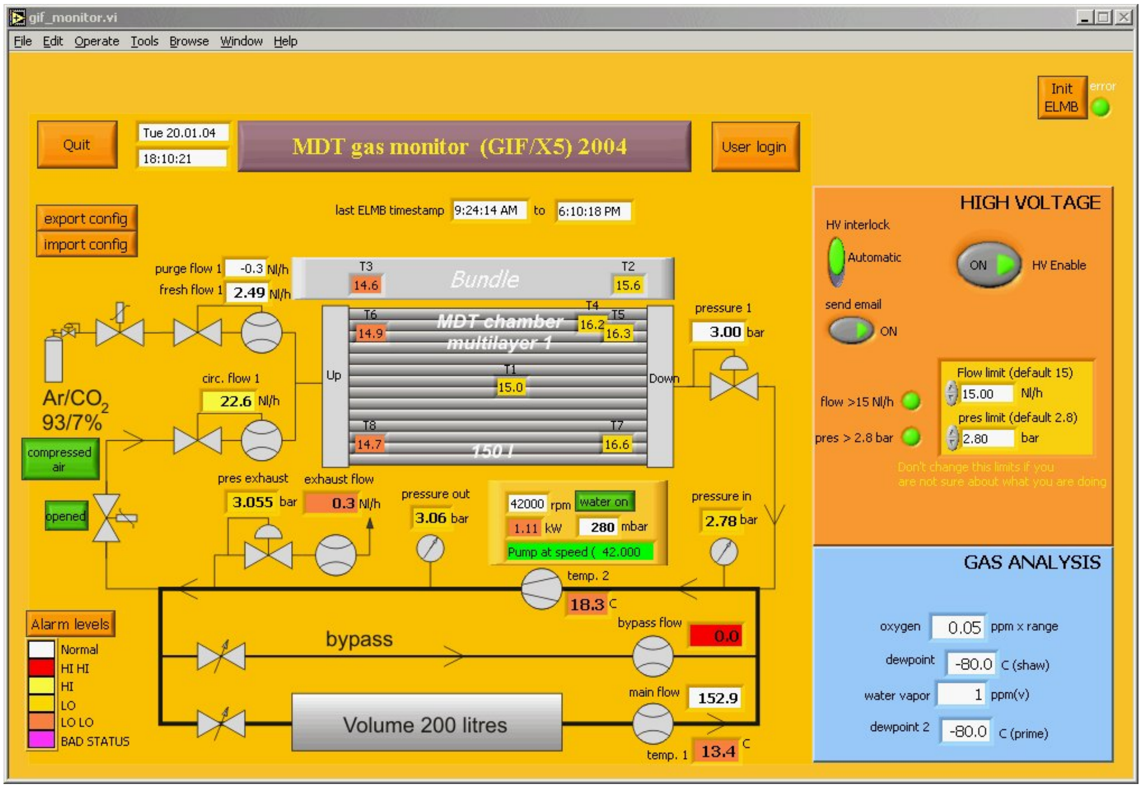

Tue 20.01.04
18:10:21
MDT gas monitor (GIF/X5) 2004
last ELMB timestamp 9:24:14 AM to 6:10:18 PM
purge flow 1 -0.3 Nl/h
fresh flow 1 2.49 Nl/h
T3 14.6
T2 15.6
T6 14.9
T4 16.2
T5 16.3
T1 15.0
T8 14.7
T7 16.6
pressure 1 3.00 bar
circ. flow 1 22.6 Nl/h
pres exhaust 3.055 bar
exhaust flow 0.3 Nl/h
pressure out 3.06 bar
42000 rpm
water on
1.11 kW
280 mbar
Pump at speed (42.000
pressure in 2.78 bar
temp. 2 18.3 C
bypass flow 0.0
main flow 152.9
temp. 1 13.4 C
Flow limit (default 15) 15.00 Nl/h
pres limit (default 2.8) 2.80 bar
Don't change this limits if you are not sure about what you are doing
oxygen 0.05 ppm x range
dewpoint -80.0 C (shaw)
water vapor 1 ppm(v)
dewpoint 2 -80.0 C (prime)

Figure 4.13: A picture of the slow control panel. In the middle the scheme of the circulation gas system and the position of the temperature sensors are drawn. The two bundles are connected in a series, which then is connected in parallel with the BIS. On the right the high voltage interlock, related to the gas flow and pressure.

In this gas system this problem was solved by including a large bypass loop into the gas re-circulation loop: in this way the turbine pumped 100 Nm^3/h of gas, but only a small fraction of this flow was sent to the BIS and the bundles. A buffer volume of 200 liters was found suitable to act as a bypass for the major part of the circulating gas.

The standard Atlas gas mixture Ar-CO_2 93:7 was provided in premix bottles grouped in batteries and stored outside the GIF building. The two racks containing all the gas system are outside the GIF area. The scheme of the gas distribution is given in figure 4.14. Three gas pipes are the connection between the gas system and the chambers: two lines are used to supply the gas to the BIS and to the bundles, while the other line is the exhaust. The gas circulation is fully parallel in the BIS, as explained in 2.2.7, and serial in each layer of the bundles, as explained in 4.4. The gas inlets of the BIS and of the bundles series are splitted in parallel from the gas racks: the gas flow is divided such that the gas exchanges per day are the same for the BIS and the bundles. The circulation operating conditions were similar to the Atlas nominal ones: the 10% of gas was replaced by fresh gas in each cycle, the other 90% of the gas was re-circulated. The gas flow through the chambers was 2 volumes per day for the first period of the test and then was increased to 4 volumes per day.

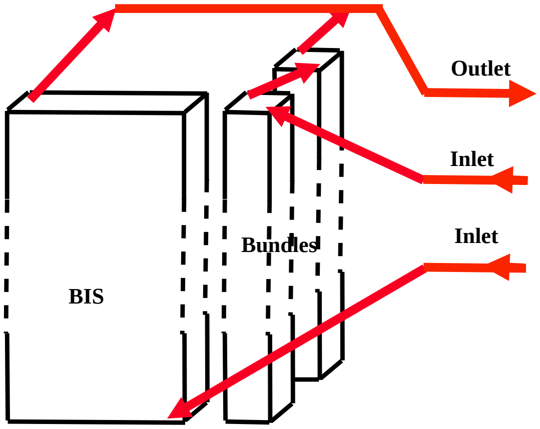

Figure 4.14: A schematic draw of the gas distribution.

The high voltage was provided to the chambers via a CAEN A333N (4 Channel 4 kV / 2 mA) high voltage board mounted in a CAEN SY527 power supply. To perform the monitor of the high voltage parameters of the CAEN SY527, it was linked to a VME system via a CAEN A128HS module. Since we would monitor the integrated charge by each chamber, we used three different channel for the BIS and for the two bundles. Six tubes for each layer, the BIS tubes from 25 to 30 in the naming convention explained in 4.4.1, were disconnected from the high voltage and used as reference tubes, to be sure that the effects we were looking for were due to irradiation and not to other causes. These tubes were reconnected to the high voltage only during the weekly reference runs. Particular attention was given not to have “ground loops” due to different grounds between the high voltage power supply positioned outside the GIF area and the chambers inside the area. The voltage was set to 3400 V (MDT still in proportional regime) during the irradiation period to accelerate the ageing process, and to 3080 V during the reference runs.

Temperature sensors were mounted on the chambers in order to be able to apply temperature correction in the data analysis. The slow control was divided in two parts done in two different pcs: the gas and temperatures monitoring and the high voltage monitoring.

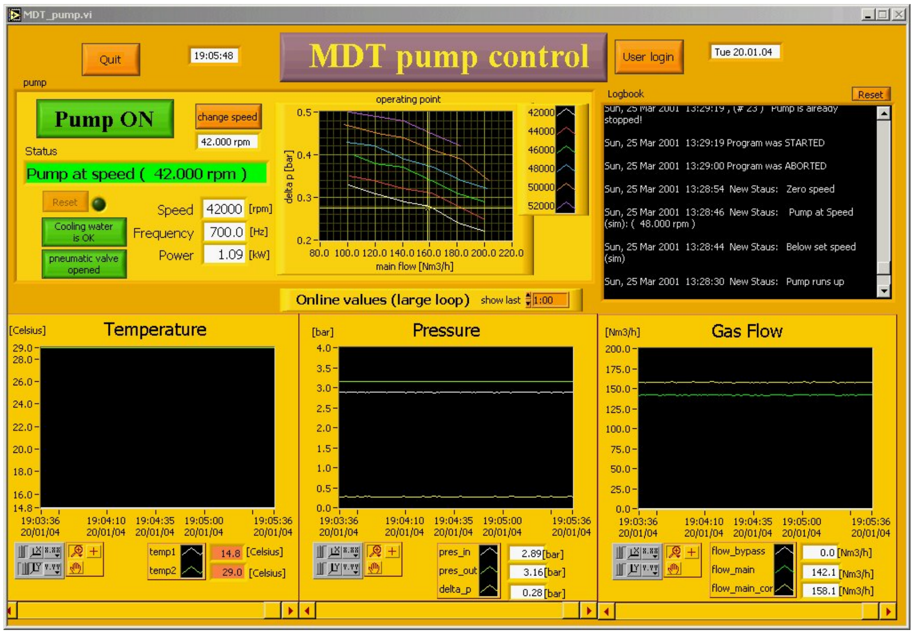

19:05:48

Tue 20.01.04

42.000 rpm

Status: Pump at speed (42.000 rpm)

Speed 42000 [rpm]
Frequency 700.0 [Hz]
Power 1.09 [kW]

show last 1:00

```
Sun, 25 Mar 2001  13:29:19 , (# 23 )  Pump is already
stopped!

Sun, 25 Mar 2001  13:29:19 Program was STARTED

Sun, 25 Mar 2001  13:29:00 Program was ABORTED

Sun, 25 Mar 2001  13:28:54  New Staus:   Zero speed

Sun, 25 Mar 2001  13:28:46  New Staus:    Pump at Speed
(sim): (  48.000 rpm )

Sun, 25 Mar 2001  13:28:44  New Staus:   Below set speed
(sim)

Sun, 25 Mar 2001  13:28:30  New Staus:   Pump runs up
```

temp1 14.8 [Celsius]
temp2 29.0 [Celsius]

pres_in 2.89 [bar]
pres_out 3.16 [bar]
delta_p 0.28 [bar]

flow_bypass 0.0 [Nm3/h]
flow_main 142.1 [Nm3/h]
flow_main_cor 158.1 [Nm3/h]

Figure 4.15: The ATC pump control and monitor panel

The “gas pc” monitored:

- flows and pressures in different points of the circulation system (figure 4.13);
- ATC turbine speed and frequency (picture shown in figure 4.15);
- temperatures.

The “DAQ pc” monitored the voltage and the current of the three used channels and the status of the step motors. The slow control informations, acquired every minute, were automatically transferred on a server each ten minutes. A script running on the server updated a web page which allowed to monitor the integrated charge of the BIS and of the bundles and the status of the whole system. In case of problems, it was also possible to be advised by automatic SMS in which the kind of failure or the value out of a given range was reported. The high voltage was also hardware interlocked by the gas slow control pc in case of flow or pressure under standard values.

4.8 Trigger and data acquisition

As explained in 4.6, we used 5 “old” mezzanine (6×4 tubes) for the BIS and 1 for the bundle. Since in this way it is possible to have the analog signal of 1 out of 3 tubes, we have 48 analog outputs from the 120 + 24 tubes of the system BIS-bundle. The number of the analog outputs depends on the design of the mezzanine: in our case we red out the tubes 3 and 4 of each mezzanine. Since the time available for the weekly reference runs was only about 6 hours, it was impossible to move each time the mezzanines in order to read out all the tubes. These signals were carried out of the X5 zone with 80 m long BNC cables and fed into custom-made splitters. One of the two output of the splitter is delayed of 75 ns and goes in a CAEN V792 integrating charge ADC (32 ch., 12bit, 400pC max charge), the other is sent to a discriminator. The discriminators outputs are sent to coincidence units and then to a 500 ns gate generator which drives the ADC. The scheme is shown in figure 4.16. Since the number of readout channels was 48, we used two ADCs. We used also two different gate generators, to minimize the number of empty events stored in the ADCs. The two ADCs are housed in a VME interfaced to the DAQ pc via a National Instruments VXI-MXI bus. Using the LabWindows-C programming language, we developed a program that we called MicroDAQ. This software is able to acquire data, drive the step motors and monitor the high voltage. A screenshot of the MicroDAQ panel is shown in figure 4.17. After the initialization (the “Init” button) of the VXI for the VME and of the motors driver, it is possible to “Start Monitor” of the high voltage, to “Start Run” to acquire data, or to “Move” the motors. The names of the monitor and data file are automatically generated: they are based on the day, the time, the motors position. It is possible to insert a comment string in case of

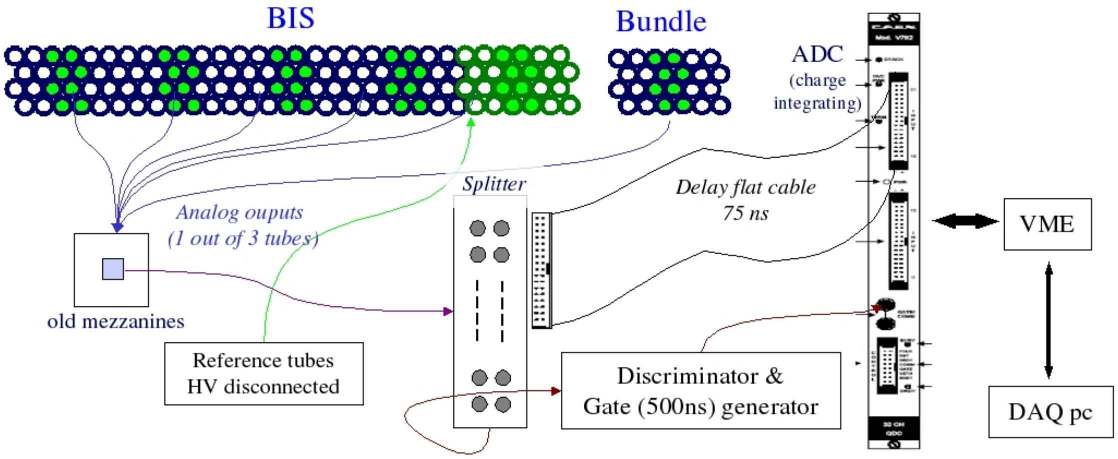

Figure 4.16: The trigger scheme

X-pos 10		**X-pos 20**		**X-pos 30**	**X-pos 40**
Mezzanine1	Mezzanine2	Mezzanine3	Mezzanine4	Mezzanine5	Mezzanine6
Lay. 1,2,3,4 Tubes 03,04 BIS	Lay. 1,2,3,4 Tubes 09,10 BIS	Lay. 1,2,3,4 Tubes 15,16 BIS	Lay. 1,2,3,4 Tubes 21,22 BIS	Lay. 1,2,3,4 Tubes 27,28 BIS	Lay. 1,2,3,4 Tubes 3,4 bundle

Y-pos (for each X-pos)
0, 2, 5, 8, 10, 12, 15, 25, 35, 55, 85, 120, 155, 158, 161
cm from gas inlet

Table 4.1: The ^{241}Am sources positions during the reference runs.

particular runs. The motors, apart when there are reference runs, must be in the garage position. The garage position is such that the sources are hidden by a lead protection: in this way the radiation level in the area is lower than the safety limits.

The high voltage data, set and monitor voltage and current for each channel, were recorded every minute, apart from the weekly reference runs. During these periods, since the GIF source was retracted in its lead housing, the chambers weren't exposed to irradiation and their currents were below 5μA instead of 800μA with the GIF open.

It was possible to move the two step motors to different positions. Table 4.1 shows the positions studied systematically during the data taking.

Since the distance between two couple of "readable out" tubes on the BIS is six times a tube diameter, the distance between the center of the two source collimators mounted on the mechanical support is 18 cm. The X-pos 10 and 20 illuminate two mezzanines together, while the X-pos 30 and 40 only one each. This is due to the fact that the distance between the last mezzanine of the BIS and the mezzanine of the bundle is $\sim$10 cm more than the distance between two close mezzanines of the BIS. The Y-pos at 0 and 161 cm correspond to the position of the crimps of the endplugs. For time reasons not all the Y-pos were taken all the weeks, in particular we added the Y-pos at 0, 2, 8, 10, 12, 158 and 161 only after degradation of pulse height, close to gas inlet side, was observed in three tubes: some Y-pos in the middle of the tubes were thus excluded.

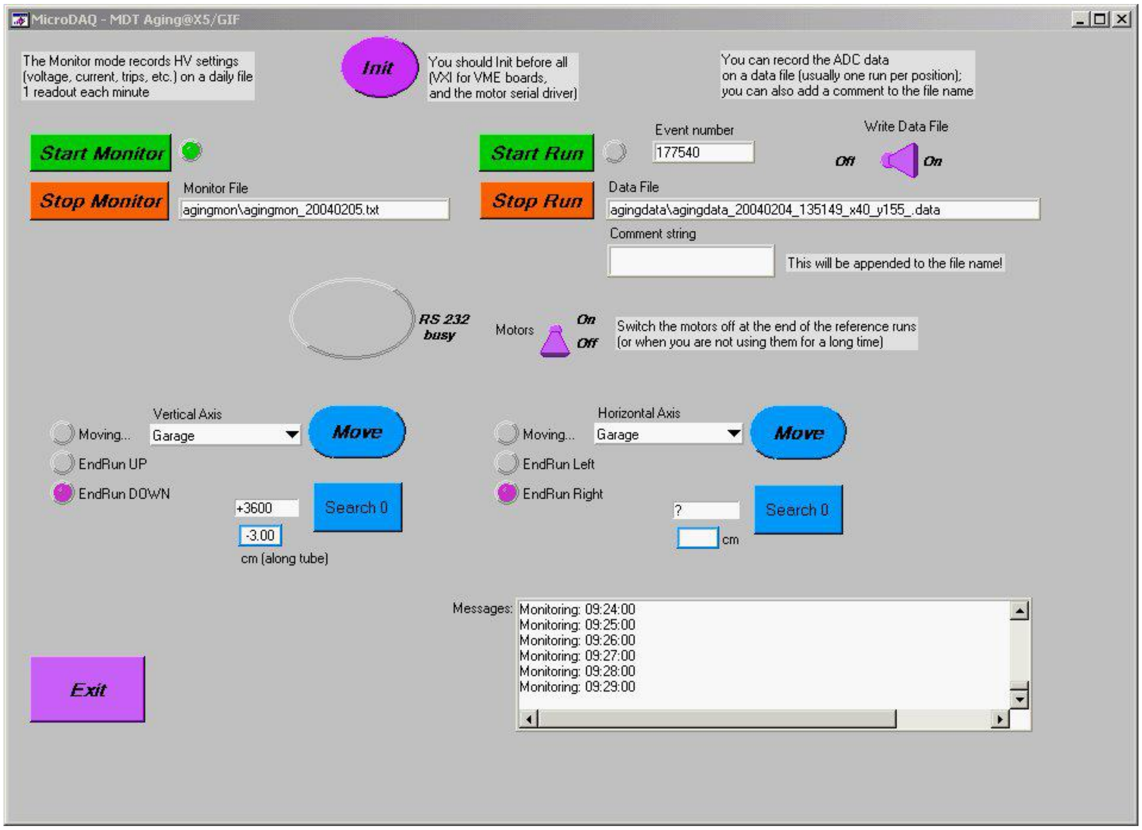

The Monitor mode records HV settings (voltage, current, trips, etc.) on a daily file 1 readout each minute

You should Init before all (VXI for VME boards, and the motor serial driver)

You can record the ADC data on a data file (usually one run per position); you can also add a comment to the file name

Event number: 177540

Monitor File: agingmon\agingmon_20040205.txt

Data File: agingdata\agingdata_20040204_135149_x40_y155_.data

Comment string:

This will be appended to the file name!

Switch the motors off at the end of the reference runs (or when you are not using them for a long time)

Vertical Axis: Garage

+3600

-3.00 cm (along tube)

Horizontal Axis: Garage

?

cm

Messages:

```
Monitoring: 09:24:00
Monitoring: 09:25:00
Monitoring: 09:26:00
Monitoring: 09:27:00
Monitoring: 09:28:00
Monitoring: 09:29:00
```

Figure 4.17: The MicroDAQ control panel.

4.9 Analog signals

In figure 4.18 it is shown the ^{241}Am signal as seen by an oscilloscope mounted in the ADC position. In figure 4.19 we reported the background on the same tube. As it was expected from the theory and the simulations, a signal generated from the ^{241}Am source is approximately 200-300 ns long, with a very sharp and clear peak. A muon signal is longer, until 700 ns long,with smaller maximum. This behaviour is in good agreement with our preliminary results, described in 4.6. As discussed there, when integrating the charge collected in the first 15÷20 ns, the γ signal exhibits a saturation effect, contrary to the muon one. We decided to set the threshold of the discriminators to -30 mV. With this threshold the rate of the background was less than 10% of the signal rate, but at the same moment it is clear (as confirmed by the pulse height spectra that will be shown in the next paragraph) that we are not discarding “interesting” γ events.

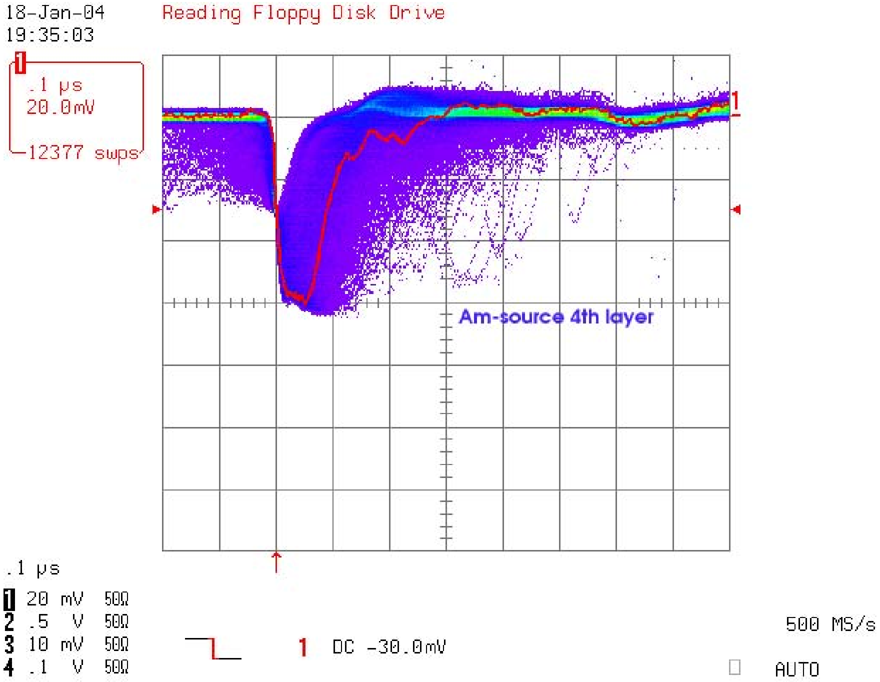

Figure 4.18: The signal generated by the ^{241}Am on a tube of the fourth layer. The oscilloscope scales are 20 mV and 0.1 μs. The threshold is set to -30 mV, the same value of the discriminators threshold. The violet-blue gradient is proportional to the persistency of the signals.

4.10 Analysis diagram and ADC Spectra

The signals which cross the discriminator threshold, as already mentioned, are integrated in an ADC with a gate of 500 ns. The data are stored in the DAQ pc by the MicroDAQ software in binary format to maximize the speed of the data acquisition. The data files are then transferred on a storage area on the University of Roma pcs farm and are ready to be analysed. A C++ program ("decode_fit") was written to perform the data analysis. This program decodes the data, fills the histograms with the pulse height spectra for each tube, fits the pedestal and the peak of the 60 keV γ. It produces a .root file used to check all the analysis chain for each channel and an ascii file containing the values of the 60 keV peak (pedestal subtracted) with its statistical error for all the channels in ADC counts unit:

$$Q_{60keV} = Q_{peak\_60keV} - Q_{pedestal} \tag{4.4}$$

Another C++ program ("split_fill") correlates the ascii files produced by "decode_fit" with the slowcontrol data. The program "split_fill" produces a summary file with the 60 keV peak value together with the temperature values and the integrated charge for each channel and each Y-pos. A pulse height spectra is shown in figure 4.20. In the spectra it is possible to distinguish four different peaks. The first peak on the left is the pedestal. The entries in the pedestal is about 15 times the entries in the rest of the histogram. This is due to the trigger we used: for each of the 16 channels (connected to the same ADC for the same X-pos) which crosses the discriminator threshold, the gate is opened. Since the illumination of the tubes by the two ^{241}Am sources can be considered uniform, only one every 16 times the gate is opened by the relevant channel. The second, the third, and the fourth peaks correspond to the different γ energies emitted by the ^{241}Am: 14 keV, 35 keV and 60 keV. The variations of the 60 keV peak position are used to measure the variations of gain.

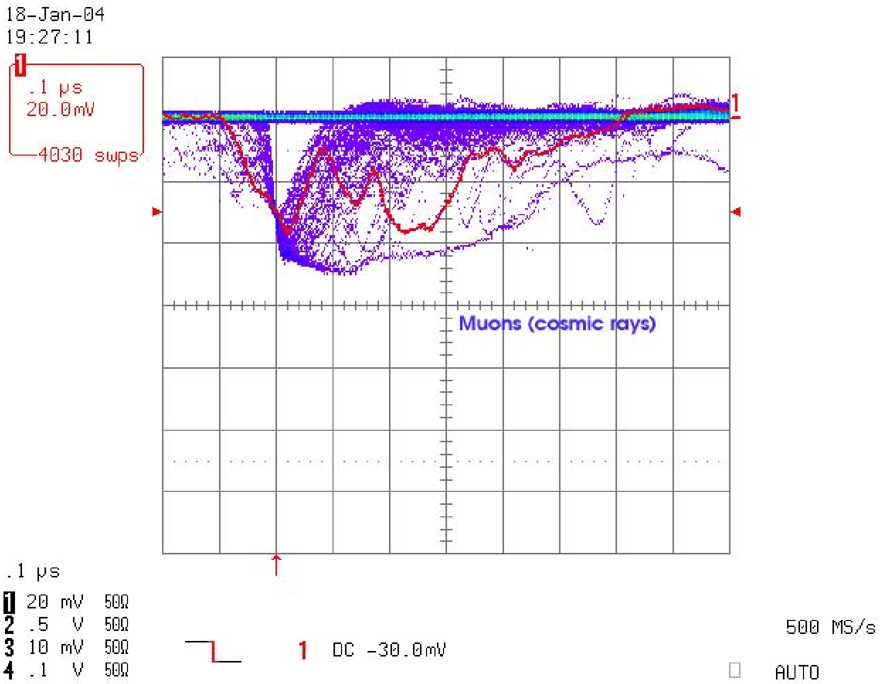

Figure 4.19: The background, mainly cosmic rays, observed on a tube of the fourth layer. The conditions are the same of the ones explained in figure 4.18.

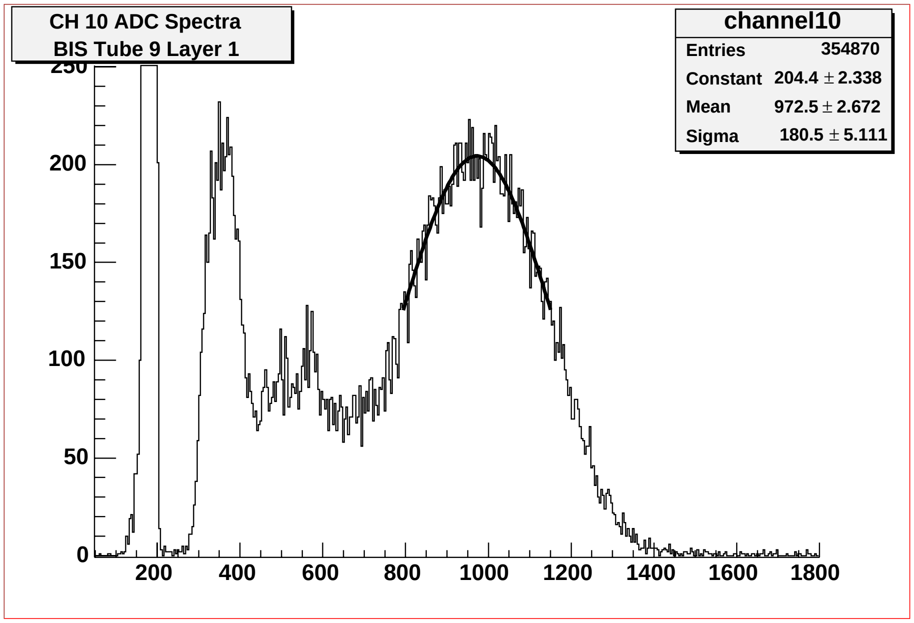

Figure 4.20: A pulse height spectra. On the x-axis there are ADC counts, on the y-axis number of entries.

4.11 System linearity and sensitivity

To understand the sensitivity of the full system, we simulated a variation of gain with an external variable attenuator. It was mounted before the splitters in order to simulate also the possible variations in the number of triggers generated by that channel. The variations of the pulse height spectra is shown in figure 4.21, where the spectra generated by signals without attenuation (color red) are plotted together with the spectra generated by signals attenuated of 1dB (black). The results of the measured attenuation for different values of the attenuator are reported in figure 4.22. The data are normalized to the value of the 60 keV peak without attenuation. The statistical error on each data point is between 0.8% and 1.1% of the value.

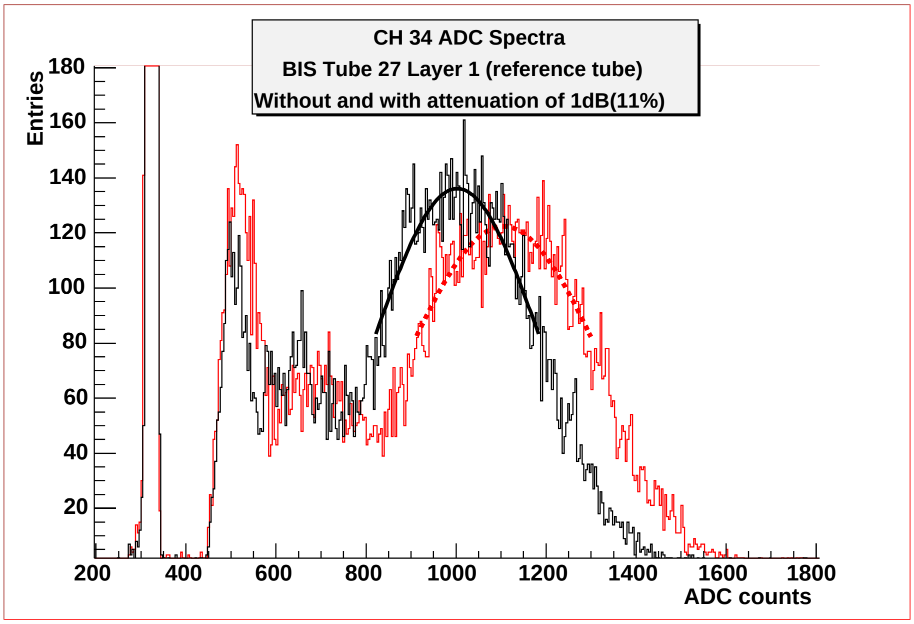

Figure 4.21: Two superimposed pulse height spectra. The red-dotted one is the ADC spectra of the signal without attenuation, the black-solid one corresponds to an attenuation of 1dB (11%).

The overall system sensitivity for the detection of a loss of gain can be estimated around 3%.

From the fit parameters of the data we learn that our system slightly overestimates the gain drops, thus we have to apply a correction:

$$\Delta G_{true} = \frac{\Delta G_{measured} + 0.264}{1.269} \tag{4.5}$$

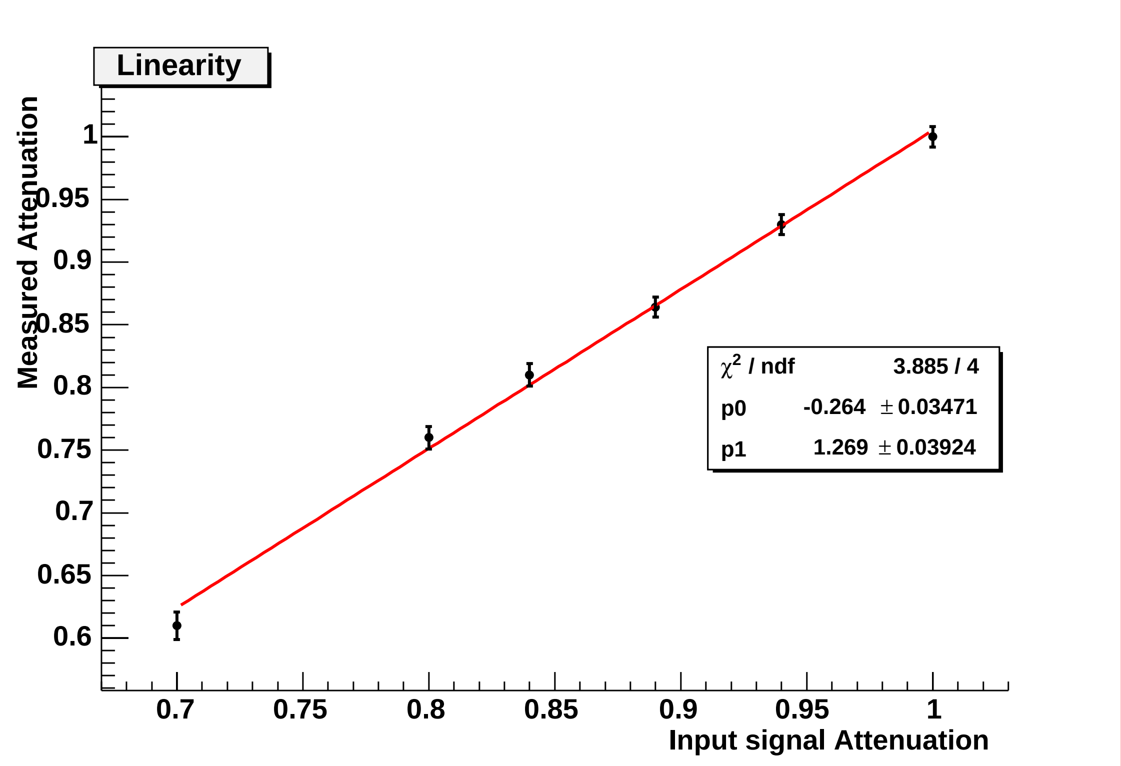

Figure 4.22: The measured attenuation of the 60 keV peak as a function of the value of the attenuator added in the setup. The statistical errors are shown on the data points.

Chapter 5

Ageing test results

5.1 Data taking period and integrated charge

The chambers were irradiated from the 28^{th} of January to the 28^{th} of April 2004. Data were taken once a week during the 6 hours assigned to maintenance on Wednesday, when the GIF source is switched off. During all the remaining time the chambers were irradiated by the GIF source. The figure 5.1 shows the accumulated charge for the BIS a a function of the days from the 28^{th} of January. As already mentioned in 2.10, the maximum expected accumulated charge on the wire, in 10 years of LHC operations, is 600 mC/cm, including the safety factor of 5: a charge of 290 mC/cm was collected by the BIS Beatrice, corresponding to about 50% of the LHC requirements. For the first two weeks of measurements we set the high voltage to 3080 V, that corresponds to a gain of 2×10^4. Then we set the voltage to 3400 V ($G=8\times10^4$) to accelerate the ageing processes, thus increasing the gain (and therefore the accumulated charge) by a factor 4.
The two bundles were slightly out of the irradiation cone of the GIF source, thus they accumulated less charge than the BIS: approximately 55 mC/cm. However one of the goal of the test, which was to verify the good functionality of the reconditioning procedure for tubes affected by dark currents problem (mentioned in 4.4), was reached since the two bundles showed a similar behaviour from the point of view of the integrated charge, and thus the drawn currents, as it is shown in figure 5.2.
During a first part of the test the gas flow was 2 volumes per day, then it was changed to 4 volumes per day on the 10^{th} of march, when the integrated charge was about 110 mC/cm.

Data were taken in three different modes:

- The first mode, during the irradiation period, consists of the weekly reference runs

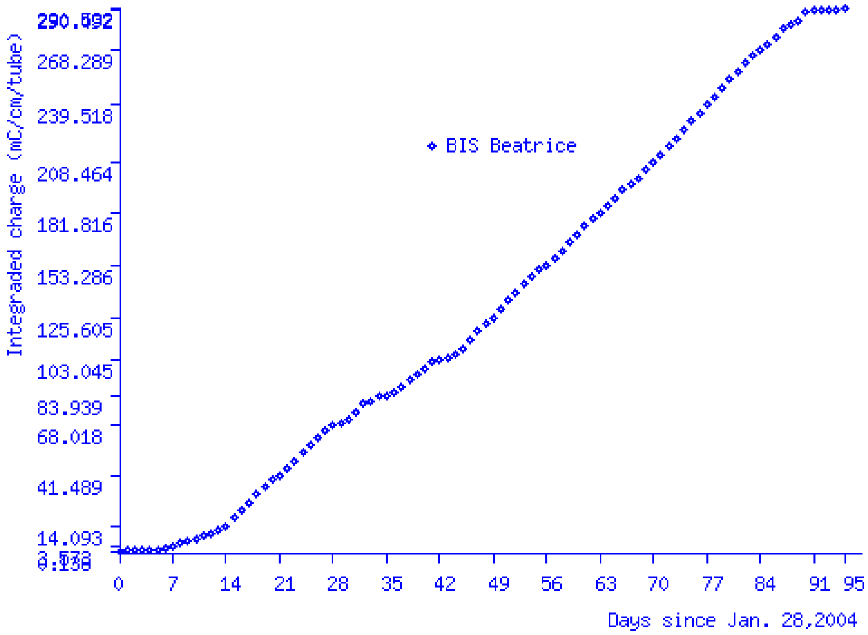

Figure 5.1: Integrated charge for the BIS Beatrice

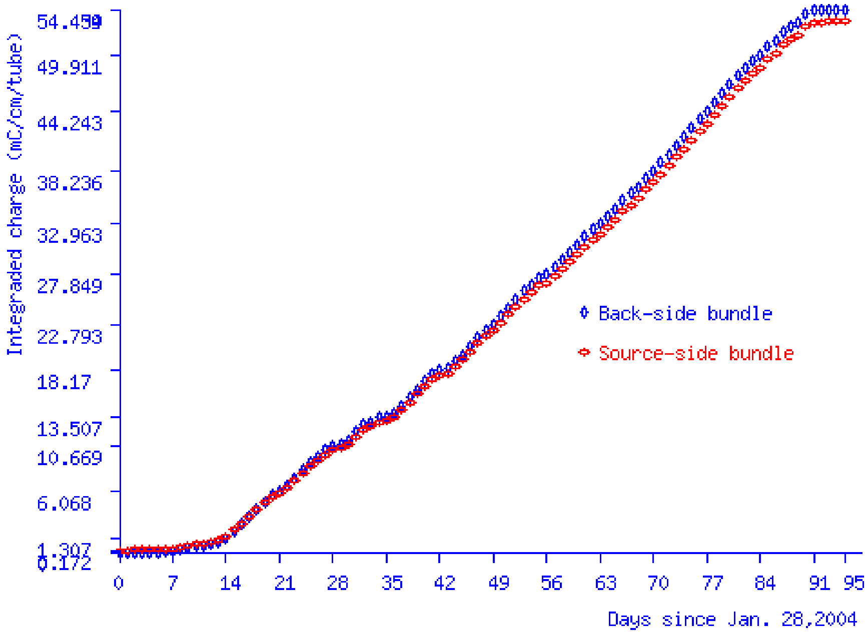

Figure 5.2: Integrated charge for the two bundles.

in the X-pos and Y-pos illustrated in 4.1.
- During the second mode of data taking, just after the irradiation, we recorded all the tubes not read out during the first period. These measurements were performed to improve the statistics on the behaviour of the tubes as a function of the position along the wire after the irradiation. To allow these measurements the BIS mezzanines were displaced, respect to their usual position, by two tubes on the left (to read out the tubes number 1,2,7,8,13,14,19,20,25,26 of each layer), and by two tubes on the right (to read out the tubes number 5,6,11,12,17,18,23,24,29,30 of each layer). The X-pos of the sources were modified in order to irradiate those tubes.
- The third and last data taking mode, from the 6^{th} of May to the 7^{th} of May after the dismantling of the mechanical setup, consists in runs with the BIS in horizontal position outside the GIF area.

Depending on the number of mezzanine irradiated by the two sources (X-pos 10 and 20 irradiate 2 mezzanines each, while X-pos 30 and 40 only one), the runs consist in a different amount of events: ~350000 for X-pos 10,20 and ~175000 for X-pos 30,40. These amounts of events were chosen such to have, for each tube, at least 10000 events generated by the photoelectric interaction of the 60 keV γ.
The recording speed of our DAQ system was of about 1.15 kHz. One run of 350k(175k) events, in average, was performed in 6.5(4) minutes, 1.5 minutes for the sources movements (and control of the position) and 5(2.5) minutes for the data collection.

5.2 Corrections and normalizations

The gain, according to the Diethorn formula 2.6, is dependent mainly on the voltage of the wire and the density of the gas, thus its pressure and its temperature. Since the voltage is kept constant from the high voltage power supply and the pressure from the pressure regulators inside the gas circulation loop, we only monitored that these two parameters remain stable inside the given ranges. On the contrary a variation of the temperature can caused by sources of heat in particular points (like electronics or motors) and by the temperature of the area. The temperature sensors, positioned on the BIS and on the bundle as shown in figure 4.13, were used to apply off-line corrections to the data, as explained in the following. The variation of temperature during all the test is shown in figure 5.3 as a function of the time.
The effects due to the variation of the temperature on the chambers, that can limit the precision in the pulse height measurements, are:
- The vertical temperature gradient due to the presence of the electronics under the BIS. This effect is shown in figure 5.4, where the x-axis is the temperature and the

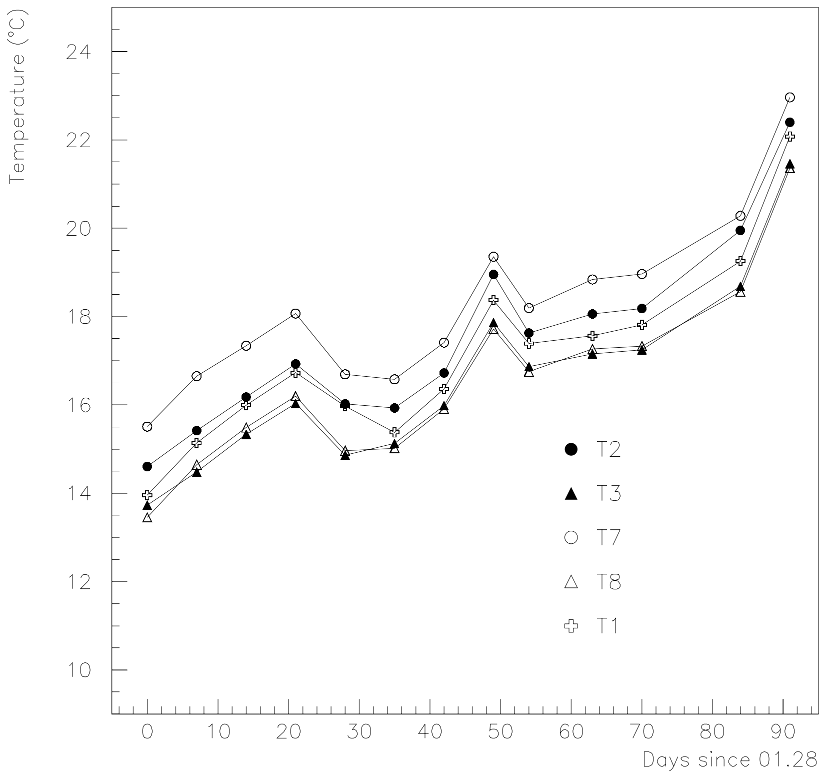

Figure 5.3: Temperature of five sensors on the BIS and on the bundle as a function of the day from the 28^{th} of January. $T1$ is positioned on the center of the BIS, $T7$($T8$) on the bottom(top) left of the BIS, while $T2$($T3$) on the bottom(top) of the bundle.

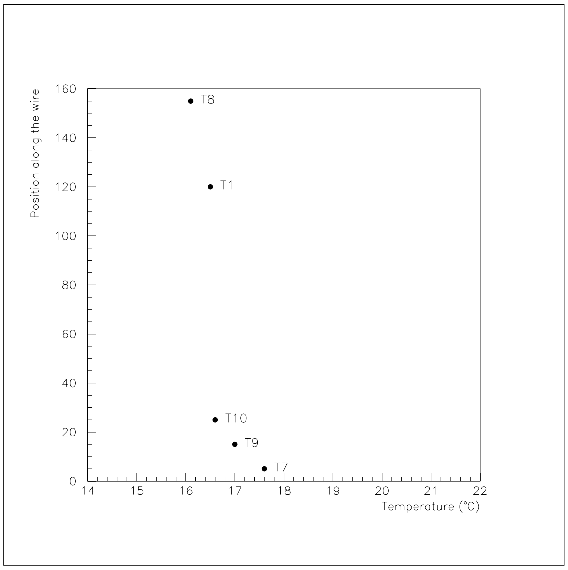

Figure 5.4: The temperature in different positions along the wires, measured by different sensors.

y-axis is the position of the sensor along the tube, measured from the gas inlet. This effect is of the order of 1.5C^o and mainly located in the first 25 cm near the gas inlet: since part of the effect have to be attributed to the electronics, which should affect the air temperature outside of the tubes more than the gas temperature inside the tube, we can neglect this difference.

• The horizontal variation of temperature can be derived from figure 5.3 if we compare the difference between the $T7$ and $T2$ sensors positioned on the bottom left and bottom right of the setup and the difference between the $T8$ and $T3$ positioned on the top left and top right of the setup. This effect is of the order of 1C^o. Clearly we have to correct for it only when comparing different tubes.

• The drift of the external temperature during the test over a period of ∼100 days: it is of the order of 10C^o, as we can see from figure 5.3. This is a global effect, in fact all the temperature sensors drift together and their differences remain constant. When comparing different tubes, we have also to correct for the possible different response of the electronic chain (mezzanine, cables, ADC).

We can use different approaches to show the variation of gain due to ageing effects either as a function of the accumulated charge on the wire or as a function of the position along the wire. It is useful to define:

• the 60 keV peak pulse height as a function of the accumulated charge (mC/cm) for a given tube ($tube$) at temperature T as:

$$Q_{60keV}(mC/cm, Ypos, tube, T) \tag{5.1}$$

- the intercalibration factor to a reference value as:

$$Intercalib(tube) = \frac{Q_{60keV}(Zero.mC/cm, Ypos, tube, T)}{Q_{60keV}^{meanYpos}(Zero.mC/cm, tube, T)} \tag{5.2}$$

- the temperature correction: we fitted the slope α of the Q_{60keV} versus temperature for each channel and each Y-pos using data in a wide range of temperatures, as shown in figure 5.5. We used the average of these fits as temperature correction factor[1] at a reference temperature. Our data were corrected to 14C^o, the average temperature when we started the test.

$$\begin{aligned}&Q_{60keV}^{temp.corr}(mC/cm, Ypos, tube) = \\ &Q_{60keV}(mC/cm, Ypos, tube, T) \cdot [1 + \alpha(T - 14)] \cdot Intercalib(tube)\end{aligned} \tag{5.3}$$

The global effect of the corrections can be evaluated from figure 5.6. We plot the values of $Q_{60keV}^{temp.corr}$ for Y-pos=85 cm from all the tubes of a typical mezzanine for the complete data taking period. The relative width of the distribution is $\sigma/mean \sim 2\%$. Notice that this figure alone shows that no drop effect is present within ~2%.

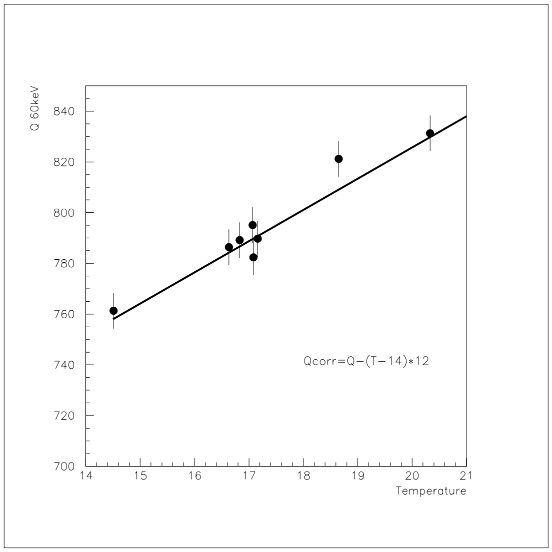

Figure 5.5: Q_{60keV} as a function of the temperature for one channel at 85 cm.

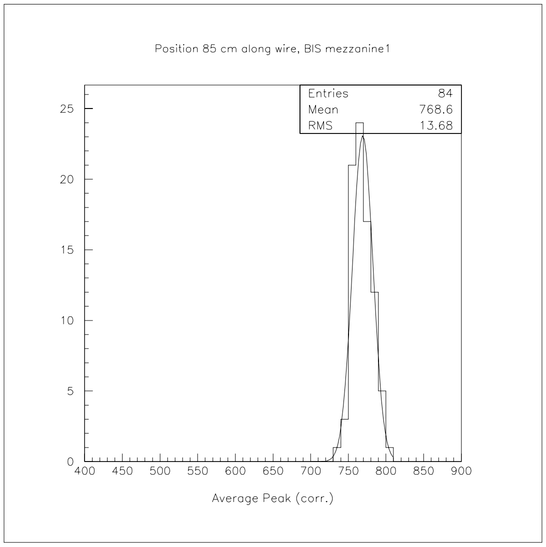

Figure 5.6: $Q_{60keV}^{temp.corr}$ distribution for different tubes at 85 cm.

We explain here two of the possible approaches to show the gain variations:

---

[1] We stress that the shape of the temperature variation 5.3 allows to decouple the temperature effects from a possible drop due to irradiation. This would not be the case if the temperature dependence on time were monotonic.

- Each tube can be compared with one of the reference tubes which had not accumulate charge since they were disconnected from the high voltage. For each Y-pos as a function of the accumulated charge, or for each accumulated charge as a function of the Y-pos, we could plot the ratio:

  $$R_1 = \frac{Q_{60keV}^{temp.corr}(mC/cm, Ypos, tube)}{Q_{60keV}^{temp.corr}(Zero.mC/cm, Ypos, Ref.tube)} \tag{5.4}$$

  Using this method we have to apply the correction due to the different intercalibration of each channel, the one due to the variation of the external temperature, and to use at least two different tubes (one is the reference).

- The relative variation of gain of each tube and for each position along the wire can be studied, as a function of the integrated charge. Thus, for each Y-pos, a ratio can be plotted as a function of the integrated charge:

  $$R_2 = \frac{Q_{60keV}^{temp.corr}(mC/cm, Ypos, tube)}{Q_{60keV}^{temp.corr}(Zero.mC/cm, Ypos, tube)} \tag{5.5}$$

  To compare pulse height measurements at different position along the wire we can also plot the numerator of 5.5 as a function of Y-pos. In this way the results are not dependent on the reference tubes.

Both the ratios should have as expected value 1, if no gain drops were measured. We observed that the two explained methods gives compatible results. We decided to use the second one because it is simpler to implement, and because each measurements depends only from one channel and not also from the behaviour of the reference tubes.

5.3 Data analysis results

From now on, we refer to the results coming only from the BIS tubes, unless explicitly explained, since the bundle accumulated too few charge to compare its results to the BIS ones.

5.3.1 Dependence on the integrated charge on the wire

During the irradiation period only 3 out of 40 (32 irradiated, 8 reference) monitored tubes showed ageing effects, none of the 8 reference ones. The three affected tubes are the tubes number 4, 10 and 16 on the third layer.
At the beginning of the test, only Y-pos at 5, 15, 25, 35 cm were recorded. However,

after discovering the ageing problems, also all the other Y-pos reported in 4.1 were included.

For the three affected tubes $Q_{60keV}^{temp.corr}$ at Y-pos=5 cm is shown in figure 5.7 as a function of the integrated charge. Also three of the remaining 29 irradiated tubes that did not show any ageing effect are plotted.

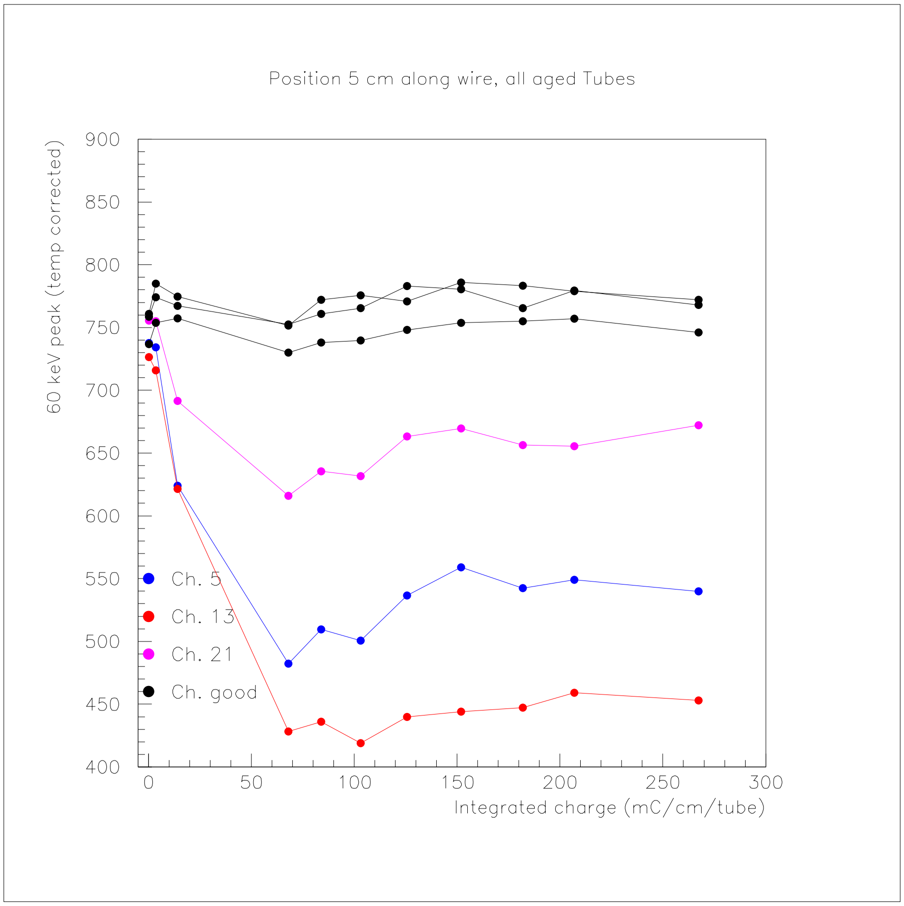

Figure 5.7: Pulse height $Q_{60keV}^{temp.corr}$ as a function of the integrated charge at 5 cm from the gas inlet. The ADC $Ch.5$(blue) on the plot corresponds to the tube number 4 in layer 3, $Ch.13$(red) and $Ch.21$(violet) to the tubes 10 and 16 always of the third layer. The three $Ch.good$ are a sample of the 29 irradiated tubes which did not show ageing effects.

For these 3 tubes the pulse height $Q_{60keV}^{temp.corr}$, only at 5 cm from the gas inlet, started decreasing right after the beginning of the irradiation. The pulse height decreased to about 60÷90% of its original value until about 70 mC/cm of integrated charge. At that point it became approximately stable and stayed on a plateau. The pulse height remains stable even after the gas flow was changed from 2 volumes per day to 4 volumes per day on the 10^{th} of March (110 mC/cm). The behaviour is similar

for all the three tubes (see figure 5.7).
For the three affected tubes it was not seen any effect at Y-pos=15 cm. Their behaviour as a function of the integrated charge is similar to the one of the other 29 not-affected tubes. In figure 5.8 the $Q_{60keV}^{temp.corr}$ versus the accumulated charge at 15 cm from the gas inlet is reported. We studied also the gas outlet zone, where

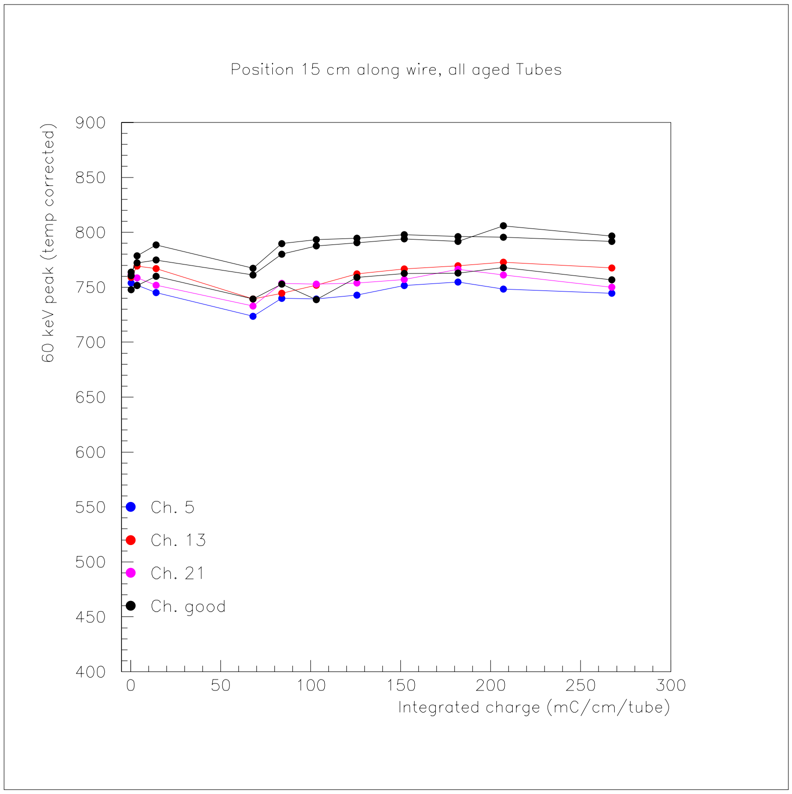

Figure 5.8: Pulse height $Q_{60keV}^{temp.corr}$ as a function of the integrated charge at 15 cm from the gas inlet. $Ch.5$(blue), $Ch.13$(red) and $Ch.21$(violet) correspond to tubes number 4, 10 and 16 of layer 3.

we didn't find ageing effects for any tubes. In figure 5.9 the $Q_{60keV}^{temp.corr}$ versus the integrated charge at the Y-pos 35 and 85 cm is plotted. The pulse height $Q_{60keV}^{temp.corr}$ is shown in figure 5.10 as a function of the integrated charge at Y-pos=120 cm and 155 cm, 40 and 5 cm from the gas outlet. No ageing effect is visible at the gas outlet.

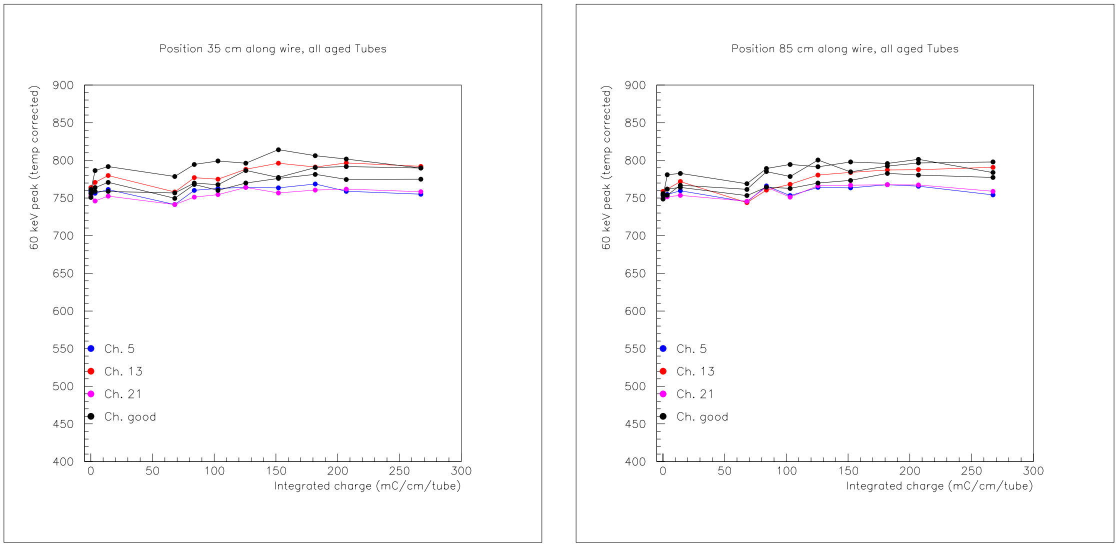

Figure 5.9: Pulse height $Q_{60keV}^{temp.corr}$ as a function of the integrated charge at 35 cm (on the left) and at 85 cm from the gas inlet. $Ch.5$(blue), $Ch.13$(red) and $Ch.21$(violet) correspond to tubes number 4, 10 and 16 of layer 3.

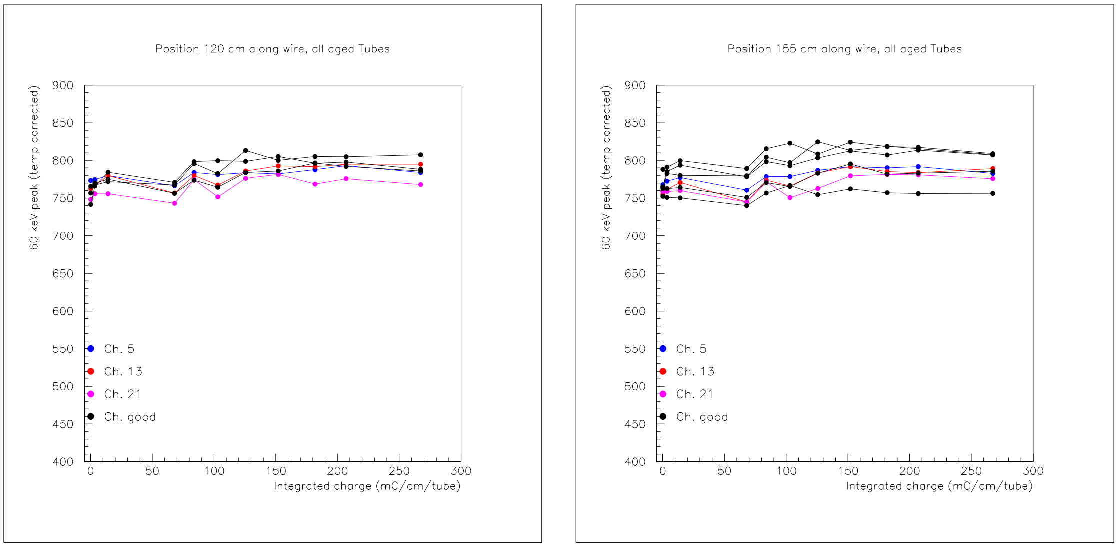

Figure 5.10: Pulse height $Q_{60keV}^{temp.corr}$ as a function of the integrated charge at 120 cm (on the left) and at 155 cm from the gas inlet. $Ch.5$(blue), $Ch.13$(red) and $Ch.21$(violet) correspond to tubes number 4, 10 and 16 of layer 3.

5.3.2 Dependence on the position along the wire

Four weeks after the beginning of the irradiation we realized that there were three tubes which showed ageing effects on the first few centimeters of the wire. The accumulated charge up to that moment, the 25th of February, was 68 mC/cm.

In figure 5.11 we plotted the behaviour of the three affected tubes, compared with other tubes that didn't show ageing effects, as a function of the distance from the gas inlet. The integrated charge corresponding to the day in which we took these data is ∼70 mC/cm.

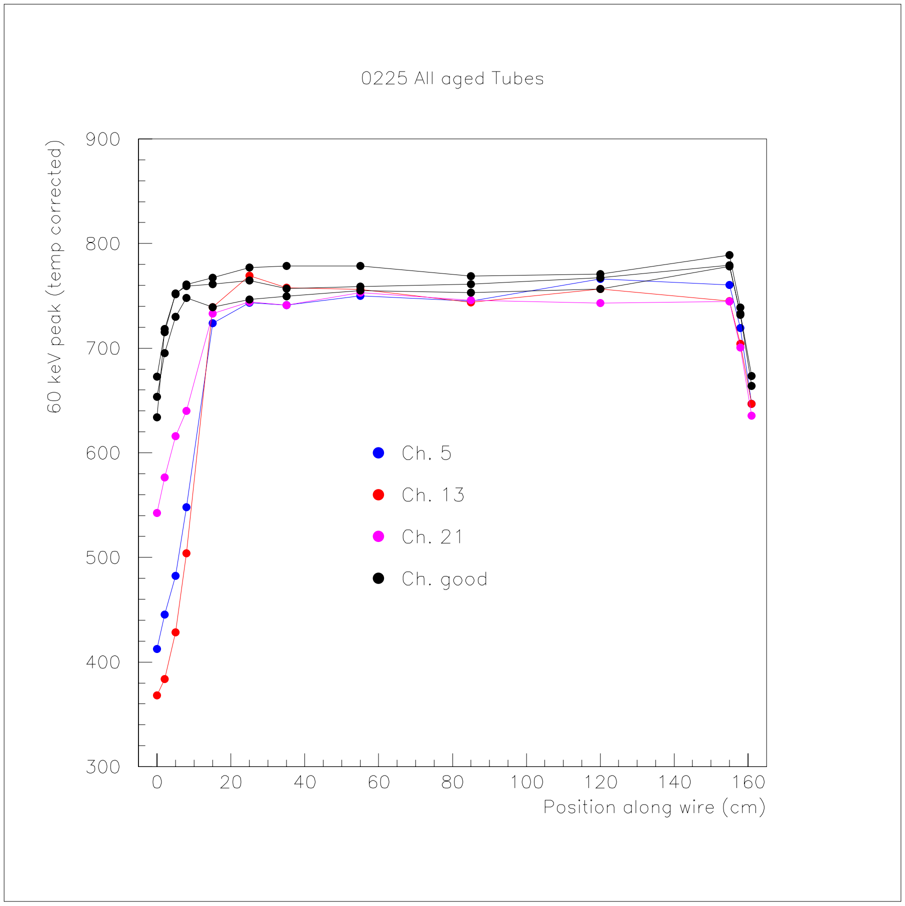

Figure 5.11: Pulse height $Q^{temp.corr}_{60keV}$ as a function of the position along the wire, at an integrated charge of 68 mC/cm. The tubes shown are the same as in the previous pictures.

In 5.11 we can figure out the "normal" pulse height drop close to the gas outlet endplug for all the tubes. This effect is due to the distortions of the electric field, and for the three "good" tubes it is the same at the gas inlet side. For the three affected tubes the behaviour is different at the gas inlet side from the gas outlet side.

It can be seen also from the figure 5.12 where a zoomed view of the pulse height over the first 40 cm from the gas inlet is plotted. In figure 5.13 it is shown the behaviour of one of the three affected tubes (tube 10) in the first 40 cm for different integrated charges.

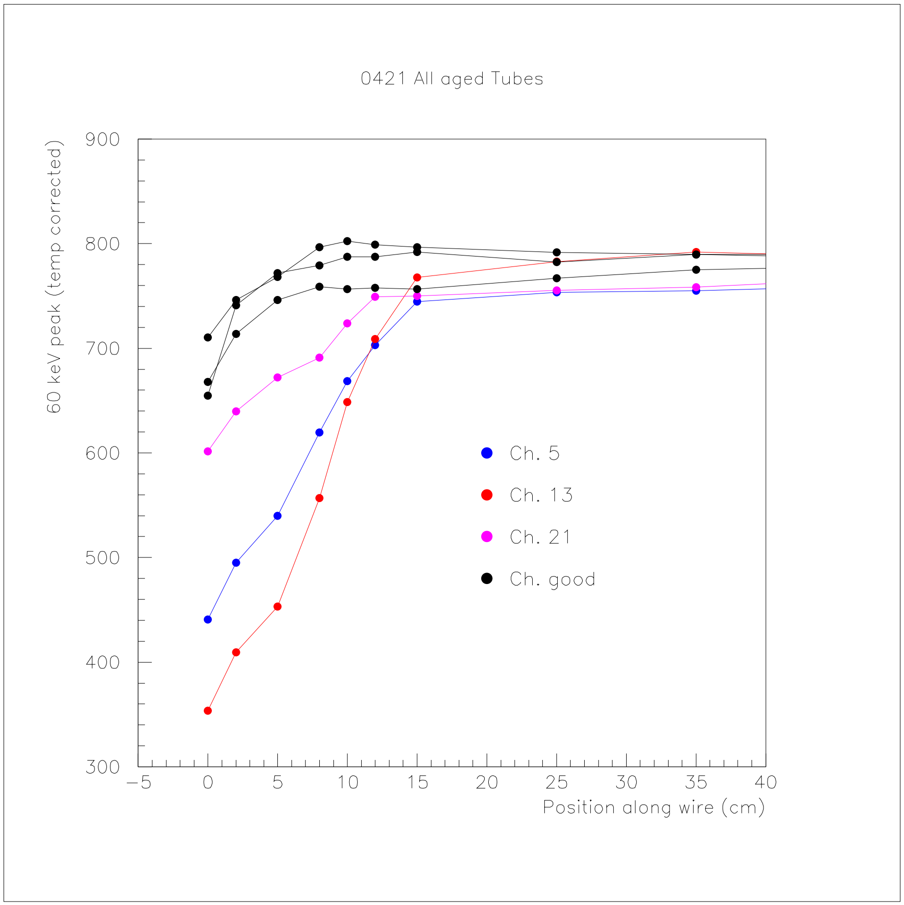

Figure 5.12: Pulse height $Q_{60keV}^{temp.corr}$ over the first 40 cm from the gas inlet, at an integrated charge of 270 mC/cm. The tubes shown are the same as in the previous pictures.

From this plot, together with the one reported in figure 5.7, we can see that the ageing stopped after 70 mC/cm, over a zone of approximately 10÷12 cm. We cannot be more accurate with these measurements on the dimension of the zone affected by this ageing effect since the BIS wire zone illuminated by the ^{241}Am γ is ∼3 cm long, for mechanical construction of the collimators.

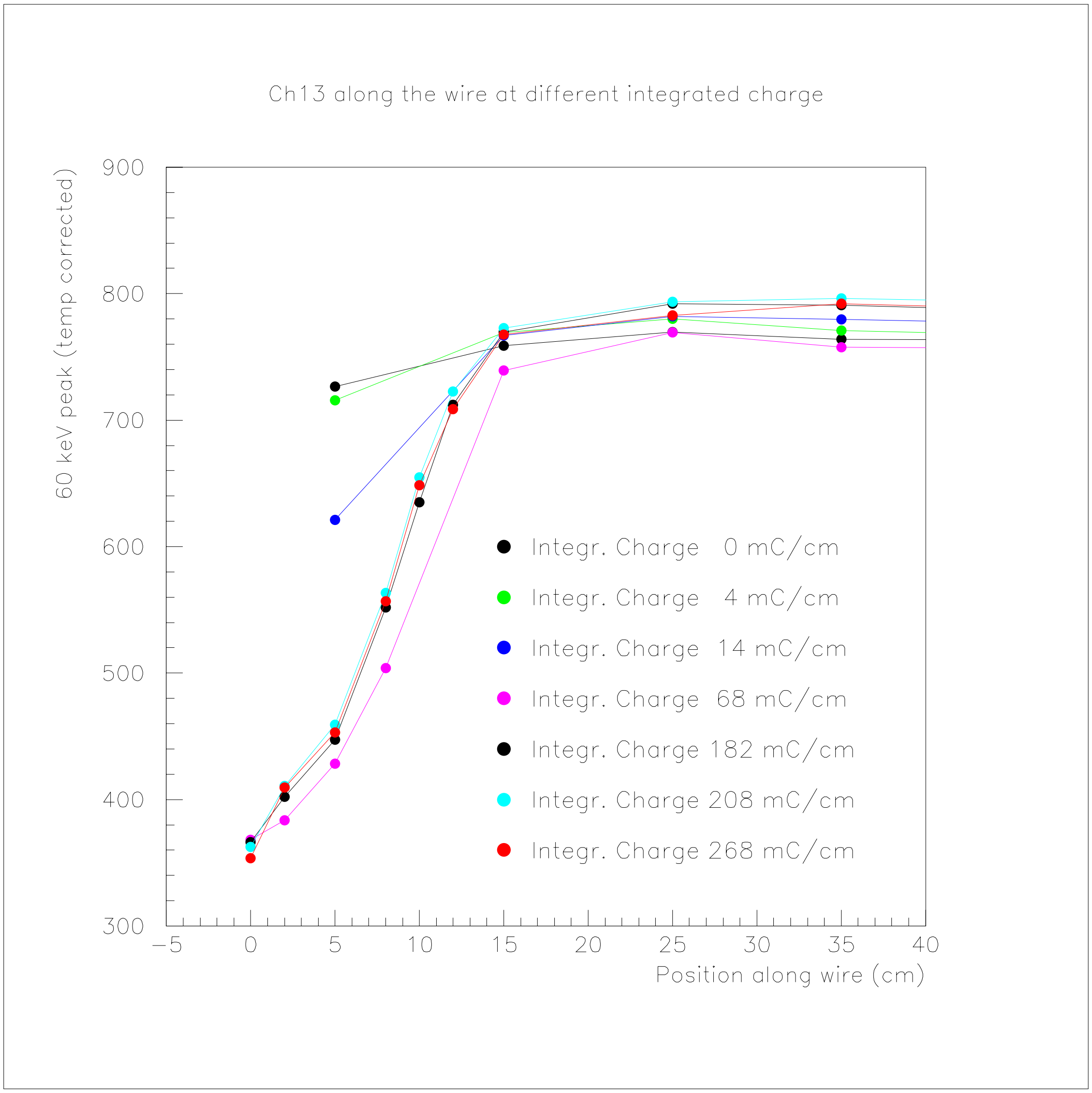

Figure 5.13: Pulse height $Q_{60keV}^{temp.corr}$ over the first 40 cm from the gas inlet, at different integrated charges. $Ch.13$ is tube 10 of layer 3.

5.3.3 BIS final results

At the end of the irradiation period the 28^{th} of April, before dismantling the setup, we decided to read out all the tubes that we couldn't have monitored during the irradiation period.
Since we noticed a different dependency of the pulse height drop on the distance from the gas inlet between the three affected tubes and the other tubes, we performed the analysis of the pulse height as a function of the position along the wire as we did for the 40 tubes monitored during the irradiation period. Then we compared the results.
The readout setup was modified as explained in 5.1. The behaviour of 11 out of 64 tubes was found similar to the one shown by the three affected tubes. Also the range of pulse height drop was consistent with the results shown in figure 5.12. The three tubes studied for the duration of the test were a good sample to describe the observed ageing effect.

We decided to separate the tubes with the proper functionality, after 290 mC/cm of integrated charge, from the tubes with ageing effects, in terms of the variable $\Delta G/G$. Such a variable is defined as the ratio between the $Q_{60keV}^{temp.corr}(5cm)$ and the average of the $Q_{60keV}^{temp.corr}(Y-pos)$ at 15, 25 and 35 cm. This ratio is corrected for the linearity of the system to obtain the real gain reduction, as explained in 4.5, at 5 cm from the gas inlet:

$$\Delta G/G = (\frac{Q_{60keV}^{temp.corr}(5cm)}{Q_{60keV}^{mean}(15,25,35cm)} + 0.264)\frac{1}{1.269} \tag{5.6}$$

In figure 5.14 we showed the results for all the BIS irradiated tubes: 14 out 96 showed a $\Delta G/G > 5\%$. The effect is not uniformly spread over the four layers. This is probably due to the fact that the causes of the observed ageing effect are to be searched inside particular pieces dedicated to the third layer.

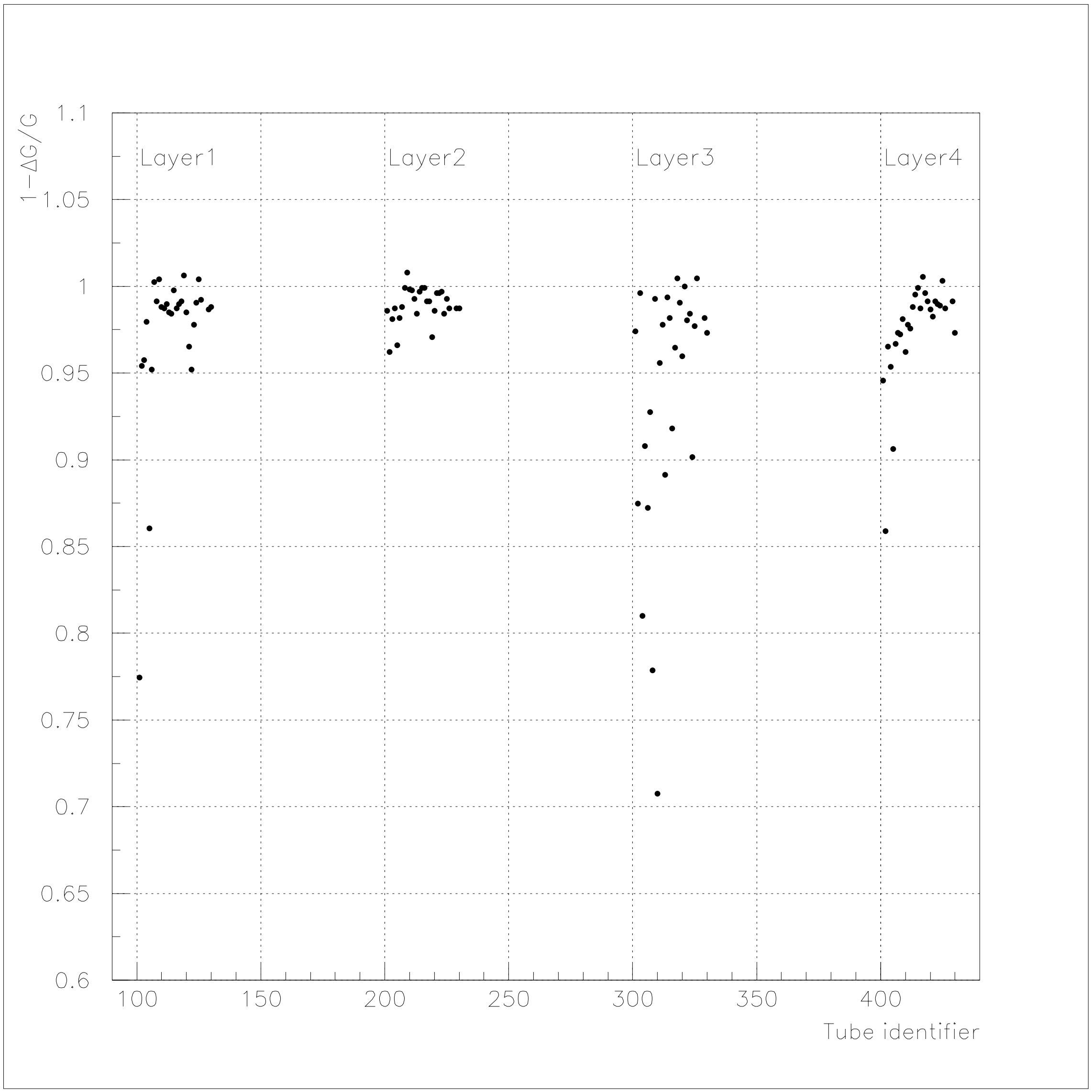

Figure 5.14: $1 - \Delta G/G$ for the BIS tubes.

5.4 Further analysis

Since the ageing effect was not seen in all the tubes, as it happened in the previous tests, there is the possibility that a kind of contaminant, probably Silicon, was present only in some pieces of the BIS, but not in the gas recirculation loop. In this hypothesis, the time variation of the effect is due to the small amount of the contaminant, which apparently flushed out in the first period of irradiation.
In order to confirm the hypothesis, SEM (Scanning Electron Microscope), EDX (Energy Dispersive X-ray) and FTIR (Fourier Transform InfraRed spectroscopy) analysis methods were used.

5.4.1 Wire analysis with the SEM and EDX techniques

We opened some BIS tubes, to take out the wires, and to analyse them with the scanning electron microscope and the energy dispersive x-ray analysis methods. We analysed three tubes, all from the third layer, two affected by ageing (tubes 4, 10) and one not affected (tube 12). In figure 5.15 the gas inlet part of the wire of one of the not affected tubes is shown. The wire does not present any kind of deposits.

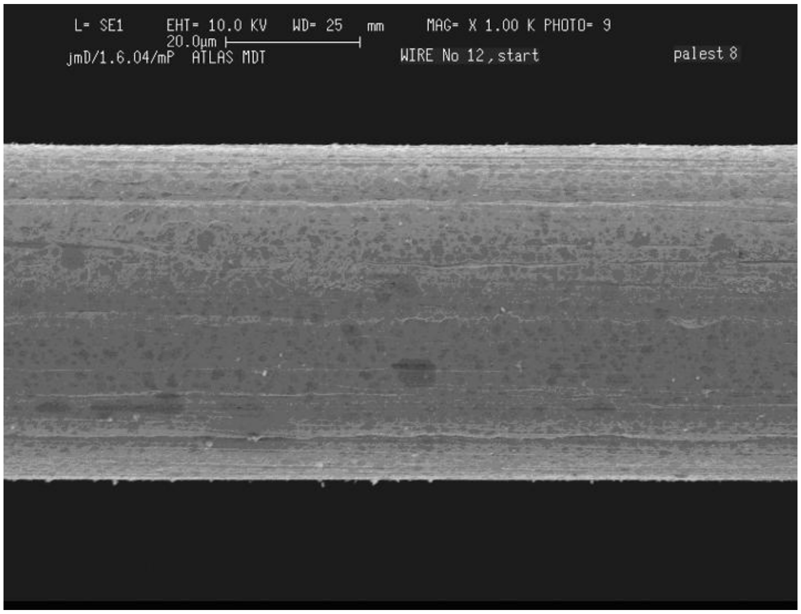

Figure 5.15: Micrograph of the tube 12 layer 3, not affected by ageing, at the beginning of the wire from the gas inlet side. No deposits are present.

On the contrary, micrographs of the affected tube confirmed the presence of needle-like growth perpendicular to the wire surface. The dimensions of these structures

decrease with the distance from the gas inlet, in agreement with the pulse height drops measured.
In figure 5.16 the gas inlet part of the wire of one of the affected tubes is shown. The energy dispersive x-ray analysis confirmed that the deposits are mainly done of Silicon and Oxygen, as reported in figure 5.18.

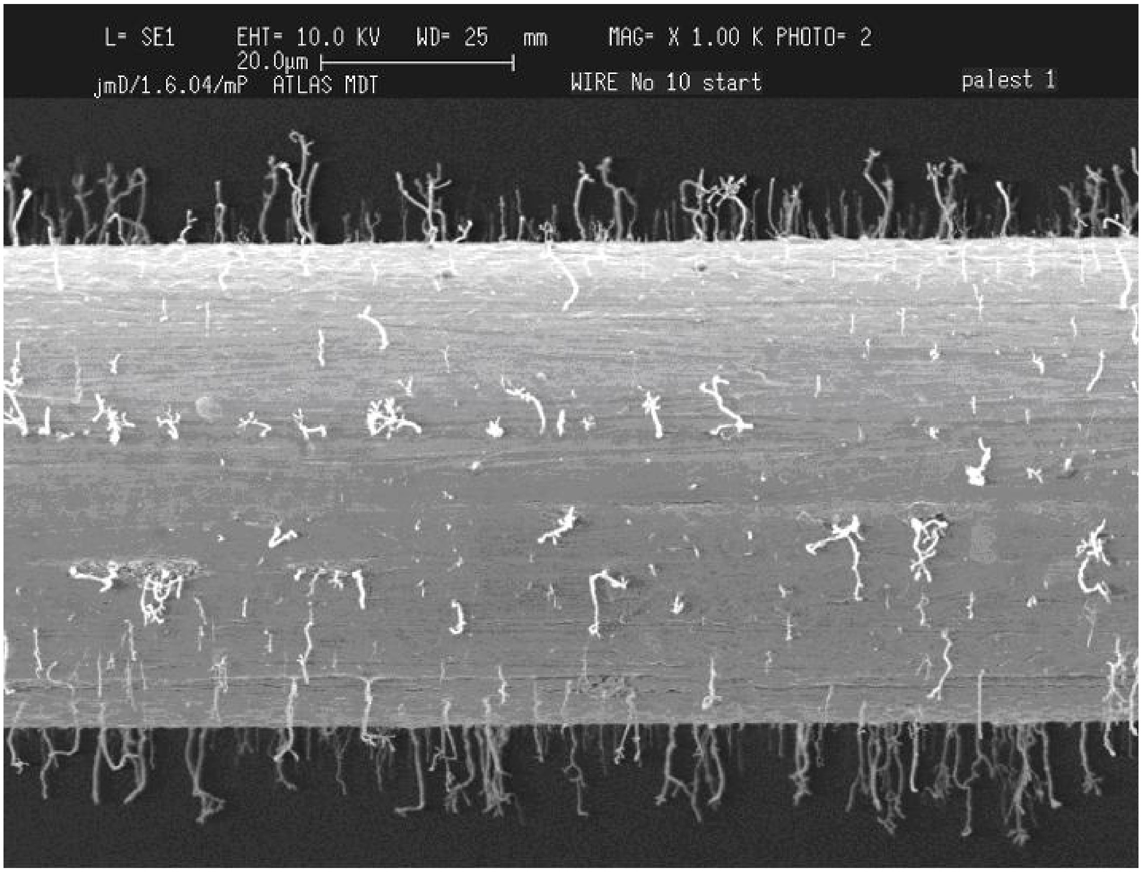

Figure 5.16: Micrograph of the tube 10 layer 3, affected by ageing, at the beginning of the wire from the gas inlet side.

In figures 5.19 and 5.20 we show the wire of tube 10 at different distance from the gas inlet. The wire at 15 cm does not present Silicon deposits, thus confirming our hypothesis of a localized ageing effect limited to the first 10÷12 cm from the gas inlet.
In figure 5.21 we display a special germination which was found on the tube 10, at the beginning of the wire. This was probably caused by a dust particle already present on the wire before the beginning of the test. Only very few germinations like this one were found on the wires. Their impact on the gain drops is negligible.

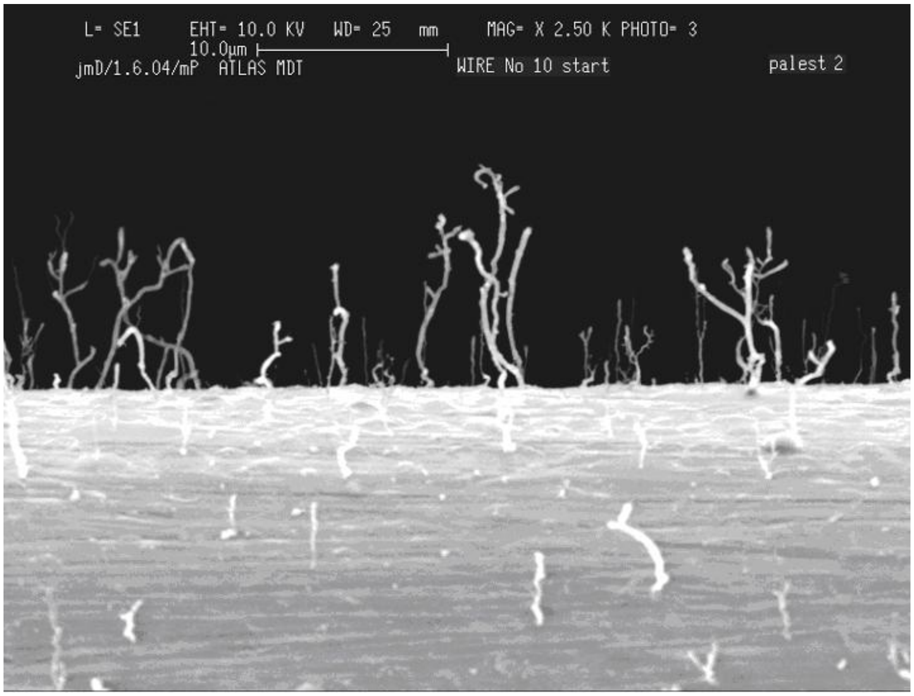

Figure 5.17: Detailed view of picture 5.16. Whiskers of ~5μm length are visible.

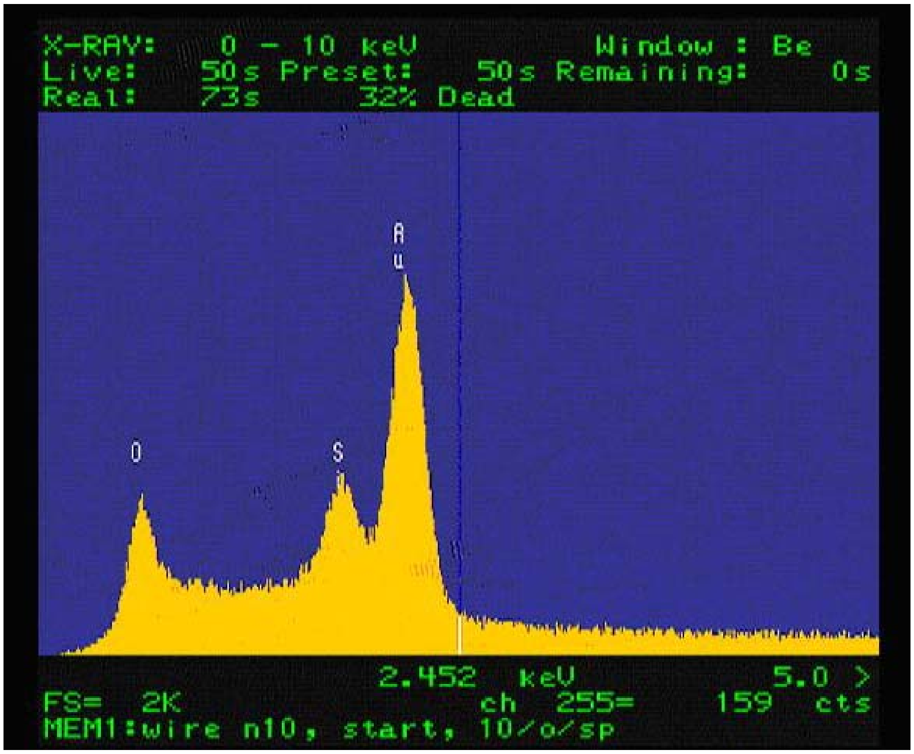

Figure 5.18: Energy dispersive x-ray spectrum of a whisker. Silicon and Oxygen elements are present.

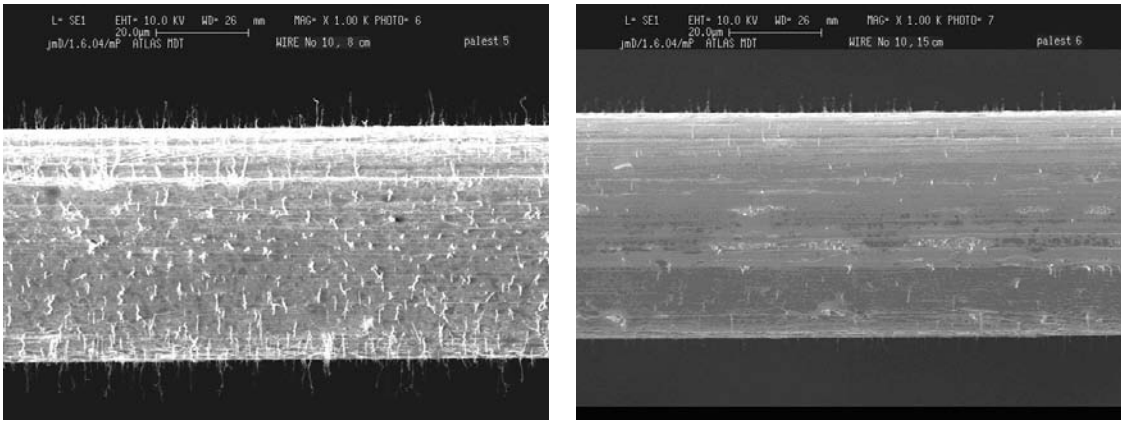

Figure 5.19: Deposits on tube 10 at 8 (left) and 15 cm. Already at 15 cm from the gas inlet the wire does not present deposits, as the pulse height measurements had shown.

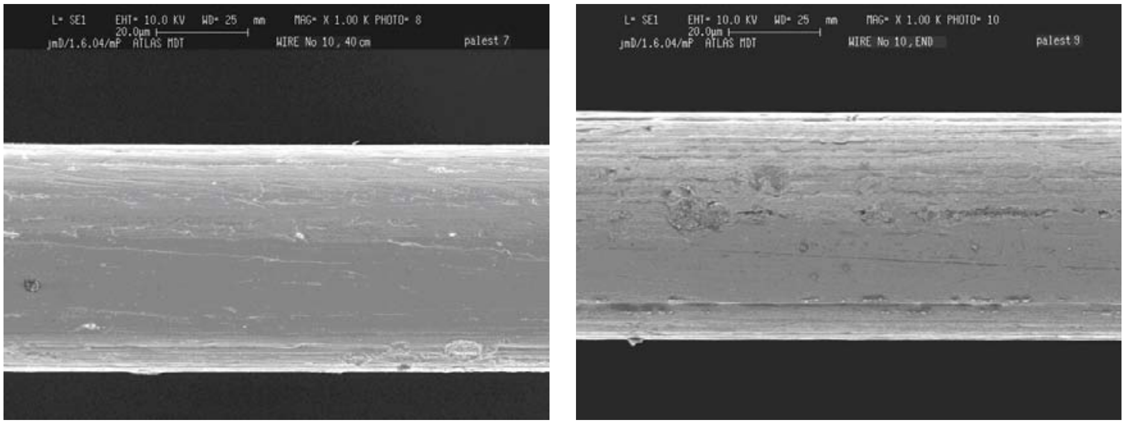

Figure 5.20: Deposits on tube 10 at 40 (left) and 160 cm (the end of the wire on the gas outlet side). On the gas outlet side the wire is perfectly clean.

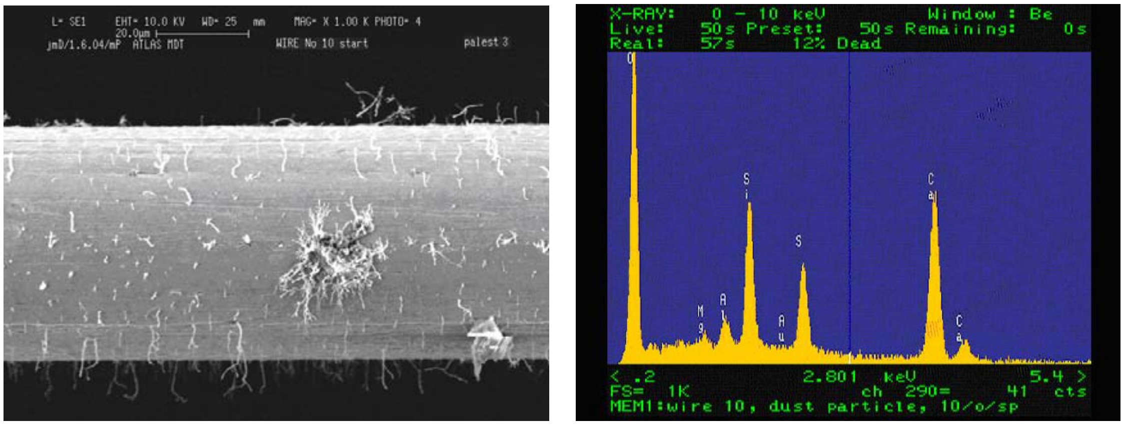

Figure 5.21: A special germination on a probably preliminary dust deposit on tube 10 at the beginning of the wire (left) with the relative EDX. Ca, S and Mg are consistent with the hypothesis of a dust particle.

5.4.2 Tubelets analysis with the Fourier Transform InfraRed spectroscopy

After the confirmation on the contaminant nature, Silicon, we tried to find the source of this contaminant. Since the ageing effects is not uniform among all the tubes, as figure 5.14 shows, we decided to analyse the gas components not common to each tube.
As explained in 2.2.7, the BIS gas distribution is fully parallel (see figure 2.14). Thus we decided to analyse some tubelets of the BIS, one of the gas components different for each tube.
The possible source of this contamination could be the improper cleaning of these tubelets. Since during the cleaning procedure the tubelets are divided in batch of different shape, thus corresponding to different layers, an improper cleaning could explain the results we observed where one layer showed ageing effects on ∼50% of its tubes, while the other layers only on 0÷10% of their tubes.

In order to find out if something was wrong in the cleaning procedure of these components, some tubelets from BIS and some reference tubelets from the same cleaning batch as those ones on BIS layer 3, but not used before, were analyzed with the Fourier Transform Infrared Spectroscopy technique. We were looking for different kind of pollution, in particular Silicone traces.
The FTIR method is a vibrational technique which identifies different components by their vibrational states. The technique consists in shining a range of infra-red frequencies one at a time through a sample of an organic compound (like hexhane) flushed in the tubelets, and, with a detector, measure how much of a particular frequency gets through the compound in terms of percentage transmittance. The fingertip of the Silicon compounds is 500÷1500cm^{-1}, the one of some Carbon compounds is 2500÷3500cm^{-1}, the water infrared spectrum is ∼1600cm^{-1}.
The sample of 5 tubelets from the BIS chamber was composed by two tubelets from affected tubes, one of layer one and one of layer three, and three tubelets from not affected tubes, one of layer one and two of layer three. Figure 5.22 shows the transmittance plot of an affected tube (tube 16 layer 3), while figure 5.23 shows the transmittance plot of a not affected tube (tube 12 layer 3). In figure 5.24 we show the transmittance plot of the five reference tubelets.

Two tubelets (tube 11 and 16 layer 3, one belonged to a tube showing ageing, the other belonging to a tube not showing ageing) showed a slightly different pollution. However no clear signal for Silicon compounds could be observed.
The results for the other 3 BIS tubelets and for the set of five tubelets not used before did not show the presence of pollution.

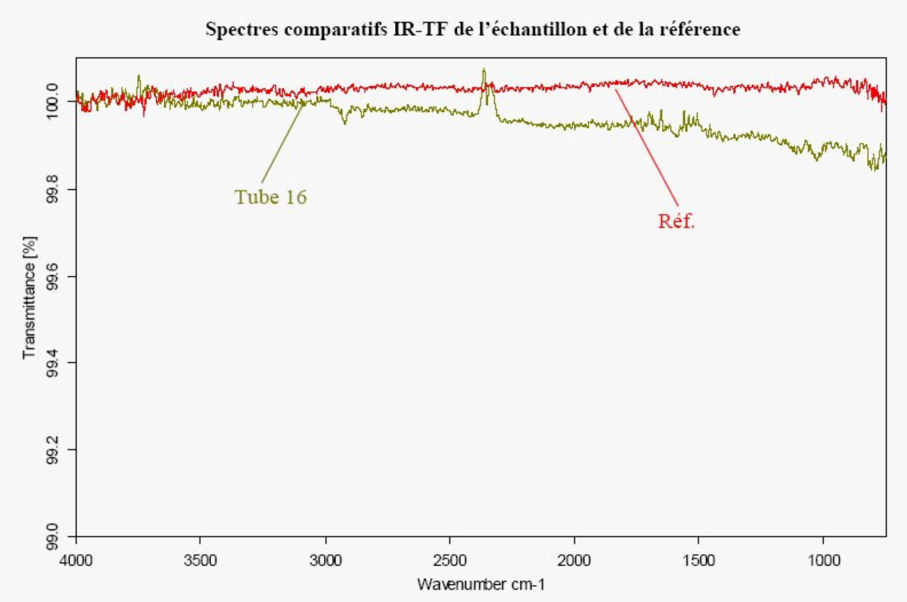

Figure 5.22: FTIR of the tubelet belonging to tube 16 of layer 3 ($1-\Delta G/G\ \sim$10%).

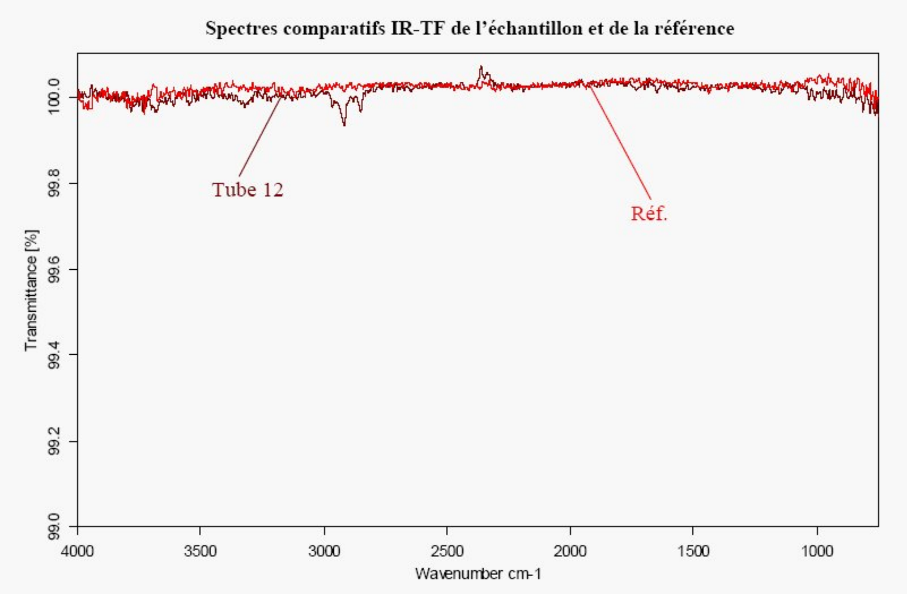

Figure 5.23: FTIR of the tubelet belonging to tube 12 of layer 3 (not affected by ageing).

However, the quantity of contaminant needed to cause ageing effects as reported in this study, should be so small that could be very difficult to find it out.

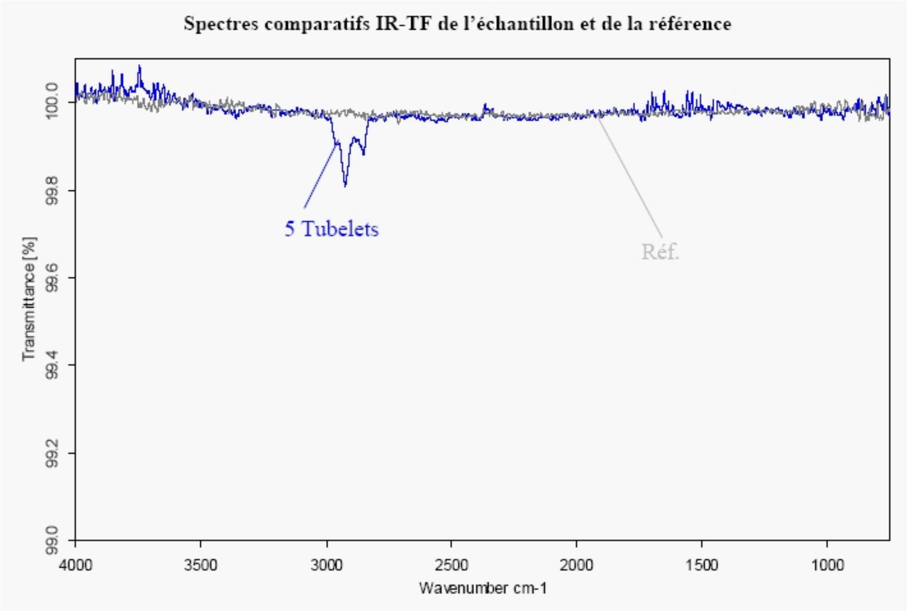

Figure 5.24: FTIR of five tubelets belonging to BIS layer three tubelets cleaning batch but not used.

5.5 Impact of the ageing effects on efficiency and resolution

To estimate the losses in efficiency and spatial resolution due to an ageing effect like the one observed in this ageing test, we performed a Garfield simulation.
We simulated a data sample of 100k 180GeV muon tracks in standard conditions [35]. The analog signals at the output of the ASD, before the Wilkinson ADC and the TDC, were stored. The time of threshold crossing was extracted by applying the nominal value of the threshold. The efficiency is the fraction of signals over threshold. Using the TDC informations and the Wilkinson ADC informations the r-t relation and the spatial resolution[2], including the time slewing correction, were calculated. Since the MDT works in proportional regime, a gain loss can be simulated by a corresponding increase of the threshold.
Then, we calculated the variations of the tube spatial resolution and efficiency as a function of the gain loss, as reported in table 5.1.

The effects caused by the ageing of 15% of the tubes on the first 10÷12 cm of the wire are very small.

Gain scale factor	Resolution (μm)	Efficiency (%)
1	76	99.95
0.95	77	99.944
0.90	78	99.938
0.85	79	99.925
0.80	81	99.917
0.75	83	99.908
0.70	85	99.901
0.60	91	99.867

Table 5.1: Spatial resolution and efficiency at different gain reduction.

---

[2] $\sigma_{tube} = \sqrt{\int_{r>1mm} \frac{\sigma^2(r)}{b-1} dr}$, b being the tube inner radius 14.6mm [14]

Conclusions

The subjects of this Thesis are the accuracy and the reliability of the MDT chambers of the muon spectrometer of the ATLAS detector.

For the first subject, we have discussed a new method for the measurement of the geometrical parameters of a chamber. The method has been evaluated with the help of a simple Monte Carlo data sample. The method consists in collecting the tracks of the cosmic rays for a short period of data taking. Then, by reconstructing these tracks in the two multilayers and comparing the results of the two fits, an accuracy of 1.6 mrad and 230 μm can be achieved on the parameters of each track. These figures correspond to a statistical accuracy on the displacement of the two multilayers of 10 μrad in the rotation and 1 μm in the displacement after a data taking period of 1.5 days. The performances of the method have been demonstrated by simulating a chamber with a sizable distortion and by checking the effective capability of measuring its parameters.

The study of the chamber ageing has required a larger effort. We have equipped a MDT chamber with a special electronic setup and exposed it to the CERN GIF facility. The elements of the gas system have been carefully checked, avoiding organic pollutants and unknown sealants. A new data taking program and offline analysis chain have been developed for the test. After 100 days of irradiation, corresponding to 290 mC/cm/tube, equivalent to 30 years of LHC, the following results have been found :

- no tube had a decrease of the signal greater than 5%, apart from the first 10÷12 cm from the gas inlet;

- in the first 10÷12 cm of the tube, 82 out of 96 tubes show no appreciable deterioration of the signal;

- the remaining 14 tubes show a decrease of the signal between 5% and 30%; the drop is not linear with the irradiation, but remains constant after 70 mC/cm/tube without any further increase;

- for these tubes, the resultant loss in efficiency is negligible, even if only the affected small region is considered;

- the only possible consequence of the effect is a (small) systematic increase in the resolution, due to the (small) delay in the measured time, not taken into account by the autocalibration;

- the chemical analysis of the wires, both with the Scanning Electron Microscope, the Energy Dispersive X-ray and the Fourier Transform InfraRed spectroscopy techniques, was able to identify the effect, but gave no clue for its cause.

In summary, although the origin of the effect is not completely understood, its size and phenomenology do not look very dangerous. For that conclusion, the results of the test has been very positive and encouraging.

In fact, the real concern comes from a different source. The results of the preliminary tests show the fragility of the chambers with respect to the gas composition and the radiation environment. Even a small contamination in few components can cause a great damage. Although in principle this behavior was well known before, these tests had a large impact in the ATLAS muon community and contributed to a better understanding of the problems and a better use of the resources.

Bibliography

[1] C. Adorisio, C. Cernoch, M. Cirilli, A. Di Girolamo, S. Konig, A. Kramer, S. Palestini, P. Valente, and S. Zimmermann. Recent and ongoing ageing studies for the atlas muon spectrometer drift tubes. *Nuclear Instruments and Methods A*, 26132, 2003.

[2] C. Adorisio, C. Cernoch, M. Cirilli, A. Di Girolamo, S. Palestini, P. Valente, and S. Zimmermann. Recent and ongoing ageing studies of for the atlas muon spectrometer drift tubes. *IEEE 2004, pub. proceedings in progress.*

[3] C. Adorisio, C. Cernoch, M. Cirilli, A. Di Girolamo, S. Palestini, P. Valente, and S. Zimmermann. Ageing studies for the atlas muon spectrometer drift tubes. *Pub. in progress*, 2004.

[4] C. Adorisio, C. Cernoch, M. Cirilli, A. Di Girolamo, S. Palestini, P. Valente, and S. Zimmermann. Final results of mdt ageing studies at x5/gif. 2004.

[5] P. Bagnaia, C. Bini, G. Ciapetti, A. De Salvo, A. Di Girolamo, and E. Solfaroli. Performance of an mdt cosmic test stand : a monte carlo evaluation. *Atlas Internal Note ATL-COM-MUON-2004-014.*

[6] R. Barate et al. Search for the standard model higgs boson at lep. *Phys. Lett.*, B565:61–75, 2003.

[7] S.Zimmermann C.Cernoch. Mdt ageing studies : Results of the measurements conducted at the gamma irradiation facility gif between autumn 2001 and summer 2003. *Atlas Internal Note ATL-COM-MUON-2004-019.*

[8] C. Cernoch. Performance of atlas muon precision drift chambers in a high radiation environment. *PhD Thesis*, 2003.

[9] M. Cirilli, A. Di Domenico, A. Di Girolamo, S. Fiore, S. Lacava, C. Luci, L. Pontecorvo, D. Salvatore, A. Tonazzo, and S. Zimmermann. Results from the 2003 beam test of a mdt bil chamber:systematic uncertainties on the tdc

spectrum parameters and on the space-time relation. *Atlas note atlas-com-muon-2004-009*, 2004.

[10] ALICE collaboration. Alice physics performance report. 2003.

[11] CMS collaboration. Cms technical proposal. 1994.

[12] LEP collaboration. A combination of preliminary electroweak measurements and constraints on the standard model. 2003.

[13] The Atlas collaboration. The atlas detector and physics performance technical design report. *CERN/LHC 99-14/15.*

[14] The Atlas collaboration. Atlas muon technical design report. *CERN/LHC 97-22.*

[15] A.H. Compton. *Phys. Rev.*, page 458, 1923.

[16] A. Dell'Acqua et al. The atlas muon spectrometer simulation using geant4. *Atlas Internal Note ATL-MUON-2000-020.*

[17] Allkofer et al. *Phys. Lett. 36B*, 425, 1971.

[18] C. Bacci et al. Design of a cosmic test site for the quality assurance and quality control of the full mdt chambers. *Atlas Internal Note ATL-MUON-98-241.*

[19] C. Posch et al. Mdt-asd, cmos front-end for atlas mdt. *Atlas Internal Note ATL-MUON-2002-003.*

[20] E. Gschwendtner et al. Analysis and results from measurement on an x-ray tomograph of large full-scale mdt prototypes. *Atlas Internal Note ATL-MUON-98-175.*

[21] F.Bauer et al. Monitoring of the accuracy of the mdt chamber construction. *Atlas Internal Note ATL-COM-MUON-2003-10.*

[22] G.Kaptis et al. Mechanical design of the bis module zero mdt chamber. *Atlas Internal Note ATL-COM-MUON-98-242.*

[23] L. Pontecorvo et al. Integration tests of the muon system. *Atlas e-news ATL-ENEWS-2003-007.*

[24] P. Bagnaia et al. Calib: a package for mdt calibration studies. user manual. *Atlas Internal Note ATL-COM-MUON-2002-004.*

[25] P. Bagnaia et al. Study of the mdt drift properties computed with the garfield program. *Atlas Internal Note ATL-COM-MUON-2003-028.*

[26] R. Avramidou et al. Calibration of the x-ray tomograph. *Atlas Internal Note ATL-MUON-2001-008.*

[27] S. Agosteo et al. A facility for the test of large area muon chambers at high rates. *Nuclear Intruments and Methods A*, 452:94–104, 2000.

[28] K. Hagiwara, K. Hikasa, K. Nakamura, M. Tanabashi, M. Aguilar-Benitez, C. Amsler, and O.V Zenin. Review of Particle Physics. *Physical Review D*, 66:010001+, 2002.

[29] J. A. Kadyk. Wire chamber aging. *NIM A*, 300:436–479, 1991.

[30] Klein and Nishina. *Zeits. f. Physik*, 52:853, 1928.

[31] R. Kotthaus. A laboratory study of radiation damage to drift chambers. *Nuclear Instruments and Methods A*, 252:531–544, 1986.

[32] L. Landau. *JPhysics (USSR)*, 8:201, 1944.

[33] lhcb collaboration. lhcb technical proposal. 1998.

[34] W Riegler M. Aleska. Non-linear mdt drift gases like ar/co2. *Atlas Internal Note ATL-MUON-1998-268.*

[35] P.Mastrandea. *Thesis*, 2004.

[36] S. Ramo. Currents induced by electron motion. *IRE*, 27:584–5, 1939.

[37] J. Va'vra. Review of wire chamber aging. *NIM A*, 252:547–563, 1986.

[38] R. Veenhof. Garfield. *CERN Program library*, W5050.

[39] Diethorn W. A methane proportional counter system for natural radiocarbon measurements. *USAEC report NY06628*, 1956.

[40] M.J. Woudstra. Precision of the atlas muon spectrometer. *PhD Thesis*, 2002.

[41] H. Yasuda. New insights into aging phenomena from plasma chemistry. *Nuclear Instruments and Methods A*, 515:15–30, 2003.

[42] S. Zimmermann. High rate and ageing studies for drift tubes of the atlas muon spectrometer. *PhD Thesis*, 2004.

List of Figures

List of Tables